Cross-Sectional Compactness and Bracing Requirements for Hybrid HPS Girders

by

Nicola Greco

B.S. in Civil Engineering, University of Pittsburgh, 2000

Submitted to the Graduate Faculty of

School of Engineering in partial fulfillment

of the requirements for the degree of

Master of Science in Civil Engineering

University of Pittsburgh

2002

UNIVERSITY OF PITTSBURGH

SCHOOL OF ENGINEERING

This thesis was presented

by

Nicola Greco

It was defended on

April 16, 2002

and approved by

Dr. Jeen-Shang Lin, Associate Professor, Department of
Civil and Environmental Engineering

Dr. John F. Oyler, Adjunct Associate Professor, Department of
Civil and Environmental Engineering

Thesis Advisor: Dr. Christopher J. Earls, Associate Professor, Department of
Civil and Environmental Engineering

ABSTRACT

Signature_____
Christopher J. Earls, Ph.D.

CROSS SECTIONAL COMPACTNESS AND BRACING REQUIREMENTS FOR HYBRID HPS GIRDERS

Nicola Greco, M.S.

University of Pittsburgh

Current American steel building and bridge design specifications (AISC 1999, AASHTO 1998) simplify the flexural design of both homogeneous and hybrid I-shaped

members by treating local and global inelastic stability phenomenon independently. According to both specifications, if a homogeneous or hybrid section is compact and sufficiently braced against lateral instability, the member will achieve or exceed its theoretical plastic moment capacity and maintain this capacity so as to allow sufficient rotation capacity for inelastic force redistribution to take place (Yura et al. 1978). Treating local and global buckling independently has been proven by past experience to be successful when formulating flexural design provisions for lower strength steels. However, new research (Earls 1999, 2000a, 2000b, 2001) is proving that this approach is much more difficult to apply to the design of High Performance Steel (HPS) I-shaped flexural members. The main objective of the current study is to investigate the effect HPS flanges have on hybrid girder flexural ductility. Finite element models of hybrid HPS girders, employing nonlinear shell elements, are used to study the influence of flange slenderness ratios, and bracing configuration on hybrid HPS girder response at ultimate.

DESCRIPTORS

Hybrid Steel Girder

High Performance Steel

Rotation Capacity

Local and Global Buckling

Compactness

Unbraced Length

Nonlinear Finite Element Analysis

ACKNOWLEDGEMENTS

I would like to thank my advisor, Dr. Christopher J. Earls, for his guidance and support throughout my graduate career and especially on this thesis. By his example, Dr. Earls has given me a passion for structural engineering and the motivation to excel in all endevours. I am honored to have conducted this research under his guidance.

I would also like to thank the members of my committee, Dr. Jeen-Shang Lin and Dr. John F. Oyler. Their guidance throughout my graduate career is greatly appreciated. Also, it has been a great pleasure to be a teaching assistant for Dr. Jeen-Shang Lin.

I would like to thank all of my officemates, both past and present, for all their support and help throughout my graduate studies. I will never forget my experiences here with them.

I would especially like to thank my girlfriend, Lauren Fritz, for being my best friend and my unending support. I would like to extend my thanks to her family for giving me support and confidence throughout my graduate studies.

I am indebted to my family for their unending support. I would like to thank my father, Francesco A. Greco for coming to this country in hopes of a better life for himself and his family. I would like to thank my sister, Michela Greco, for giving me her love and support unconditionally.

This work is dedicated to my mother, Elisabetta Greco, without her none of this would have been possible. She has taught me more in life than she could imagine. She is my inspiration.

TABLE OF CONTENTS

Page

Page

LIST OF FIGURES

Figure No. Page

Figure No. Page

Figure No. Page

Figure No. Page

LIST OF TABLES

NOMENCLATURE

b_f	Flange width, mm
d	Overall depth of member, mm
E	Modulus of elasticity of steel
F_{cr}	Critical Stress, ksi (MPa)
F_y	Specified minimum yield stress of the type of steel being used, ksi (MPa)
F_u	Specified minimum tensile strength of the type of steel being used, ksi (MPa)
h	Web height, mm
L_b	Lateral unbraced length; length between points that are either braced against lateral displacement of the compression flange or braced against twist of the cross section, m
M	Beam bending moment, k-in (kN-mm) or k-ft (kN-m), as indicated
M-θ Plot	Moment versus rotation plot
M_{cr}	Elastic buckling moment, k-in (kN-mm) or k-ft (kN-m), as indicated
M_r	Limiting buckling moment, M_{cr}, when $\lambda = \lambda_r$ and $C_b = 1.0$, , k-in (kN-mm) or k-ft (kN-m), as indicated
M_p	Plastic bending moment, k-in (kN-mm) or k-ft (kN-m), as indicated
M_y	Moment corresponding to the onset of yielding at the extreme fiber from an elastic stress distribution, kip-in (MPa)
R	Nominal rotation capacity

t_f	Flange thickness, mm
t_w	Web thickness, mm

Symbols

β	Relative difference in yield stress
β_{br}	Required panel shear stiffeness
ε	Coefficient of linear expansion
γ	Relative difference in yield price
λ	Slenderness parameter
θ_u	The rotation when the moment capacity drops below M_p
θ_p	The theoretical rotation at which the full plastic capacity is achieved based on elastic beam stiffeness
ν	Poisson's ratio

Acronyms

AASHTO	American Association of State Highway and Transportation Officials
AISC	American Institute of Steel Construction
AISI	American Iron and Steel Institute
ASCE	American Society of Civil Engineers
ASTM	American Society for Testing and Materials
FEM	Finite Element Method
FHWA	Federal Highway Administration
HPS	High Performance Steel

LRFD	Load and Resistance Factor Design
TMCP	Thermo-Mechanical Control Processing

1.0 INTRODUCTION

I-shaped beams and girders are flexural structural members that carry transverse loads perpendicular to their longitudinal axis primarily in a combination of bending and shear. Bending resistance is achieved through the action of a compression and tension force inducing a couple resisting the externally applied moment. The compression element (flange) of the cross section is integrally braced perpendicular to its plane through its attachment to a stable tension flange by means of a web. Thus, the two flanges provide the majority of the bending resistance by acting simultaneously in compression and tension, while the web provides practically all of the shear resistance and serves to maintain a fixed distance between flanges. A hybrid steel member exploits the notion that flexural resistance is primarily the concern of the flanges by situating higher strength steel in the flanges rather than in the web as shown in Figure 1. Thus, for a member subjected to pure bending (or a moment gradient in a reasonably proportioned flexural section), the hybrid concept provides a more efficient and economical section. This is true since the shear stresses in a typical I-shaped flexural member are less critical than the longitudinal flexural stresses in terms of magnitude.

The implementation of high strength steels in the flanges of hybrid girders dates back to the early 1940's. The high strength steels available at that time, and for most of the twentieth century, were able to achieve high yield strengths (690 MPa) but with very little ductility. These high strength steels also demonstrated poor weldability because of their high carbon content. The advent of new steelmaking techniques has spawned a

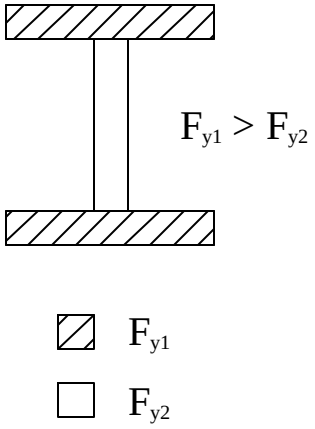

Figure 1 Illustration of Hybrid Steel Member

steel, High Performance Steel (HPS), that is able to reach yield strengths equal to those of the earlier high strength steels but with superior ductility and welding properties. The high-strength-to-weight ratio, good notch toughness, and the little or no preheat requirements for welding make HPS an optimal material to utilize in a hybrid girder. However, limitations in the use of HPS in the design of both hybrid and homogeneous girders arise from the recognition that of current design specification provisions were developed from research results conducted primarily on mild carbon steel grades with yield strength levels of 345 MPa or less. Limitation on the use of HPS in applications requiring significant structural ductility are reasonable given the fact that: HPS grades of steel tend to have a larger yield ratio (F_y/F_u); no appreciable strain hardening behavior; little or no yield plateau and an abbreviated ductility as compared with more common steel grades. These limitations arise mostly out of a lack of data related to the ultimate strength performance of HPS structural members.

Current American steel building and bridge design specifications (AISC 1999, AASHTO 1998) simplify the flexural design of both homogeneous and hybrid I-shaped members by treating local and global inelastic stability phenomenon independently. However, new research (Earls 1999, 2000a, 2000b, 2001) is proving that this approach is much more difficult to apply to the design of HPS I-shaped flexural members.

The complex interaction between local and global buckling phenomenon in the flexural response of I–shaped beams and girders is not a new idea. In its guide and commentary on plastic design, the American Society of Civil Engineers (ASCE) (ASCE 1971) states: "Even though local and lateral torsional buckling in the inelastic range are manifestations of the same phenomenon, namely, the development of large cross sectional distortions at large strains, they have been treated as independent problems in the literature dealing with these subjects." Despite this complex reality, treating local and global buckling independently has been proven by past experience to be successful when formulating flexural design provisions for lower strength steels. The existing design criteria established in both the AISC load and resistance factor design (LRFD) and American Association of State Highway Transportation Officials (AASHTO) LRFD design specifications adhere to this principle. According to both specifications, if a homogeneous or hybrid section is compact and sufficiently braced against lateral instability, the member will achieve or exceed its theoretical plastic moment capacity and maintain this capacity so as to allow sufficient rotation capacity for inelastic force redistribution to take place (Yura et al. 1978).

Rotation capacity is one measure of structural ductility, or deformation capacity, defined by ASCE (ASCE 1971) as $R = \{(\theta_u / \theta_p) - 1\}$ where q_u is the rotation when the moment capacity drops below M_p on the unloading portion of the M-q plot and q_p is the theoretical rotation at which the full plastic capacity is achieved based on elastic beam stiffness. This definition is described graphically in Figure 2. In this figure, q_1 corresponds to q_p, and q_2 corresponds to q_u in the ASCE definition.

The main objective of the current study is to investigate the effect HPS flanges have on hybrid girder flexural ductility. Finite element models of hybrid HPS girders, employing nonlinear shell elements, are used to study the influence of flange slenderness ratios, and bracing configuration on hybrid HPS girder response at ultimate.

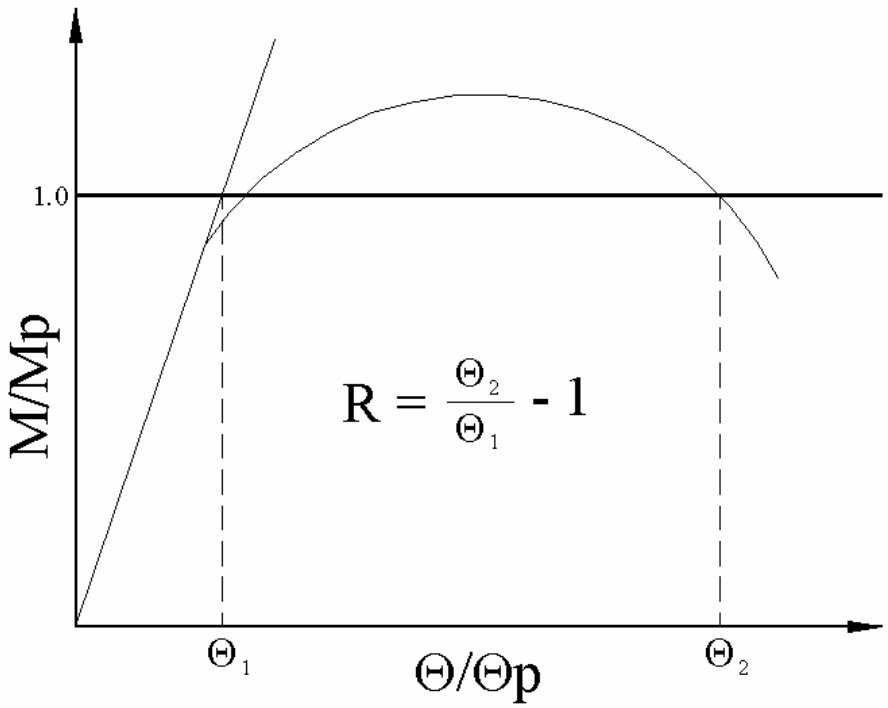

Figure 2 Definition of Rotation Capacity

1.1 Background and Literature Review

High Strength Quenched and Tempered Steel, ASTM A514, with 690 MPa yield strength has been available for about 40 years, originally sold under the trademark T – 1 Steel and developed by US Steel Corporation. Although past research had shown that many bridges could be designed more efficiently with ASTM A514, few bridge owners were willing to risk potential problems in fabrication. The high strength steel's susceptibility to hydrogen induced cracking made fabrication an expensive and highly controlled process owing to the high values of heat input, post-weld treatment, and strict control of welding consumables (Wasserman and Pate 2002). Also, A514 displayed inadequate structural ductility. Thus, there came to be a recognized need for improvement in overall performance of high strength steels (i.e. weldability, toughness, corrosion resistance).

A cooperative research program with the U.S. Federal Highway Administration (FHWA), American Iron and Steel Institute (AISI), and the U.S. Navy was initiated to improve upon the performance qualities of high strength steels while maintaining high yield strength. Through the application of thermo-mechanical control processing (TMCP), high performance steel (HPS) was developed. TMCP was able to control ranges of elements, including carbon, sulfur, and phosphorus; resulting in improved weldability, fracture toughness, and crack resistance (Teal 2002). The major contributing factor improving on the performance of high strength steel was the lowering of the carbon level which greatly improved weldability and toughness. HPS toughness values

exceeded AASHTO minimum requirements for fracture critical members in the most severe climate (Zone III) thus providing a very high resistance to brittle fracture (Wright 1997). Furthermore, HPS was created to have high corrosion resistance, satisfying the composition requirements listed in ASTM specification G – 101 to allow classification as "weathering" steel (Wright 1997). The improved performance qualities, high yield strength, and ease of welding made HPS an attractive material for designers.

Even with the performance limitations of A514, Haaijer (1961) showed that with efficient design techniques, the application of higher strength steel could lead to a significant material-cost savings for lighter weight structures. He exploited the fact that, when compared to the mild carbon steels, the higher strength steels showed a relative increase in price that was less than the relative increase in yield stress. Haaijer investigated the influence of yield stress, modulus of elasticity, and price on the proportioning of tension members, hot-rolled beams, and built-up welded girders.

For a beam, the higher strength steel was recognized to be more effective in the flanges than in the web (Haaijer 1961) and therefore, special attention was given to hybrid beams. Based on the plastic moment of a hybrid beam, the optimum proportions for minimum material cost were established. This made it possible to establish the relative weight, cost, depth of section, and deflection of a hybrid steel beam as compared with those of an optimum beam of uniform yield stress (equal to the yield stress of the web of the hybrid beam) (Haaijer 1961).

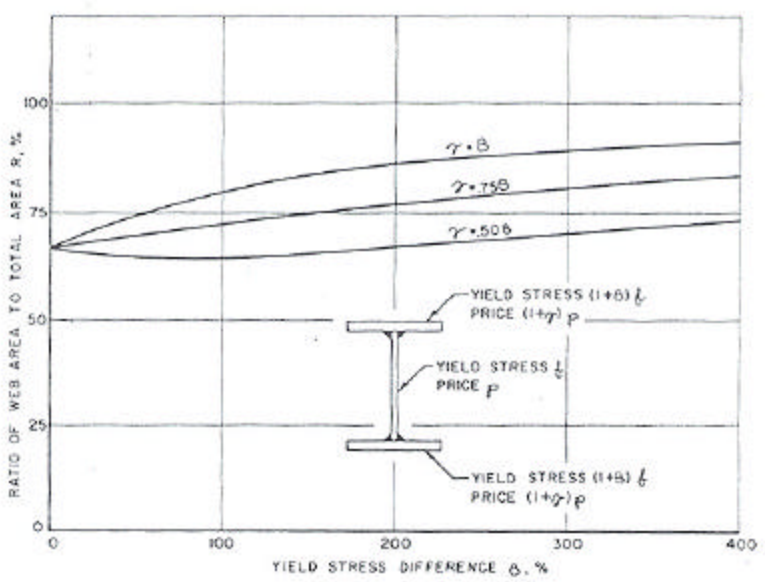

Figure 3 Effect of the Relative Difference in Yield Stress, ß, and the Relative Difference in Price, ?, on the Ratio R (Haaijer 1961)

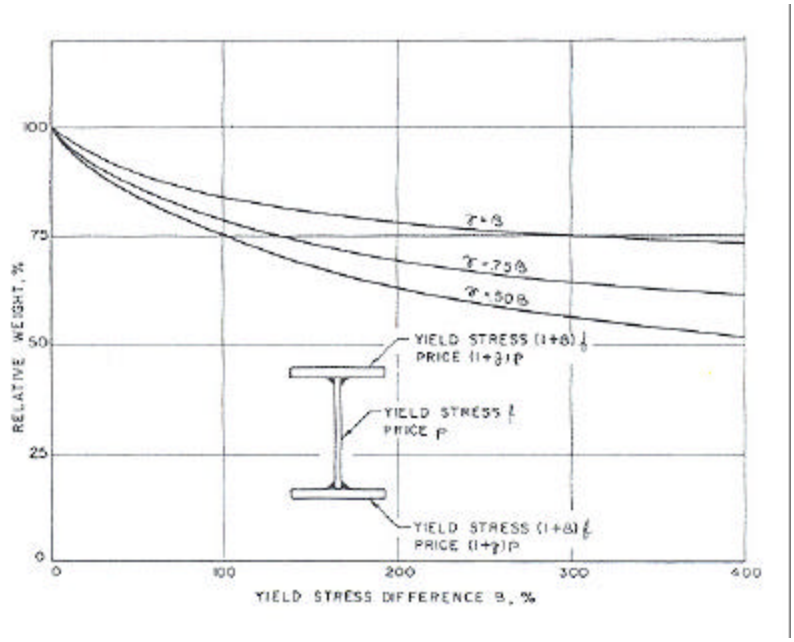

Figure 4 Relative Weights of Beams Designed for Minimum Material Cost (Haaijer 1961)

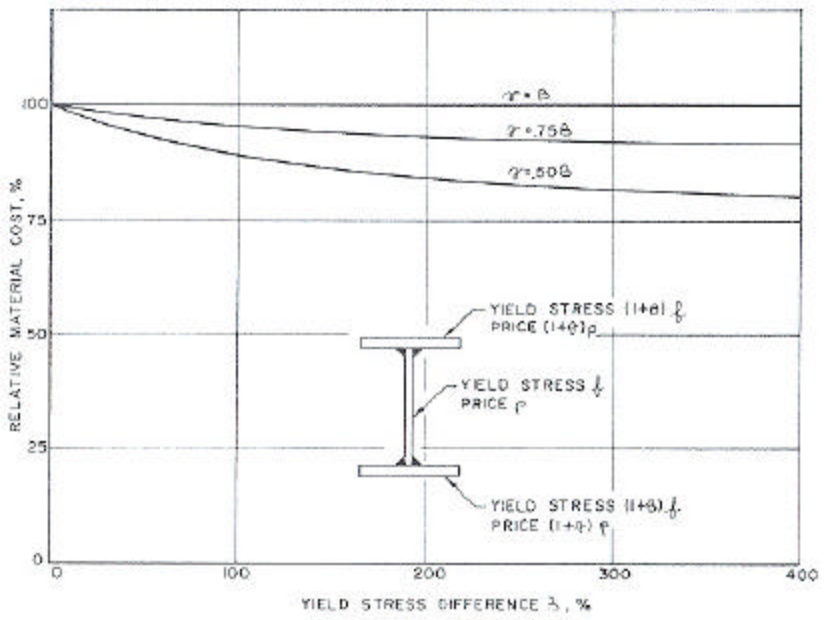

Figure 5 Cost of Optimum Hybrid Steel Beams (Haaijer 1961)

It was found that the significant parameter influencing the total material cost of a hybrid beam was the ratio of web area to total area, *R* (Haaijer 1961). Figure 3 shows the effect of the relative difference in yield stress, *ß*, and the relative difference in price, *?*, on the ratio *R*. Three curves were plotted corresponding to *?* = *ß*, *?* = 0.75 *ß*, *?* = 0.50 *ß*. The curves show that if relatively expensive steels were used for the flanges (*?* = *ß*), a greater portion of the steel should be in the web than when flanges were made from a relative cheap steel (*?* < *ß*) (Haaijer 1961). Figure 4 shows the relative weights of beams designed for minimum material cost. The smallest weights were obtained with the cheapest highest strength steels. The cost comparisons for these beams are shown in Figure 5. The results indicated that when the relative increase in price equaled the relative increase in yield stress (*?* = *ß*), no change in total material cost occurred. If the

relative increase in price was less than the relative increase in yield stress (which was true of virtually all higher strength steels), the material cost of the hybrid steel beam was less than the material cost of the beam of uniform strength (Haaijer 1961). This latter point is illustrated for specific steels of 1961 in Table 1. The steels vary from yield strengths of 33 ksi (A7) to 100 ksi (A514). All hybrid beams showed less material costs than the homogenous steel beams made of A7 steel. Thus, in his investigation, Haaijer was able to show that hybrid steel beams utilizing high strength steel in the flanges produced both weight and material-cost savings in all combinations tested.

Table 1 Hybrid Steel Beams of Equal Strength (Haaijer 1961)

Steel						
Web (1)	Flanges (2)	R[a] (3)	Relative Depth of Beam (4)	Relative Weight (5)	Relative Material Cost (6)	Relative Elastic Deflection (7)
A7	A7	0.67	1.00	1.00	1.00	1.00
A7	A441	0.65	0.91	0.85	0.95	1.38
A7	"T-1" type A	0.68	0.80	0.63	0.85	2.49
A7	"T-1"	0.75	0.87	0.68	0.92	2.16
A441	"T-1" type A	0.65	0.75	0.58	0.90	3.17
COR-TEN	"T-1"	0.73	0.81	0.60	0.99	2.74

[a] R = ratio of web area to total area.

Despite a history of application dating back to the 1940's, the theoretical behavior of hybrid steel members had not been analyzed until 1964, when a theoretical and experimental program was conducted at the Applied Research Laboratory of the United States Steel Corporation (Frost and Schilling 1964). Frost and Schilling (1964) analyzed

the behavior of a hybrid steel beam, with high strength steel (A514) situated in the flanges, under pure bending and combined shear and bending. This hybrid beam behavior was compared with the static behavior of a homogeneous beam made of A514 steel. Based on this research, the Subcommittee 1 on Hybrid Beams and Girders of the Joint ASCE-AASHO Committee on Flexural Members (1968) was formed to develop design methods for symmetrical hybrid beams and girders that would reflect their true strength and thus allow the efficient utilization of the hybrid concept.

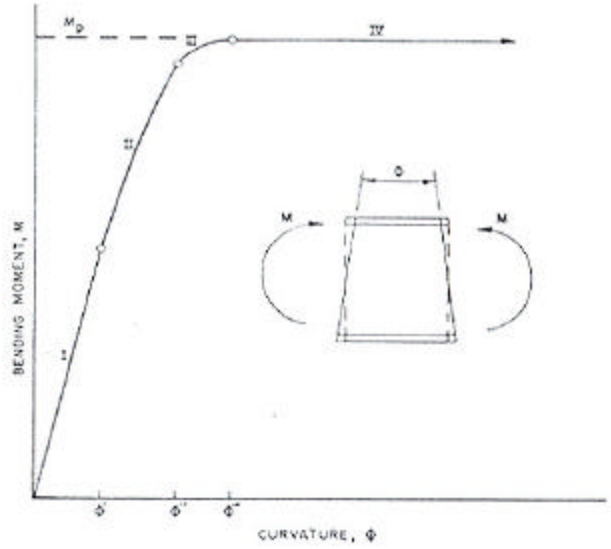

Figure 6 Moment-Rotation Relationship for a Hybrid Beam (Frost and Schilling 1964)

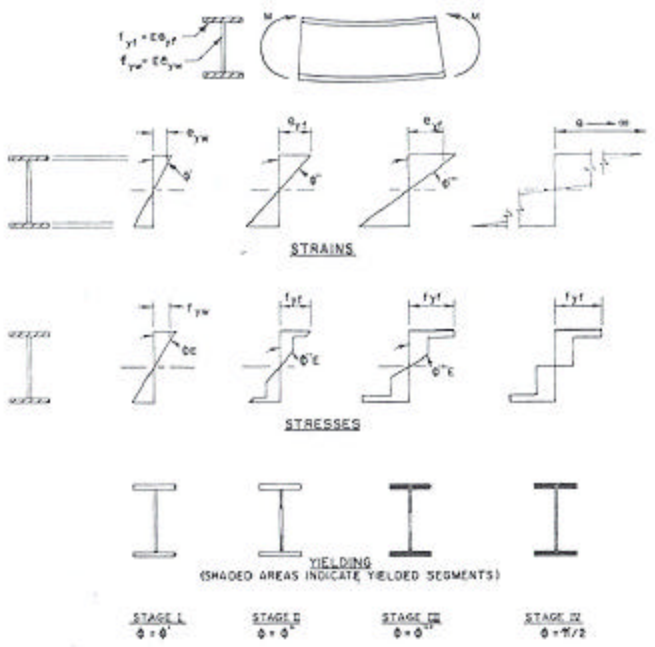

Figure 7 Distribution of Strain, Stress, and Yielding at the Upper Limit of Each Stage of Loading (Frost and Schilling 1964)

Schilling and Frost (1964) explained the theoretical behavior of a typical hybrid beam in pure bending by considering the hypothetical bending moment, *M*, versus rotation, *f* , response shown in Figure 6. The hybrid beam was assumed to have the same material makeup of Figure 1, proportioned so as to prevent local buckling, and braced accordingly in order to prevent lateral torsional buckling. It is seen in Figure 6 that the moment versus rotation plot passes through four stages. The distribution of strain, stress, and yielding at the upper limit of each of these stages was presented schematically by Schilling and Frost and reproduced here as Figure 7. Stage I represents the range in which the hybrid beam is fully elastic and the moment is directly proportional to the rotation (Schilling and Frost 1964). Stage II represents the range in which yielding

develops in the outer fibers of the web while the flanges remain elastic (Schilling and Frost 1964). In this stage, the plastic strain in the web is controlled by the elastic strain of the flanges. Because the stress in the web cannot exceed the yield strength of the web steel, the nonlinear stress distribution develops. Stage III represents the range in which only a small portion of the web near the neutral axis remains elastic and yielding progresses entirely through the flanges (Figure 7) (Schilling and Frost 1964). Therefore, the rotation in this stage increases rapidly as the moment approaches the plastic moment of the cross section. The final stage, Stage IV, represents the range in which the remaining elastic portion of the web at the neutral axis becomes plastic and the hybrid beam reaches its ultimate load. Schilling and Frost observed the difference between the theoretical bending behavior of hybrid and homogeneous beams was small. The major difference resulted from the fact that the homogeneous beam remains elastic until yielding began in the flanges, whereas the hybrid beam began to yield in the web at a lower moment.

Schilling and Frost (1964) defined the bending strength of a hybrid girder, like that of a homogeneous beam, as two quantities: (1) the yield moment, M_y; (2) the plastic moment, M_p, the ultimate bending strength of a beam. The yield moment of a hybrid beam showed to have little practical significance based on the above theoretical behavior (Schilling and Frost 1964). A third and more meaningful definition of bending strength for a hybrid beam was defined to be the moment causing first yielding of the flanges (upper limit of Stage II, Figure 6) (Schilling and Frost 1964). Schilling and Frost (1964) indicated that this moment would be somewhat comparable to the yield moment for

homogeneous beams because it represented the moment above which the rotation would deviate significantly from a straight line in a moment versus rotation plot.

In addition to the theoretical research done, Schilling and Frost experimentally investigated the bending behavior of hybrid beams. Three beams, possessing A514 (690 MPa) steel in the flanges with varying steel in the webs, were tested for moment-rotation response. The three webs were made up of A7 (228 MPa), A242 (345 MPa), and A514 steels and were labeled C, H, and T, respectively (Schilling and Frost 1964). The experimental moment versus rotation curves for the three tested beams are shown in Figure 8, indicating the initiation of web and flange yield moments. It is noted that the experiments were terminated upon achievement of each beam's plastic moment, M_p. The main objective of the experiments was to observe the manner in which stresses and deformations resulting from applied loads developed (Schilling and Frost 1964). Therefore, Schilling and Frost did not examine the plastic behavior of the hybrid girder beyond the attainment of M_p but did state that local buckling could be prevented by applying the dimensional limitations for the members designed according to plastic design methods.

From the experimental results it was shown that the bending behavior of the hybrid beams differed slightly to that of the homogeneous beam. The main difference resulted from the fact that the load required to initiate yielding in the flanges of the hybrid beams was slightly smaller than the load required to initiate yielding in the flanges of the homogeneous beam because, as a result of yielding, the web of the hybrid beam did not contribute its full share of the bending moment (Schilling and Frost 1964, Subcommittee

1 1968). Also, the plastic moment for a homogeneous beam is larger than the plastic moment of a hybrid beam because of the larger contribution of the homogeneous-beam web to the ultimate bending strength (Subcommittee 1 1968).

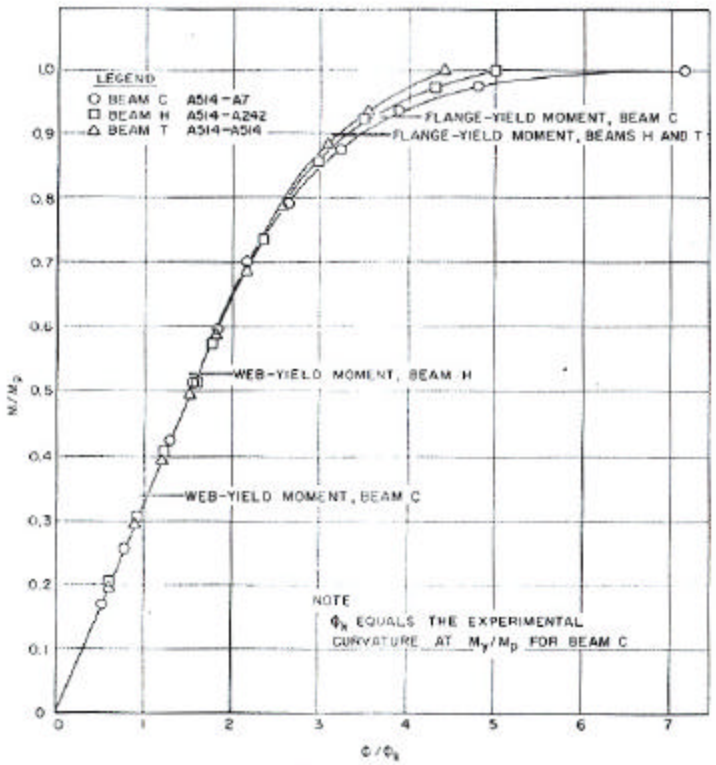

Figure 8 Experimental Bending Behavior Curves for Hybrid Beams (Subcommittee 1 1968)

Based mainly on the theoretical and experimental work of Schilling and Frost (1964), Subcommittee 1 on Hybrid Beams and Girders of the Joint ASCE-AASHO Committee on Flexural Members (1968) was able to develop conservative design methods for hybrid beams and girders. The Subcommittee 1 design guides were

comparable to the specification requirements for the allowable-stress (elastic) design of homogeneous beams (Subcommittee 1 1968). Although Subcommittee 1 stated that hybrid beams, like homogeneous beams, could also be designed by plastic design-methods, they were not considered in the formulation of the design guides. This omission was due to the lack of plastic-design buckling limits for A514 steel (Subcommittee 1 1968). Therefore, Subcommittee 1 recommended that the design of hybrid beams be based on an allowable moment calculated as the flange-yield moment divided by a factor of safety (Subcommittee 1 1968). Recommendations on cross-sectional member proportions and bracing, based on observations of Schilling and Frost, were given so that local and global buckling of the hybrid member would not occur prior to achievement of the flange yield stresses (Subcommittee 1 1968).

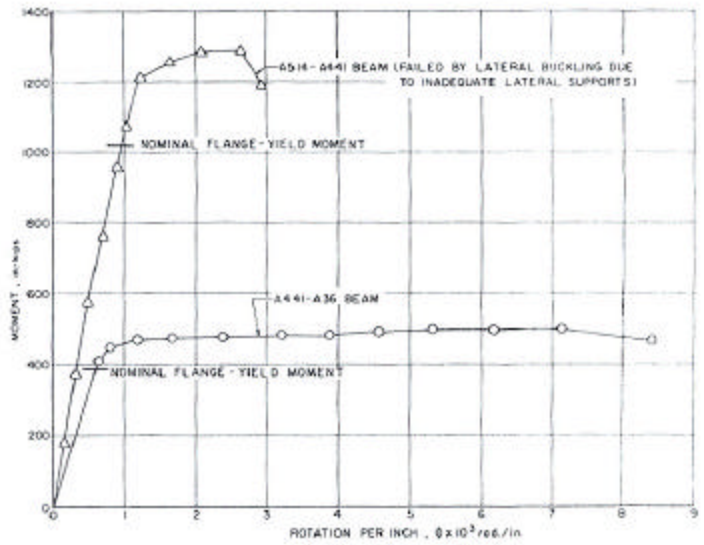

Figure 9 Experimental Moment-Rotation Curves for Hybrid Beams (Toprac 1964)

Although the design recommendations were based on flange material yield stress properties, Subcommittee 1 did note that hybrid beams, like homogeneous beams, could sustain considerable rotation after the ultimate load was reached without a rapid drop in load if adequate lateral bracing was provided (Subcommittee 1 1968). This observation was based on the experimental hybrid beam test results of Toprac (1964) shown in Figure 9.

The previously mentioned research depended on the achievement of yield stresses and the use the less favorable A514 high strength structural steel and did not consider the plastic behavior of hybrid girders. Despite the lack of experimental data, current design specifications (AISC 1999, AASHTO 1998) were able to formulate provisions that enable the achievement of a hybrid beam's ultimate capacity, M_p, and allow for sufficient rotation capacity prior to the occurrence of local or global buckling. The design specification provisions also include the use of the more favorable High Performance Steel in both hybrid and homogeneous girder design.

Current American steel building and bridge design specifications require that a hybrid girder be compact and adequately braced in order to achieve M_p. These provisions are applied to hybrid sections as if they were a homogeneous beam with a yield stress equal to that of the hybrid girder's flanges and are therefore indifferent to the presence of a web with a lesser yield strength. The member is considered compact and adequately braced once some limits on cross-sectional and member slenderness ratios are satisfied, respectively. Differences in steel grades are accounted for in these ratios through the inclusions of a scaling factor related to the inverse of the square root of the yield stress

associated with the compression flange. Implicit in such an approach is that this scaling factor should account for all the behavioral changes that accompany the significant deviations in uniaxial material responses when the new High Performance Steel (HPS) grades are situated in the flanges of hybrid beams. This approach has been proven to be un-conservative for homogeneous girders made of HPS (Earls 1999, 2000a,b, 2001).

Earls (1999, 2000a,b, 2001) has provided evidence that the conventional approach of treating local and global inelastic stability phenomenon independently may not be applicable to the new high performance steels. Experimentally verified nonlinear finite element studies of HPS beams have shown that the affects of cross-sectional compactness and unbraced length contradict the conventional beliefs of the influence of these parameters on structural ductility, as quantified by rotation capacity (Earls 1999). Earls and Shah (2001) demonstrated this to be true in monosymmetric bridge girders designed with HPS grade steel. Earls' research (1999, 2000a,b, 2001) has shown that the rotation capacity of HPS beams is dependent upon two distinct inelastic modal failures; both modes demonstrate local and global buckling interaction. The existence of these two modes is also evident in other studies found in the literature (Azizinamini 1998, Climenhaga et al. 1972, Gioncu et al. 1996). The two modes are referred to by Earls (1999, 2000a,b, 2001) as Mode 1 and Mode 2.

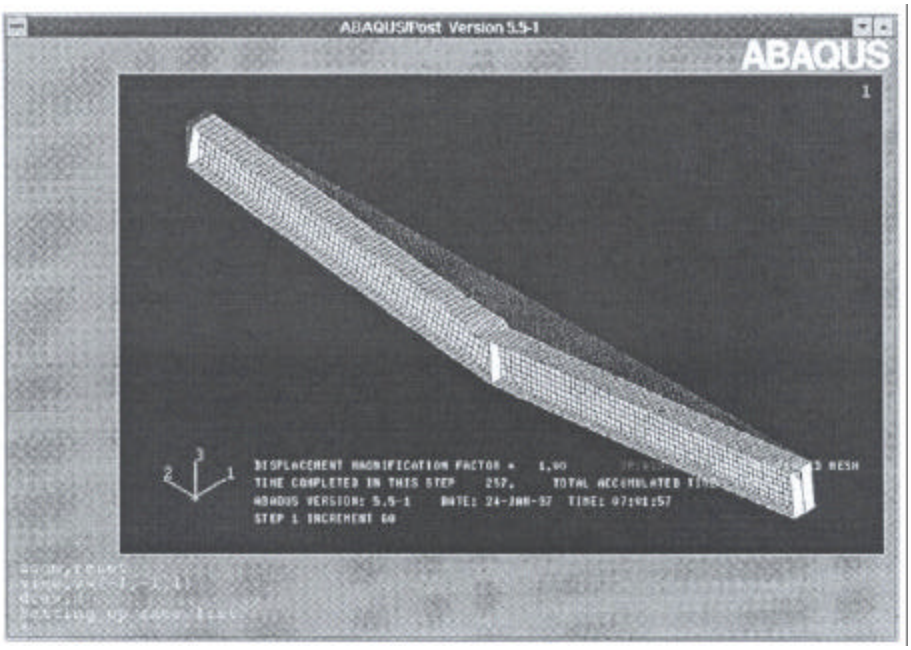

Figure 10 Mode 1 Inelastic Buckling (Earls 1999)

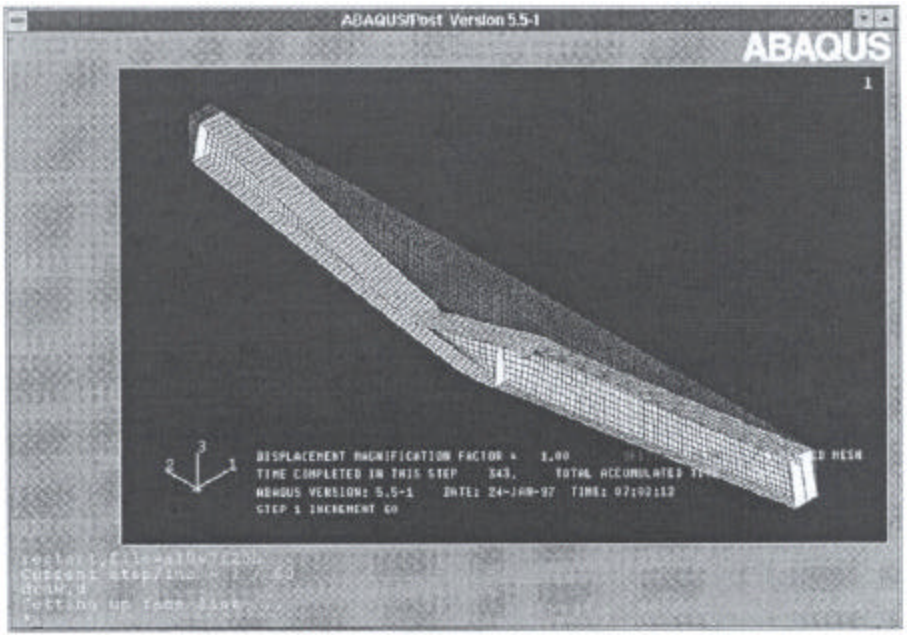

Figure 11 Mode 2 Inelastic Buckling (Earls 1999)

Mode 1 failure was characterized by a localized buckling instability of the flange, either with or without substantial web participation, occurring in close proximity to the mid-span stiffener (most often restricted to one half span of the beam) (Earls 1999). This localized buckling instability usually resulted in only very slight out-of-plane deflections in the compression flange (Earls 2000b). The Mode 1 plastic hinge was shown to be well defined and proximal to the mid-span stiffener (Earls 2000a). Mode 1 failures achieved a higher ultimate moment capacity and exhibited larger cross-sectional rotation capacities as compared with the Mode 2 failures. A typical Mode 1 failure can be seen in Figure 10.

The more severe Mode 2 failure was characterized as a highly asymmetrical inelastic mode shape where local and global buckling is highly coupled (Earls 1999). The flange buckling components, or flange-web buckling components, occurred at a substantial distance from the mid-span. This distance was roughly equal to *d/2*, where *d* is the depth of the beam. Mode 2 failures occurred with substantial out-of-plane deflections between brace points. The out-of-plane deflection was either symmetric or anti-symmetric about the mid-plane stiffener (Earls 1999). There was also an asymmetry in the development of the plastic hinge within the beam (Earls 1999). Earls (1999) described the Mode 2 failure as being a "zone of plastification" rather than a "plastic hinge," which usually defines a tightly formed concentrated zone of plasticity (Earls 1999). Another characteristic feature of the Mode 2 failure was the formation of a mechanism in the compression flange, where the flange behaved as a three-bar-linkage (Earls 1999). A typical Mode 2 failure can be seen in Figure 11.

It is interesting to note that an alternative bracing scheme proved to be effective in preventing this less favorable Mode 2 failure (Earls 1999). This bracing scheme consisted of placing intermediate stiffeners a distance of *d/2* on either side of the mid-span stiffener. This distance of *d/2* was the distance mentioned above where the Mode 2 manifestations took place on average. This bracing configuration provided for a considerable improvement on the inelastic deformation capacity by eliminating the Mode 2 failure.

Earls (2000a) evaluated the use of simple geometric parameters used in the literature and current design specifications in order to identify the transition from one mode to the other in HPS beams. Approaches focusing on beam geometry alone proved to be useful only in a narrow range of beam sizes and steel grades (Earls 2000a). Earls (2000a, 2000b) stated that in order to formulate a method to predict steel I-shaped beam ductility, geometric parameters (i.e. flange slenderness, web slenderness, unbraced length) need to be considered along with certain features of the uniaxial material response representation of the steel.

It was shown that uniaxial material response features such as: yield stress value, magnitude of strain hardening slope, and the presence or absence of a yield plateau, all play fundamental roles in influencing the structural ductility of steel beam response (Earls 2000b). Increasing yield stress led to a decrease in the rotation capacity and ultimate moment capacity of a beam (Earls 2000b). An increase in the strain hardening slope led to increases in both the rotation capacity and ultimate moment capacity (Earls 2000b). Increasing the length of the yield plateau led to an increase in rotation capacity

but a decrease in ultimate moment capacity (Earls 2000b). These results demonstrated the significant influence that the uniaxial material response has on beam flexural behavior. Evidence from this work also showed that the Mode 1/Mode 2 transition emanates from a single bifurcation of the fundamental loading branch in the beam equilibrium curve (Earls 2000b).

This research (Earls 2000b) and the prior research done by Earls (Earls 1999, 2000a) has shown that geometric properties of the beam and material properties of the steel must be considered together in order to formulate a more reliable prediction of the flexural behavior of a homogeneous HPS beam. This will allow for a more favorable Mode 1 failure so that sufficient rotation capacity and ultimate moment capacity can be achieved in HPS beams.

1.2 Scope

The use of high strength steel flanges in hybrid girders has proven to result in a more economical section. The performance qualities of new high performance steel surpass those of the earlier high strength steel while achieving the same high yield stresses. Thus, HPS seems to be an intuitive choice to use in the flanges of hybrid girders. Given the concerns arising from the fact that treating local and global inelastic buckling phenomena separately has been proven to be inadequate in predicting the flexural response of homogeneous HPS girders, the current research will investigate the

influence of HPS flanges on the flexural ductility of hybrid girders, as quantified by rotation capacity.

Experimentally verified nonlinear finite element modeling techniques (Earls and Shah 2001) will be the vehicle used for the present study. Parametric studies will be done on doubly symmetrical hybrid HPS girders in order to investigate the influence of flange slenderness ratios on the girder's flexural ductility, subjected to a moment gradient. This will be done for three different bracing configurations: (1) bracing in accordance with AASHTO design specification; (2) bracing with intermediate stiffeners placed a distance of *d/2* on either side of the mid-span stiffener; (3) bracing with intermediate stiffeners placed a distance of *d* on either side of the mid-span stiffener. The rotation capacity is calculated for each case as per ASCE (1971).

1.3 Overview of Thesis Organization

Chapter 2 provides an overview and discussion of the notion of compactness. The current American steel building and bridge design specifications (AISC 1999, AASHTO 1998) provisions for compactness will be outlined in this chapter as well as the manner in which different steel grades are accounted for in these provisions. Chapter 3 discusses the finite element method employed in this research. Section 3.1 outlines the nonlinear finite element analysis applied to this research with the use of the finite element program ABAQUS. Chapter 4 describes the finite element model that will be analyzed by ABAQUS and the verification study performed in the current study. A detailed

description of the parametric study undertaken herein will be outlined in Chapter 5.0. The results of this parametric study are presented and discussed in Section 5.3. Conclusions from this study are contained in Chapter 6.0.

2.0 NOTION OF COMPACTNESS

The resistance of both homogeneous and hybrid beams in flexure is dependent on the stability effects both locally and globally. If the beam is able to remain stable at high loads, then the beam can develop a bending resistance beyond the first yield moment M_Y and perhaps even attaining its full plastic moment resistance, M_P. If the beam's stability is limited by either local or global buckling then the bending resistance may be less than M_P, and if the buckling is severe, less than M_Y. In order to prevent local or global buckling prior to the attainment of M_P, the beam must be compact and adequately braced (Salmon and Johnson 1996). The term "compact" refers to adequate proportioning of the cross-sectional plate elements of the girder such that M_P can be achieved and maintained through a finite cross-sectional rotation. A compact beam should have adequate rotation capacity for inelastic force redistribution to take place (Yura et al. 1978).

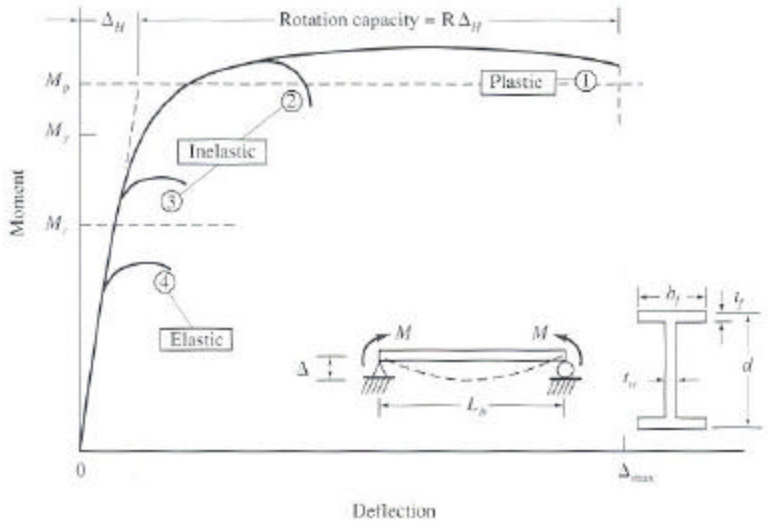

Figure 12 Beam Behavior (Yura, Galambos, and Ravindra 1978)

The behavior of a singly or doubly symmetric beam bent about the strong axis is shown in Figure 12. The beam will ultimately fail with the occurrence of either local buckling of the compression flange, local buckling of the web, or lateral torsional buckling of the member. Due to the sufficient ductility of the grades of steel current American steel building and bridge design specifications (AISC 1999, AASHTO 1998) allow for flexural application involving moment redistribution, failure by tensile rupture will not occur prior to a buckling type failure associated with compression (Yura et. al 1978).

The beam behavior shown in Figure 12 can be classified into 4 categories:

1. The plastic range where the cross section is able to reach the plastic moment, M_P, and maintain this strength through sufficient rotation capacity in order to permit moment redistribution in indeterminate structures (Yura et. al 1978).
2. Inelastic response where plastic moment strength M_P is achieved but little rotation capacity is exhibited, as a result of inadequate stiffness of the flange and/or web to resist local buckling, or inadequate lateral support to resist lateral-torsional buckling, while the flange is inelastic.
3. The inelastic response where the moment strength M_r, the moment above which residual stresses cause inelastic behavior to begin, is reached or exceeded; however, local buckling of the flange or web, or lateral torsional buckling prevent achieving the plastic moment strength M_P.

4. Elastic behavior with moment strength, M_{CR}, being controlled by elastic buckling; any or all of: local flange buckling; local web buckling; or lateral-torsional buckling.

In 1974, the AISC Specification adopted changes in the allowable stress provisions for compact beams, i.e., beams in the plastic zone where moment redistribution is permitted. These new rules for controlling instability were based on the ability of the cross section to reach rotation capacities of three or greater (or stress four times the elastic limit strain) (Yura et. al. 1978). This level of rotation capacity was believed to be sufficient for most civil engineering structures.

When a beam's compression flange is adequately braced against lateral-torsional buckling, local buckling of the flange and/or web will govern the attainment of the beam's plastic moment capacity, *Mp*, and rotation capacities of three or greater (Salmon and Johnson 1996). Local buckling of the beam plate elements can cause premature failure of the entire section, or at least it will cause stresses to become nonuniform and reduce the overall strength of the beam. Thus, current design provisions require that the plate elements (flange and web) be adequately proportioned, or "compact" in applications requiring the attainment of M_P. AISC LRFD (1999) states that compact sections are capable of developing a fully plastic stress distribution and can possess a rotational capacity of approximately 3 before the onset of local buckling (Yura et al. 1978).

The behavior of the compression flange governs the efficiency of an I-shaped cross-section in flexure. The typical behavior of a compressed plate loaded to its ultimate

capacity is illustrated in Figure 13. The stress distribution remains uniform until the elastic buckling stress F_{CR} is reached (assuming elastic-plastic material). Further increase in load can be achieved but the portion of the plate farthest from its lateral edge supports will deflect out of its original plane. The out-of-plane deflection causes the stress distribution to be nonuniform even though the load is applied through ends, which are rigid and perfectly straight. From Figure 13, it can be seen that the plate strength under edge compression consists of the sum of two components; (1) elastic buckling stress represented by (2-1), and (2) post-buckling strength. Post-buckling strength increases as the width-to-thickness ratio b/t becomes larger as illustrated in Figure 13. Plates with low width-to-thickness ratios will have little to no post-buckling strength and may completely yield while reaching a strain-hardening condition, so that F_{CR}/F_Y may become greater than unity (Salmon and Johnson 1996).

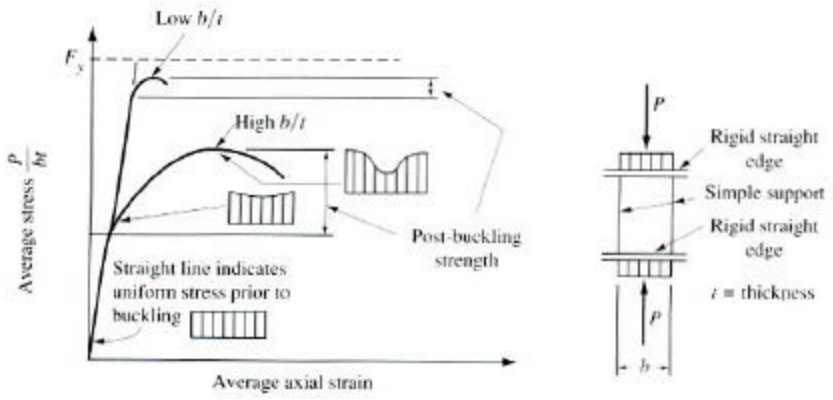

Figure 13 Behavior of Plate Under Edge Compression (Salmon & Johnson)

The behavior of plates in compression is similar to that of columns and the basic elastic buckling expression corresponding to the Euler equation for columns can be expressed as,

$$F_{CR} = k\frac{p^2 E}{12\left(1-m^2\right)\left(b/t\right)^2} \tag{2-1}$$

where k is a constant depending on type of stress, edge conditions, and length to width ratio; μ is Poisson's ratio, and b/t is the width-to-thickness ratio as shown in Figure 14. Plate compression elements can be separated into two categories: (1) stiffened elements; those supported along two edges parallel to the direction of compressive stress; and (2) unstiffened elements; those supported along one edge and free on the other edge parallel to direction of compressive stress (Salmon and Johnson 1996). From the previous definitions, the flange is considered an unstiffened element and the web is considered to be a stiffened element (Figure 14). Various degrees of edge rotational restraint for plates under uniform edge compression are represented in Figure 15, which depicts the variation in k as a function of aspect ratio a/b for most of the idealized edge conditions.

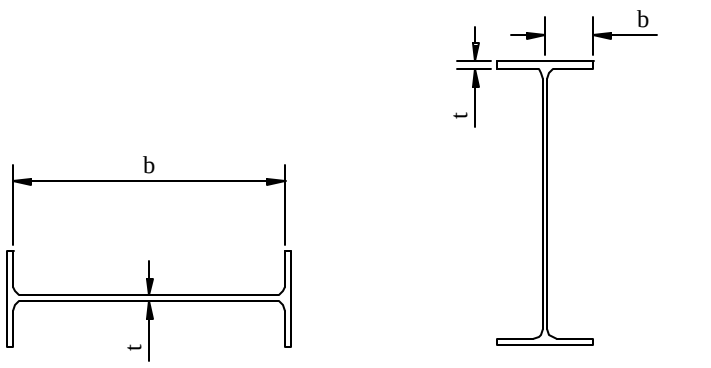

Figure 14 Stiffened and Unstiffened Compression Elements

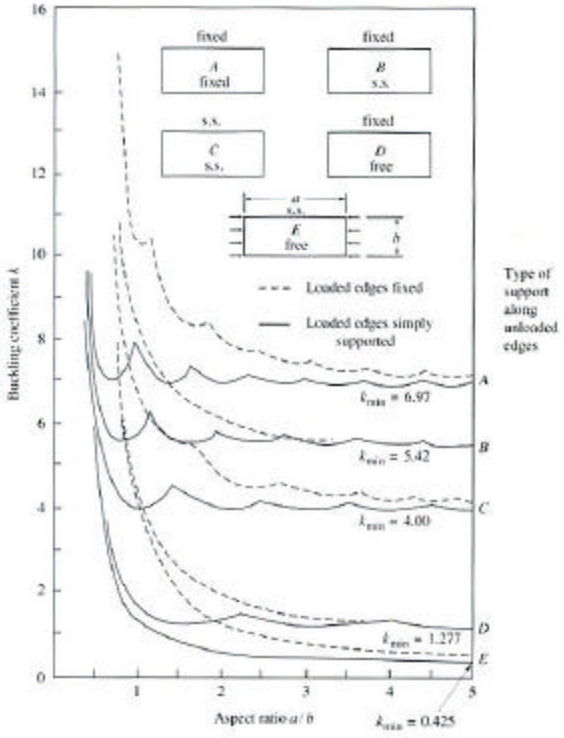

Figure 15 Elastic Buckling Coefficients for Compression in Flat Rectangular Plates (Salmon & Johnson)

The behavior of plates without residual stress is shown in Figure 16. F_{CR}/F_Y is defined as $1 / ?^2$ and (2-1) for plates becomes,

$$l_C = \frac{b}{t}\sqrt{\frac{F_y(12)(1-m^2)}{p^2 Ek}} \qquad (2\text{-}2)$$

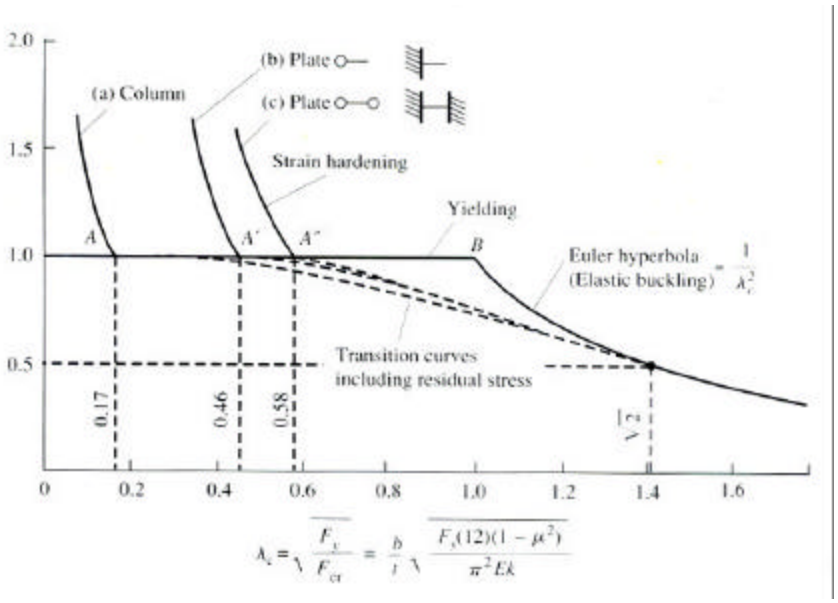

Figure 16 Plate Buckling Behavior (Salmon & Johnson)

Plates with a low *b/t* value may achieve strain hardening without buckling occurring. Inelastic buckling considering residual stresses and initial imperfections is represented by a transition curve for plates with medium values of *b/t*. For large *b/t* values, buckling occurs in accordance with (2-1). It can be seen that the important factor that determines $?_0$ (the value of $?_C$ at which strain hardening commences) is whether the plate element (i.e. flange or web) is supported along one or both edges parallel to loading.

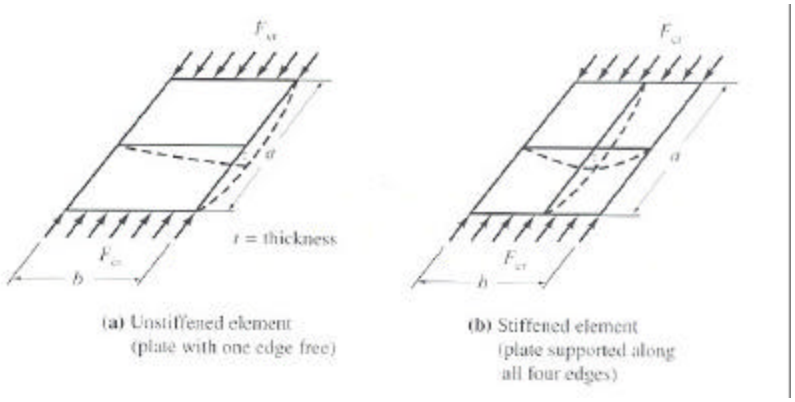

Figure 17 Buckled Deflection of Uniformly Compressed Plates (Salmon & Johnson)

The flange and/or web plate elements of a cross-section may buckle locally prior to the achievement of the cross section's ultimate capacity, *Mp*. In order for a beam to attain M_P, the flange and/or web might be required to undergo significant plastic strain without having local buckling occur (Yura et al. 1978). The buckled deflection of the flange (unstiffened element) and the web (stiffened element) are shown in Figure 17. The lower the width-to-thickness ratio, the greater the compressive strain *e* that can be absorbed by the plate element without buckling. Therefore, $?_C$ must be restricted so not to exceed $?_0$ if strain hardening is to be reached without plate buckling. From Figure 16, it is shown that $?_0$ should not exceed 0.46 for unstiffened compression elements and 0.58 for stiffened compression elements.

The requirement that a plate element achieve yield stress without local buckling is given as

$$F_{CR} = k\frac{p^2 E}{12\left(1-m^2\right)\left(b/t\right)^2} \geq F_y \tag{2-3}$$

Using μ = 0.3 for steel, and E = 29,000,000 psi and F_Y in psi, and solving for b/t yields

$$\frac{b}{t} \leq 5120\, l_C \sqrt{\frac{k}{F_y}} \tag{2-4}$$

For an unstiffened plate $?_C$ should equal 0.46, which is the value of $?_0$ that is required to ensure strain hardening, (2-4) yields,

$$\frac{b}{t} \leq 74.3 \sqrt{\frac{k}{F_y, ksi}} \tag{2-5}$$

Using the lowest value of k for an unstiffened plate from Figure 14 (k = 0.425), (2-5) gives

$$\frac{b}{t} \le \frac{48.5}{\sqrt{F_y, ksi}} \tag{2-6}$$

It should be noted that the strain at the onset of strain hardening is 15 to 20 times e_y, it should be further pointed out that the extreme fiber strain in a fully plastified cross section exhibiting a rotation capacity of 3 is on the order of 7 to 9 times e_y, hence the current American steel building and bridge design specifications (AISC 1999, AASHTO 1998) liberalize, somewhat arbitrarily, this limit to be

$$\frac{b}{t} \le \frac{65}{\sqrt{F_y, ksi}} \quad \text{or} \quad \frac{b}{t} \le \frac{171}{\sqrt{F_y, MPa}} \tag{2-7}$$

Equation (2-7) is the width-to-thickness limit, specified by the AISC LRFD (1999) Table B5.1 for "compact" flanges in order to permit M_P and a rotation capacity of at least 3.0.

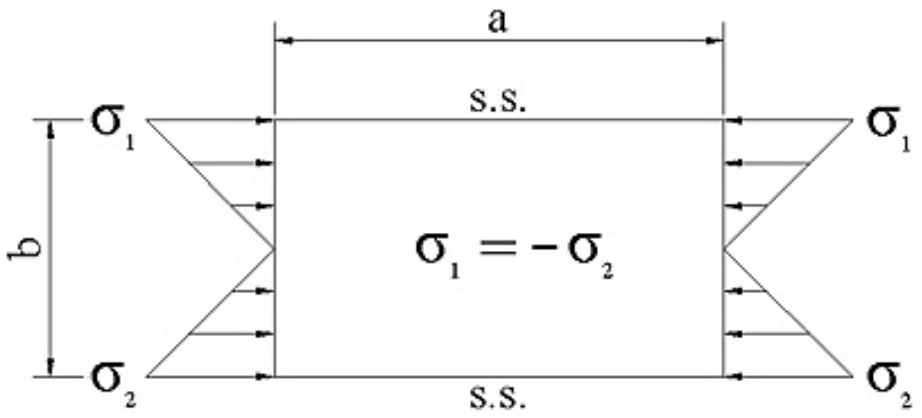

Figure 18 Simply Supported Plate Element Under Pure Bending

For a stiffened plate (i.e. web) element $?_C$ =0.58, which is the value of $?_0$ that is required to ensure strain hardening for this particular element, (2-4) yields

$$\frac{b}{t} \le 93.7\sqrt{\frac{k}{F_y, ksi}} \tag{2-7}$$

The web of an I-section is a plate element whose edges are simply supported along two edges parallel to the applied bending stress as shown in Figure 18. For this case, *k* is equal to 23.9. Using this value in equation (2-7) yields,

$$\frac{b}{t} \le \frac{458.4}{\sqrt{F_y, ksi}} \tag{2-8}$$

Tests have shown that welded girders with thin unstiffened webs and *b/t* up to 125 can reach M_P, but the rotation capacity may be affected when shear stresses exceeded the web buckling strength (Yura et al. 1978). Based on this test data, it was found that the web slenderness limit, (2-9), would permit M_P and a rotation capacity of at least 3.0.

$$\frac{b}{t} \le \frac{640}{\sqrt{F_y, ksi}} \quad \text{or} \quad \frac{b}{t} \le \frac{1681}{\sqrt{F_y, MPa}} \tag{2-9}$$

Thus, (2-9) is the width-to-thickness limit, specified by the AISC LRFD Table B5.1 for a compact web.

The AISC LRFD (1999) classifies steel sections as compact, noncompact, or slender-element sections. For an I-shaped homogeneous member to qualify as compact the flanges must be continually connected to the web and the width-to-thickness ratios of compression plate elements must not exceed the limiting values given in (2-7) and (2-9) as per LRFD Table B5.1. For flanges of I-shaped homogeneous members, AISC LRFD specifies the width *b* of (2-7) to be half the full-flange width, b_f. For webs of built up I-sections, *h* (*b* in (2-9)) is the distance between adjacent lines of fasteners or the clear distance between flanges when welds are used in built-up members: *h* is equal to the clear distance between flanges minus the fillet radii in rolled members.

The commentary for AISC LRFD (1999) Chapter B states, “The definitions of the width and thickness of compression elements agree with the 1978 AISC ASD Specification with minor modifications. Their applicability extends to sections formed

by bending and to unsymmetrical and hybrid sections." According to AISC LRFD (1999), to qualify as a hybrid girder, the flanges at any given section shall have the same cross-sectional area and be made of the same grade of steel. Hybrid I-shaped sections subjected to pure bending are treated in the same manner as homogeneous sections by AISC LRFD. However, *Fy* in both (2-7) and (2-9) is the yield stress of the compression flange; the web yield stress does not affect the limiting width-thickness ratio for compression elements as per LRFD Table B5.1.

The AASHTO LRFD Specification (1998) provisions for I-sections in flexure are contained in Section 6.10 of the publication. The provisions of this section apply to the flexure of rolled or built-up straight steel I-sections symmetrical about the vertical axis in the plane of the web. The AASHTO LRFD Specification states, "Hybrid sections consisting of a web with a specified minimum yield strength lower than one or both of the flanges may be designed under these specifications." The provisions apply to compact and noncompact sections. The depth-to-thickness limit specified in AASHTO LRFD (1998) Section 6.10.4.1.2 for compact-section web slenderness in both homogeneous and hybrid cross sections is given as

$$\frac{2D_{cp}}{t_w} \le 3.76\sqrt{\frac{E}{F_{yc}}} \qquad (2\text{-}10)$$

where D_{cp} = depth of the web in compression at the plastic moment (inches or millimeters), F_{yc} = specified minimum yield strength of the compression flange (ksi or

MPa), and t_w = the thickness of the web (inches or millimeters). Equation (2-10) is essentially the same as (2-9). The width-to-thickness limit specified in AASHTO LRFD (1998) Section 6.10.4.1.3 for compact-section flange slenderness in both homogeneous and hybrid cross-sections is the same as (2-7), where *Fy* is the yield strength of the compression flange.

If the actual web slenderness and/or flange slenderness is greater than 75 percent of their respective limit, AASHTO LRFD (1998) requires the satisfaction of a compact section web and compact section flange interaction equation given in Section 6.10.4.1.6 as,

$$\frac{2D_{cp}}{t_w} + 9.35\left(\frac{b_f}{2t_f}\right) \leq 6.25\sqrt{\frac{E}{F_{yc}}} \qquad (2\text{-}11)$$

This is done by the AASHTO LRFD Specifications because moment-rotation test data found in the literature suggests that compact sections may not be able to reach the plastic moment when the web and compression-flange slenderness ratios both exceed 75 percent of the limits given in (2-7) and (2-10), respectively (AASHTO-LRFD 1998). Once (2-7), (2-10), and (2-11) are satisfied, the homogeneous or hybrid member is compact according to the AASHTO LRFD Specifications (1998).

Assuming that a girder is adequately braced against lateral-torsional buckling, the provisions for cross-sectional compactness given by the current American steel building and bridge design specifications (AISC 1999, AASHTO 1998) ensure that the girder

cross-sectional plate elements will be able to undergo significant plastic strain without having local buckling occur.

3.0 FINITE ELEMENT ANALYSIS

The objective of the current study is to investigate the effect HPS flanges have on hybrid girder flexural ductility. This includes the attainment of the cross-section's plastic moment and its ability to maintain this capacity through some amount of rotation capacity. This investigation requires a full plot, both loading and unloading, of the girders moment versus rotation response as shown in Figure 2. In order to achieve this plot a nonlinear displacement based finite element analysis is performed. A nonlinear analysis is used rather than a linear analysis, since the girder will undoubtedly show nonlinear behavior prior to reaching its ultimate capacity.

The two important nonlinearities within structural analysis are material nonlinearity and geometric nonlinearity. These nonlinearities are produced by finite deformations coupled with changes in material stiffness under applied loading. Both nonlinearities are germane to the current study in that they are associated with the inelastic global and local buckling phenomenon (Earls 1999). Geometric nonlinearity governs in a situation where it is inappropriate to formulate equilibrium in terms of the undeformed state of the structure (i.e. integration of the constitutive rate equations is required). Material nonlinearity is defined when the material undergoes plastic deformation.

The commercial multipurpose finite element software package ABAQUS is employed in this research. ABAQUS has the ability to treat both geometric and material nonlinearity that may rise in a given model.

The Finite Element Method (FEM) is a numerical method for analyzing complex problems of engineering and mathematical physics. A body, in this case a beam, is discretized into an equivalent system of smaller bodies (finite elements) interconnected at points common to two or more elements (nodal points or nodes). The formulation of the problem results in a system of simultaneous algebraic equations which yield approximate values of the unknowns (i.e. displacements) at the discrete points in the continuous body. These values at the discrete points are then combined to obtain a solution for the whole body. In the displacement based FEM, it is paramount that discontinuities between elements not develop and elements must not overlap or separate so as to preserve the compatibility between the elements.

The solution of the whole body for structural problems typically refers to determining the displacements at each node and the stresses within each element making up the structure that is subjected to the applied loads. Therefore, an extremely thorough examination of the body's behavior (i.e. deformations, yielded areas, etc.) may be achieved via the use of a refined finite element study; referring to a body with a large amount of discrete elements.

3.1 Nonlinear Finite Element Analysis

The primary objective of a nonlinear analysis is to find the state of equilibrium of a structure corresponding to set of applied loads. In such a nonlinear analysis, the solution cannot be calculated by solving a single system of linear equations but rather the

solution is found by specifying the loading as a function of time and incrementing time in small steps, so as to trace nonlinear equilibrium response.

In the incremental method, each step of the finite element analysis is assumed to be linear with the loading or displacement applied in a series of increments. A new configuration of the structure, a beam in the case of the present study, is defined each time a new displacement increment is computed and added to previous calculated displacements. Changes in the beam are observed through each new configuration.

In nonlinear analysis the tangent stiffness matrix is used as a means for relating changes in load with changes in displacement. The tangent stiffness matrix depends only upon the internal forces and deformation at the beginning of each load increment. The tangent stiffness matrix maybe represented by,

$$[k_T] = [k_0] + [k_p] \tag{3-1}$$

where matrix $[k_0]$ is the conventional linear stiffness matrix for uncoupled bending and axial behavior and matrix $[k_p]$ is the initial stiffness matrix that depends upon the axial force at the beginning of each load increment.

3.1.1 Nonlinear Equilibrium Equation

The principle of virtual work is stated as follows:

> If a deformable body in equilibrium is subjected to arbitrary virtual (imaginary) displacements associated with a compatible deformation of the body, the virtual work of external forces of the body is equal to the virtual strain energy of the internal stresses.

In the principle, compatible displacements are those that ensure that no discontinuities, such as voids or overlaps, occur within the body (Logan 1993) in addition to satisfying the kinematic boundary conditions.

Applying the principle of virtual work to the finite element method gives,

$$dU^{(e)} = dW^{(e)} \tag{3-2}$$

where $dU^{(e)}$ is the virtual strain energy due to internal stresses and $dW^{(e)}$ is the virtual work of external forces on the element. The virtual strain energy may be expressed as,

$$dU^{(e)} = \iiint_V de^T s \, dV \tag{3-3}$$

where s is assumed to be an arbitrary stress measure and similarly e is assumed to be and arbitrary strain measure. It is noted that s and e must be work conjugate. Equation (3-3) shows that internal strain energy is due to internal stresses moving through virtual strains, de. The external work is due to nodal, surface, and body forces moving through virtual displacements. It is implied in (3-3) that the final deformed configuration of the structure is used as the basis for computing the magnitudes and directions of the corresponding stress and stain measures. In the case of nonlinear finite element analysis this assumption constitutes a problem because the configuration of the structure in the deformed state is unknown. Hence, a Lagrangian reference frame is chosen for the formulation of the nonlinear finite element equilibrium equations which always refers to a previous equilibrium configuration and as such is quite suitable for use in nonlinear finite element problems. There are two fundamental Lagrangian reference frames, the Total and the Updated.

3.1.1.1 Lagrangian Reference Frames. In the case of the Total Lagrangian reference frame, all material responses in the current deformed state are referred back to the initial configuration. The initial configuration of the structure is defined as the configuration prior to the first load step. The Green-Lagrange strain and Second Piola-Kirchhoff stress used in this formulation must have the initial configuration as their reference frame. The Updated Lagrangian reference frame is quite similar to the Total Lagrangian reference frame except that the material response of the structure in the current configuration is referred back to the previous equilibrium configuration.

3.1.2 Nonlinear Equilibrium Solution Techniques

In the current study, incremental solution strategies are necessary to properly trace the nonlinear equilibrium path of the inelastic hybrid girder in order to observe its complete behavior. An important issue that arises with the use of an incremental solution is how (3-2) is to be solved at each increment (ABAQUS 1999).

There are several incremental methods such as the load control method, displacement control methods, work control methods, and arc-length methods. The two most powerful and widely used incremental techniques for the solution of nonlinear problems are the Newton-Raphson technique, and the Riks (or arc length) method. The Riks method is an arc-length method which is generally used to solve post buckling problems involving unloading response. ABAQUS (1999) generally uses Newton's method as the default solution strategy for solving nonlinear equilibrium equations.

The principal advantage of Newton's method is its quadratic convergence rate when the approximation at a given iteration is within the radius of convergence (ABAQUS 1999). However, this method is unable to negotiate limit and bifurcation points and hence is not suitable to plot the unloading portion of a nonlinear equilibrium path and is therefore inadequate for this study (Earls 1995).

The incremental technique for the solution of the nonlinear problem at hand will be the modified Riks-Wempner method provided in the ABAQUS program. The Riks-Wempner method is able to trace the nonlinear equilibrium path even into the unloading regime in the structural response of beams. In addition, this method also provides some

of the most efficient use of the computational resources during the nonlinear solution process.

3.1.2.1 The Modified Riks-Wempner Method with Variable Stiffness Matrix. It is often necessary to obtain nonlinear static equilibrium solutions for unstable problems, where the load-displacement response can exhibit the type of behavior sketched in Figure 19. This type of behavior exhibits, during periods of the response, a possible decrease in the load and/or displacement as the solution evolves. The modified Riks method is an algorithm used by ABAQUS that allows an effective solution of such cases. This is accomplished by using the "arc length", along the static equilibrium path in load-displacement space. This approach provides solutions regardless of whether the response is stable or unstable.

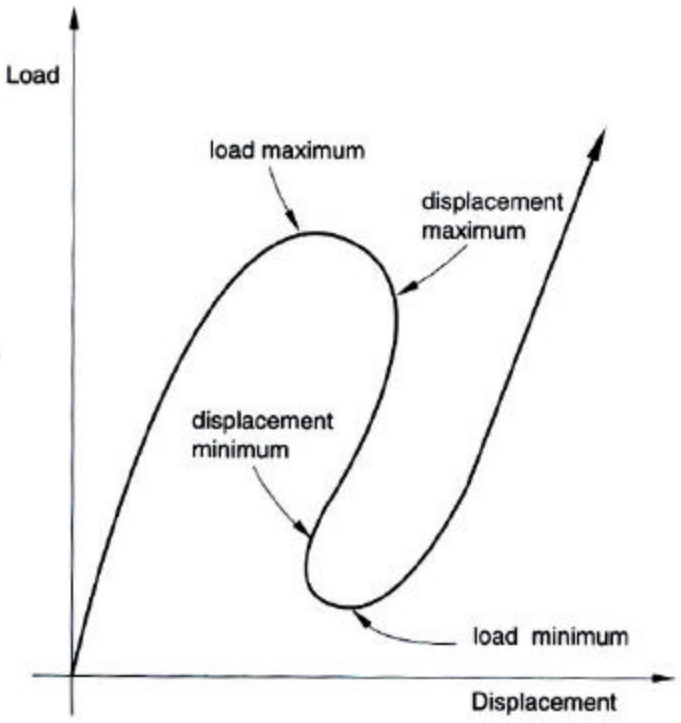

Figure 19 Typical Unstable Static Response (ABAQUS 1999)

A brief and cursory description of the Riks-Wepner follows (Earls 1995). The load whose magnitude is defined in the Riks card is referred to as a "reference" load. All prescribed loads are ramped from the initial (dead load) value to the reference values specified. In other words, the loading during a Riks step is always proportional. A description of the Riks step is given (Earls 1995). The current load magnitude, P_{total} , is defined by

$$P_{total} = P_0 + l\,(P_{ref} - P_0) \tag{3-6}$$

where P_0 is the dead load, P_{ref} is the reference load vector, and ? is the load proportionality factor. The load proportionality factor is found as part of the solution. The Points on an equilibrium path may be quantified by two parameters: a load intensity parameter ρ and a deformation parameter *t* (Riks 1979). In general, more than one deformed configuration may exist for a given load level. This leads to the conclusion that a family of equilibrium curves, for a given structural system, exist in an N+1 dimensional Euclidean space. These curves may be written in parametric form as

$$r = r(h) \; ; \; t = t(h) \tag{3-7}$$

where ? is a suitably chosen path parameter, which is the key to an efficient nonlinear solution strategy. For the case of the modified Riks-Wempner algorithm, the following parametric choice is made,

$$\left(\frac{dr}{dh}\right)^2 + \frac{dt_i}{dh}\frac{dt_i}{dh} = 1 \tag{3-8}$$

The parameter ? can be thought to assume the physical meaning of a measure of arc length associated with an interval on the equilibrium path.

Figure 20 schematically depicts the process associated with the application of the modified Riks-Wempner method to a one-dimensional system. A known equilibrium state exist at point *a* on the curve. The line, *n1*, is tangent to point *a* and possesses a length specified by the application of equation (3-8). The slope of this line is a

representation of the instantaneous system stiffness often referred to in the literature as the tangent stiffness. At a specified approximate arc length, coinciding with point *b* in Figure 20, a line is constructed normal to *n1*. A search is often carried out with a variant of the modified Newton-Raphson algorithm in the space between the actual equilibrium curve and line. The nonlinear equilibrium path in this sub-region between *b* and *c* is arrived at through the direct application of the nodal internal force vector. Point *c* is reached when the difference in the *?* of the normal line (at a particular *t*) and the internal force value at the same time *t* are arbitrarily small as specified by the analyst. A line tangent to the equilibrium path at point *c* is then constructed. This line is designated as *n2* and has a slope determined by the tangent stiffness at point *c*. Similarly, a line parallel to *n1*, emanating from point *c*, is constructed. This line is designated as *N*. The angle, Θ between *N* and *n2* is often chosen as the parameter which governs the magnitude of the arc length to be imposed on the solution for the next equilibrium point. As this angle gets large, the corresponding size of the arc length parameter decreases. This results in smaller load increments, causing a higher resolution to be achieved in tracing of the nonlinear equilibrium path.

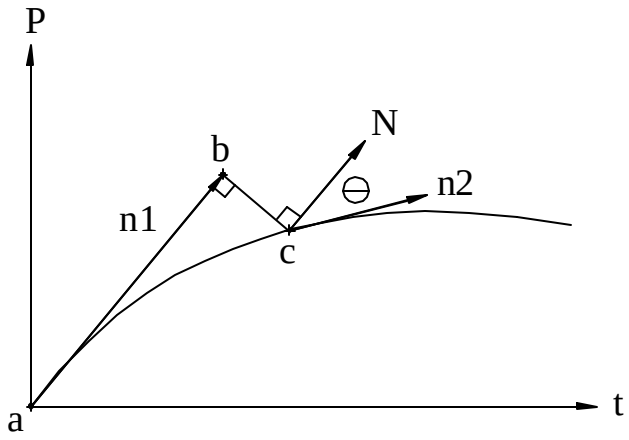

Figure 20 Arc Length Search Strategy (Earls 1995)

3.2 Metal Plasticity

A beam is said to have yielded and to have undergone plastic deformation if the beam does not regain its original shape when an applied load is removed. The resulting deformation that remains is referred to as permanent set prior to spontaneous load shedding. The beam is said to be ductile if its material is able to undergo a large permanent set. If an applied load causes the material to exceed its yield strength, the deformation is no longer fully recoverable. Once the material has yielded, some part of the beam deformation will remain when the load is removed.

Various stress components in three-dimensional space interact to cause yielding and plastic flow in a material. Relationships are required to quantify the interactions between the various loading combinations that cause yielding. This can be accomplished

through a yield function. A yield function includes the effect of all the stress components acting in a system to predict yielding of the material.

ABAQUS offers several models for metal plasticity analysis in order to describe the yield and inelastic flow of a metal. The two main choices are between the Mises yield surface with associated plastic flow for isotropic materials and Hill's yield surface for anisotropic materials (ABAQUS 1999). The models in the current study employ the von Mises yield function in order to model the member yield surface while using isotropic hardening. Most of the plasticity models in ABAQUS are "incremental" theories in which the mechanical strain rate is decomposed into an elastic part and a plastic (inelastic) part. The incremental theory relates the increment of plastic strain to the state of stress and the stress increment. Incremental plasticity (also known as flow plasticity) models are formulated in terms of: a yield surface; a flow rule; and evolution laws that define hardening.

3.2 Yield Surface and Associated Flow Plasticity

The yield function is able to model the plastic behavior of the material at specified increments during the loading and unloading of the beam. The yield surface defines the boundry for the material state of stress within which elastic response occurs. As seen in Figure 21, if $f < 0$ the material is behaving elastically and there is no change in the plastic strain. Since a material cannot achieve a state of stress beyond its yield strength; $f > 0$, is

an invalid state of stress, but $f = 0$ may occur and corresponds to incipient yielding (a consistency condition is required to determine plastification in this situation).

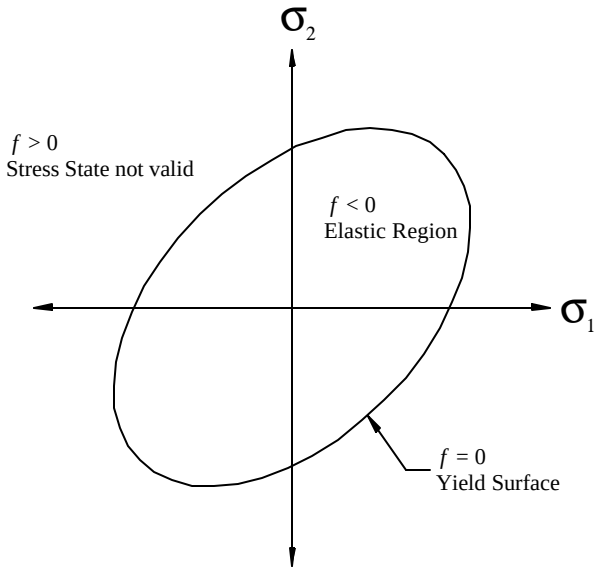

Figure 21 Schematic Yield Surface

If a material is behaving elastically, there is no change in the plastic strain ($\dot{e}_P$=0). Since stress states outside the yield surface are inadmissible, then there can only be change in the plastic strain when the stress point impinges on the yield surface ($f = 0$). When $f = 0$, the material experiences strain in the direction of the applied stress (s), with constant strain rate (?).

In the case of the associated flow plasticity, the evaluation of the change in plastic strain can be completely described for any admissible state of stress ($f = 0$) as

$$\dot{e}_P = g sign(s) \tag{3-9}$$

where *sign(s)* = +1 if $s > 0$ and *sign(s)* = -1 if $s < 0$ (Simo and Hughes 1988). Three loading and unloading conditions must follow. First, in (3-9), s must be admissible and $?$ must be nonnegative. Second, $? = 0$ if $f < 0$. Therefore, $? > 0$ only if $f = 0$. It is required that

$$gf = 0 \tag{3-10}$$

The third and final condition is referred to as the consistency condition which allows the determination of the actual value of $?$ at any given time t (Simo and Hughes 1988). Let $\hat{f}(t)$ be defined as

$$f[s(t)] = 0 \tag{3-11}$$

where $s(t)$ = the stress along any point on the yield surface; in other words, the plastic potential function is the same as the yield function. Therefore at $\hat{f}(t) = 0$, $\dot{\hat{f}}(t) = 0$, since should $\dot{\hat{f}}(t)$ be positive it would imply that $\hat{f}(t)$ is greater than zero which is not possible. Hence, ? > 0 only if $\dot{\hat{f}}(t) = 0$, and ? = 0 if $\dot{\hat{f}}(t) < 0$. Therefore, the consistency condition is given as

$$g\dot{\hat{f}}(t) = 0 \tag{3-12}$$

and corresponds to the physical requirement that for the change in the plastic strain to be nonzero (i.e. ?>0) the applied stress must persist on the yield surface so that $\dot{f}[s(t)] = 0$ (Simo and Hughes 1988).

The von Mises yield criterion is used for the material plasticity definition and is explained briefly in Section 3.3. The Mises yield surface in ABAQUS assumes that yielding of the metal is independent of the equivalent pressure stress, which has been confirmed experimentally for steel.

3.3 Von Mises Criterion

Richard von Mises (1883-1953), a German-American applied mathematician, developed the maximum-distortion-energy criterion. This later came to be known as the von Mises yield criterion. This criterion is based on the determination of the distortional energy in a given material (i.e. the energy associated with the change in shape in the material as opposed to the energy associated with the change in volume of the same material). According to this criterion, a given structural component is elastic as long as the maximum value of the distortion energy per unit volume in that material remains smaller than the distortion energy per unit volume required to cause yield; such values may be obtained experimentally.

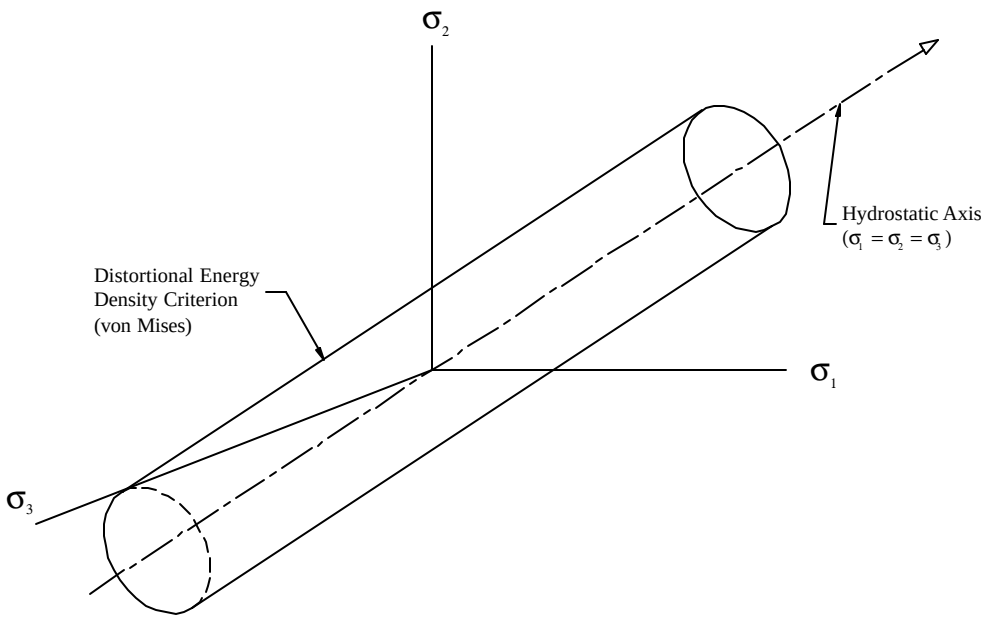

Figure 22 Yield Surface in Principal Stress Space

The von Mises yield condition assumes that only the deviatoric component of the strain tensor is associated with initiation and propagation of plastic flow (Boresi & Sidebottom 1993). The hydrostatic stress has no influence on the yielding of the material. Thus, the von Mises yield criterion forms a cylinder encompassing the entire hydrostatic axis. The radius of the cylinder represents the deviatoric component of the strain tensor associated with initiation and propagation of yielding in the material.

The distortional energy per unit volume, or the distortional strain energy

density, can be obtained from the total strain energy density, U_O. The total strain energy density can be broken into two parts: one part that causes volumetric change, U_V and one that causes distortion, U_D.

$$U_O = \frac{(s_1 + s_2 + s_3)^2}{18K} + \frac{(s_1 - s_2)^2 + (s_2 - s_3)^2 + (s_3 - s_1)^2}{12G} \qquad (3\text{-}13)$$

The first term on the right side of (3-13) is U_V, the strain energy that is associated with the pure volume change where K is the bulk modulus ($K=E/[3(1-2\nu)]$). The second term is the distortional strain energy density

$$U_D = \frac{(s_1 - s_2)^2 + (s_2 - s_3)^2 + (s_3 - s_1)^2}{12G} \qquad (3\text{-}14)$$

where G is the shear modulus. In von Mises' yield criterion, the initiation of plastic flow coincides with the deviatoric strain energy density reaching a predetermined level.

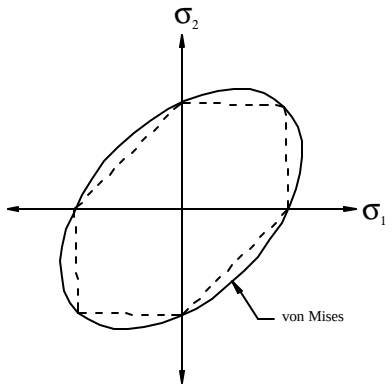

Figure 23 Yield Surface for biaxial stress state ($s_3 = 0$)

Under a uniaxial stress state ($s_1 = s$, $s_2 = 0$, $s_3 = 0$) at yield, $U_D = U_{DY} = s_Y^2/6G$. Thus, for a multiaxial stress state, the distortional energy density criterion states that yielding is initiated when the distortional energy density U_D given by (3-14) equals $U_{DY} = s_Y^2/6G$, or, failure occurs when the energy of distortion reaches the same energy for yield/failure in uniaxial tension. It is assumed that the strain tensor e_{ij} can be divided into an elastic and plastic part. Thus for an increment, de_{ij} can be expressed as

$$de_{ij} = de_{ij}^{e} + de_{ij}^{p} \tag{3-15}$$

The ellipse represents the yield surface boundary. The area within the ellipse corresponds to the material behaving elastically and anything outside of the ellipse corresponds to yielding of the material. In essence, this is what ABAQUS does when it asks for the uniaxial material response to be described with cards in the input deck. A brief description of this process is given (Earls 1995):

Abaqus uses a yield function, f, to define the limits of elastic material response. This general form of the yield function has the form

$$f(s, q, H_a) < 0 \tag{3-16}$$

which describes a purely elastic response. In (3-16), s represents stress, *?* represents temperature, and H represents hardening parameters (of which the a subscript is

associated with the particular type of hardening being used). In the case of the von Mises metal plasticity model of ABAQUS, only one such parameter, s, is used. In ABAQUS, when material is flowing plastically, the inelastic flow rule is described by

$$de^{pl} = d\lambda \frac{\partial g}{\partial s} \tag{3-17}$$

In equation (3-17), $g(s, ?, H_\alpha)$ is the flow potential, and $?$ is time, for a rate dependent problem, or a scalar whose value is determined by the requirement of the consistency condition $f = 0$, in the case of rate independent models (such as von Mises metal plasticity). Also in the ABAQUS von Mises metal plasticity model, the direction of flow coincides with the direction of an outward normal to the yield surface constructed at the point of intersection in principal stress space. This condition is represented mathematically as

$$\frac{\partial g}{\partial s} = c\frac{\partial f}{\partial s} \tag{3-18}$$

This type of flow rule is often referred to as associated flow by the literature. It works very well for materials in which dislocation motion provides the fundamental mechanism for plastic flow and where there are no sudden changes in the direction of the plastic strain rate at a point (ABAQUS 1999).

3.4 Implementation of Metal Plasticity in ABAQUS

True-stress versus true-strain (logarithmic stain) characteristics of the material are used in nonlinear finite element analysis since nonlinear element formulations permit the consideration of updated structural configurations. Engineering stress-strain response does not give a true indication of the deformation characteristics of a structural steel because it is based entirely on the original dimensions of a given specimen. Ductile materials, such as steel, exhibit localized geometric changes and therefore, the relevant stress and strain measures are different from the measured engineering stress and strain values. Figure 24 illustrates the true stress-true strain curve. Specific values for the various steels used in the current study will be discussed in Chapter 4.

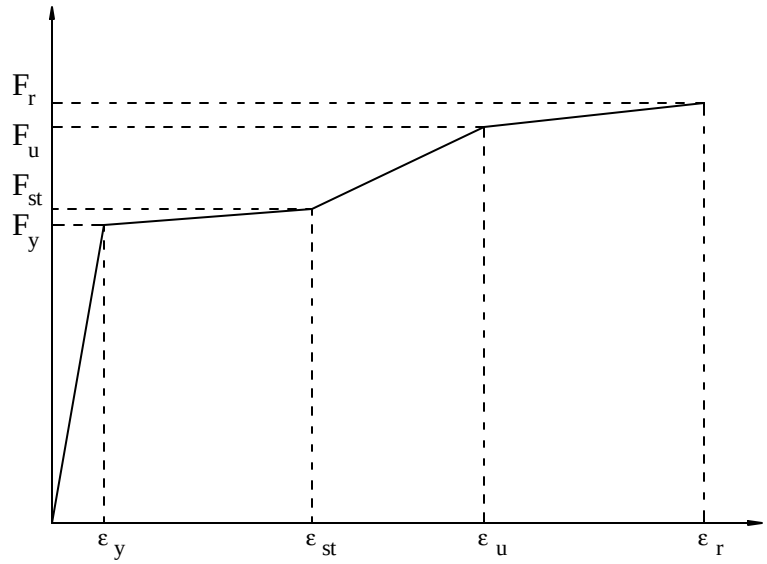

Figure 24 Constitutive Law – True Stress versus True Strain (Logarithmic Strain)

A uniaxial representation of the constitutive law is placed into the ABAQUS input deck in terms of true-stress and true-strain. A yield surface in three-dimensional principal stress space is extrapolated from this information using the von Mises yield criterion as discussed in Section 3.3 of the current study.

3.5 Shell Element Type

A nonlinear shell element is chosen for this study so as to be able to explicitly model local buckling deformations and the spread of plasticity effects. A shell element is suitable for "thick" or "thin" shell applications utilizing reduced integration. Earls and Shah (2001) considered both the S4R and S9R5 shell elements from the ABAQUS element library in their verification work. This verification study showed that the S4R element showed a better agreement with the experimental work used in the verification study (Earls and Shah 2001). Thus, the models considered in the current study are constructed from a mesh of S4R shell finite elements. The S4R element is defined by ABAQUS (1999) as a 4-node, doubly curved general-purpose shell, with; reduced integration, hourglass control, and finite member strains".

Five aspects of an element characterize its behavior (ABAQUS 1999):

1. The element family
2. Degrees of freedom (directly related to the element family)
3. Number of nodes
4. Formulation

5. Integration

The S4R element belongs to the "shell" family. There are two types of shell elements; "thick" and "thin." Thick shells are needed in cases where transverse shear flexibility is important and second-order interpolation is desired (ABAQUS 1999). Thin shells are needed in cases where transverse shear flexibility is negligible and the Kirchhoff constraint must be satisfied accurately (i.e., the shell normal remains orthogonal to the shell reference surface) (ABAQUS 1999). The S4R is a 4-noded, general purpose element which allows for thickness changes. The S4R uses thick shell theory as the shell thickness increases and become Kirchhoff thin shell elements as the thickness decreases; the transverse shear deformation becomes very small as the shell thickness decreases. This is paramount in the current study due to the varying flange thickness from model to model as will be discussed in Chapter 5.0. In addition, the S4R is suitable for large-strain analysis involving materials with a nonzero effective Poisson's ratio.

The degrees of freedom for a shell element are the displacements and rotations at each node. The active S4R degrees of freedom are shown below:

1, 2, 3, 4, 5, 6 (ux, uy, uz, f x, f y, f z)

The S4R element uses reduced integration to form the element stiffness. In the reduced integration technique, the order of in-plane integration is one integration

order less than that which would require performing the stiffness matrix integration exactly. Reduced integration usually provides results that are more accurate (provided the elements are not distorted or loaded in in-plane bending) and significantly reduces running time, especially in three dimensions (ABAQUS 1999). The S4R is computationally inexpensive since the integration is performed at one Gauss point per element.

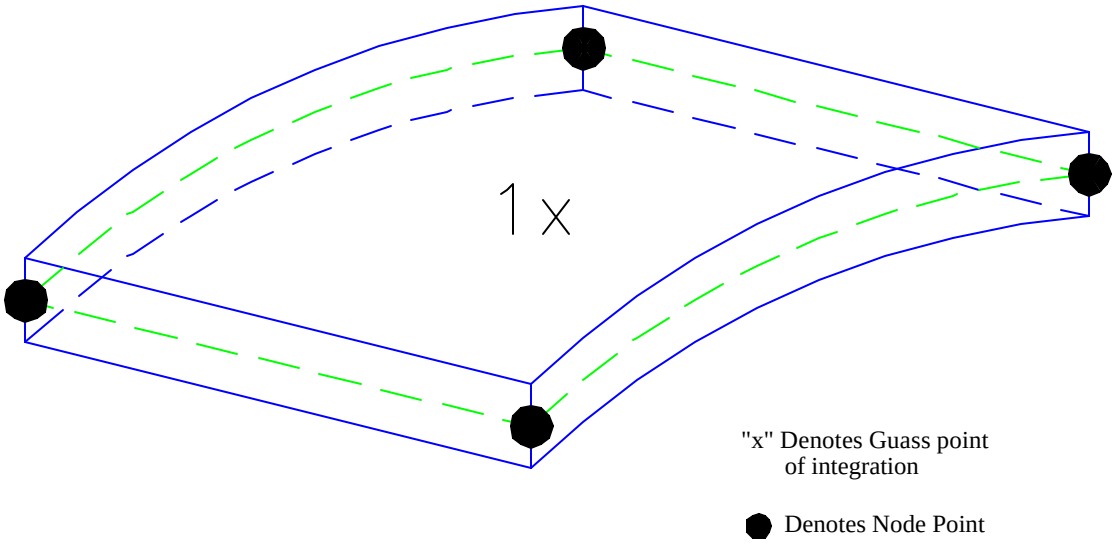

Figure 25 S4R Element: Shell Element, 4-Nodes, Reduced Integration

4.0 FINITE ELEMENT MODEL

The current study involves an analytical investigation of the effect that HPS flanges have on hybrid girder flexural ductility. The finite element modeling reported herein employs the commercial, multipurpose finite element software package ABAQUS. This chapter will serve to describe, in detail, the hybrid girder finite element model used for the parametric study outlined in Chapter 5. The hybrid girder is discretized into 58,732 finite elements, 60,817 nodes, a geometry based closely on the experimentally verified models of Earls and Shah (2001). As in Earls and Shah (2001), a moment gradient loading is achieved by applying a point load at the midspan of the simply supported girder configuration.

Earls and Shah (2001) used experimentally verified nonlinear finite element modeling techniques in order to carry out a parametric study on the influence that flange and web compactness have on homogeneous HPS bridge girder rotation capacity. The model was created in accordance with the dimensions of a subject bridge selected from the New York State Thruway Authority.

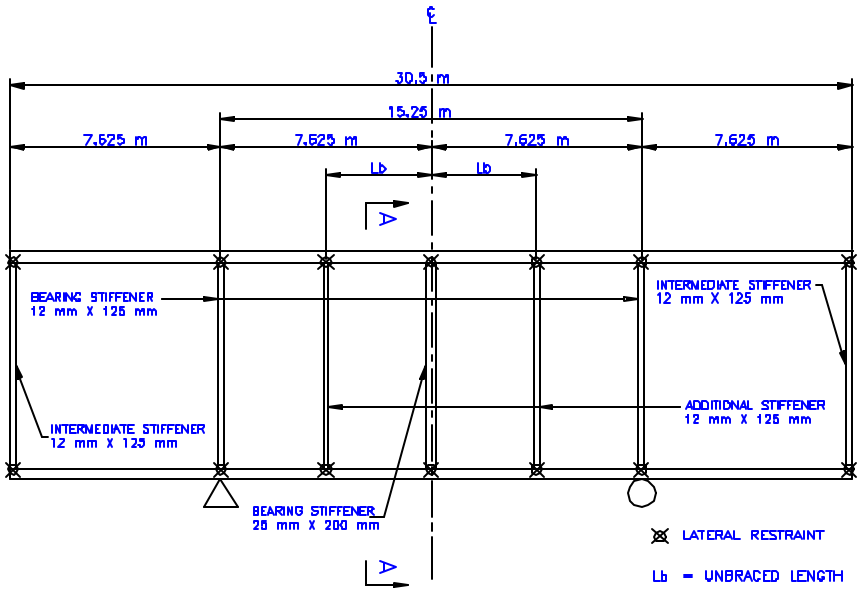

MODEL ELEVATION VIEW
NOT TO SCALE

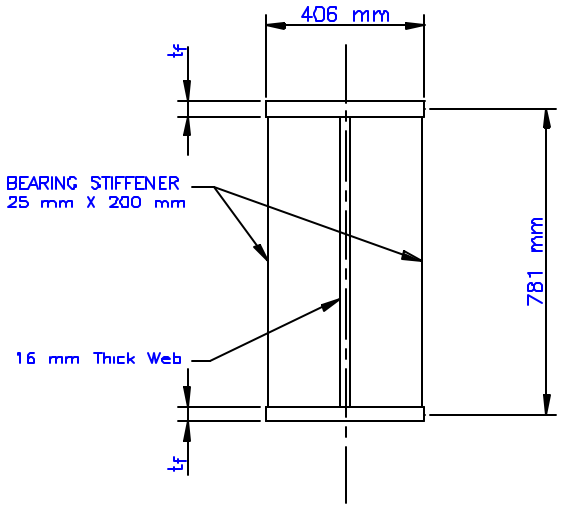

SECTION A–A

Figure 26 Finite Element Model Dimensions

4.1 Finite Element Model Geometry

The analytical model used in the current study is a representation of a simply supported doubly symmetric hybrid girder subjected to a point load at midspan, which in turn, produces a moment gradient. Figure 26 shows an elevation and cross-sectional view of the model geometry. The hybrid girder model has a total length of 30.5 meters (m) and a depth of 0.781m from the center of the top flange to the center of the bottom flange. The hybrid girder model cross-sectional dimensions remaining constant throughout the parametric study reported in Chapter 5 are the flange width and the web thickness, which are 406 millimeters (mm) and 16mm, respectively (Figure 24). The flange thickness is varied in the parametric study described in Chapter 5. The change in thickness of the flange causes the height of the web to change accordingly (which is explained in Section 4.2), maintaining the web slenderness ratio (h/t_w) at roughly 45.

The distance (L) between the two supports is 15.25m as shown in Figure 26. The hybrid girder model has a 7.625m ($L/2$) overhang at each support, which was included to represent a portion of continuous bridge girders between adjacent inflection points at an interior support in the Earls and Shah (2001) model. This overhang will help simulate torsional warping restraint provided by adjacent beam segments in an actual continuous bridge girder. The overhang length was chosen in the Earls and Shah (2001) model to correspond to the distance of the next diaphragm member occurring after the point of inflection in a continuous bridge girder (Earls and Shah 2001).

Bearing and transverse stiffeners are present along the longitudinal axis of the hybrid girder analytical model on both sides of the web. The support bearing stiffeners are provided as 12mm thick and 200mm wide plates. A 25mm thick and 200mm wide, bearing stiffener is provided at the point load. The ends of the overhang beam segments are modeled with 12mm thick and 200mm wide plate intermediate stiffeners. Additional stiffeners, 12mm thick and 200mm wide, are used to model various bracing schemes that will be discussed in Chapter 5. The stiffener dimensions remain constant throughout the entire study. All stiffeners are provided for the entire height of the web and are braced against out-of-plane translation in an idealized way in order to reduce the number of parameters observed in the current study (i.e. remove bracing stiffness from consideration). This idealized bracing is achieved by specifying rigid supports at the top and bottom of the stiffeners orthogonal to the longitudinal axis (see Figure 26). Figure 27 illustrates the idealized bracing in the analytical model.

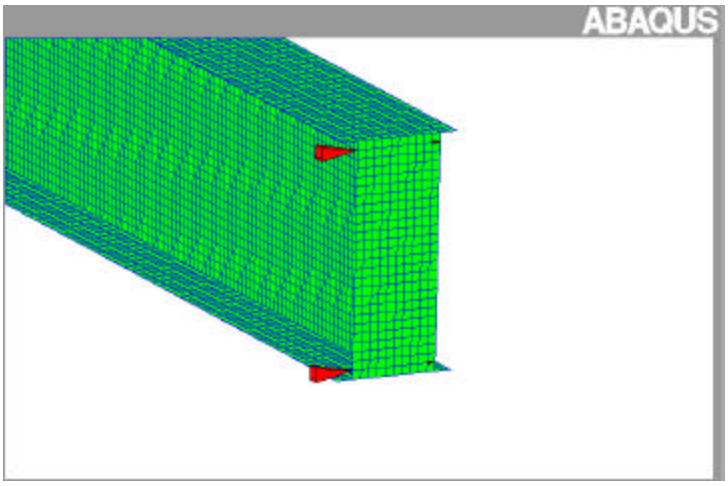

Figure 27 Illustration of Stiffener Idealized Bracing

4.2 Finite Element Mesh

The hybrid girder analytical model constructed for this study is built from a dense finite element mesh of the ABAQUS S4R element described in Section 3.5. The mesh density is directly related to computational time and also related to modeling accuracy. These two concerns must be balanced in order to achieve accurate results at both the global and local level without consuming an impractical amount of computation time. The finer the mesh is constructed, the more accurate the results will be but with a greater computational expense. Due to recently purchased high-speed scientific computing systems, for use with this research, very dense meshes can be used efficiently within the current parametric study.

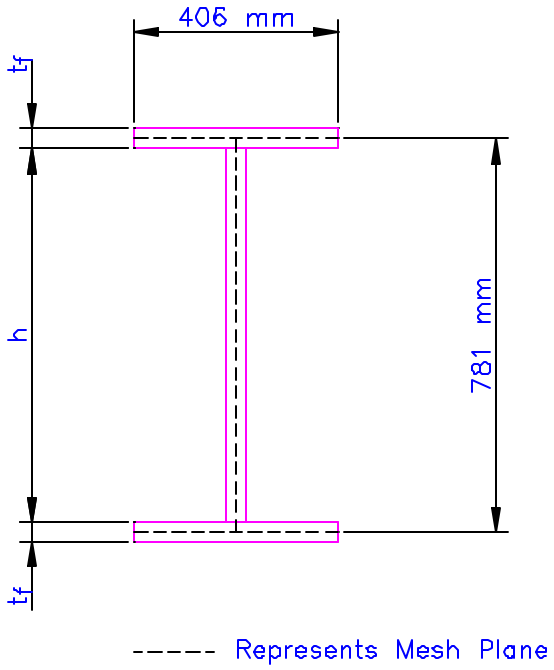

Figure 28 Illustration of Mesh Surface Planes

The elements in the hybrid girder analytical model have an aspect ratio equal to one. That is, all the elements comprising the girder plate components are square shaped with 29mm by 29mm dimensions. This mesh density was proven to provide accurate results, at both the local and global level, in the verification work performed by Earls and Shah (2001). The planes of the mesh surfaces correspond with the middle surfaces of the constituent cross-sectional plate components of the girder as shown in Figure 28. Each cross-sectional plate component is comprised of a node set, which in turn, is used to create an element set (i.e. bottom flange). Thus, a different thickness may be assigned to each cross-sectional plate component. This will be important for the parametric study discussed in Chapter 5.0. Thus, referring to Figure 28, the web height (h) varies slightly with changes in the flange thickness (t_f) since the overall cross sectional depth is held constant.

The equally sized elements in the flange and web allow the two plate components to be compatible, meaning; the web mesh can be integrated with the longitudinal centerline of the flange meshes via an element set. This allows for efficient mesh construction. This is different than the manner in which the stiffeners are connected to the flange and web. In this case, the stiffeners are connected to the flange and web by the use of the ABAQUS multi point constraint (MPC) TIE command. MPC TIE command is used to attach the stiffener edge nodes to the respective nodes located on the flanges and web. Thus, the stiffener nodes "tied" to the corresponding flange and web nodes will have identical global displacements and rotations (as well as any other active degrees of freedom) as the nodes to which they are attached. The MPC TIE command facilitates the

repositioning of the additional stiffeners to create the different bracing configurations discussed in Chapter 5.0.

4.3 Imperfection Seed

In modeling studies where inelastic buckling is investigated, it is important that the evolution of the modeling solution be carefully monitored so that any indication of bifurcation in the equilibrium path is carefully assessed so as to guarantee that the equilibrium branch being followed corresponds to the lowest energy state of the system (Earls and Shah 2001). In order to ensure that the lowest energy path is taken, the current study uses the strategy of seeding the finite element mesh of the beam with an initial displacement field. The initial displacement field is obtained from a linearized-eigenvalue buckling analysis from which an approximation to the first buckling mode of the girder is obtained. The displacement field associated with this lowest mode is then superimposed on the finite element model as a seed imperfection for use in the incremental nonlinear analysis. This seed imperfection displacement is scaled so that the maximum initial displacement anywhere in the mesh is equal to one-one-thousandth of the span length between supports (L/1000) (Yura and Hewig 2001). The imperfection is small enough so as to not affect gross cross sectional properties (Earls and Shah 2001). Although the technique of seeding a finite element mesh with an initial imperfection to help ensure that the correct equilibrium path is followed in the model is recognized to have short comings, the technique is nonetheless employed in the current study due to the

fact that the results obtained from this method have agreed quite well with experimental tests (Earls and Shah 2001). This displacement field is introduced in the model geometry by using the *IMPERFECTION option. The nonlinear load-displacement analysis may then be carried out as explained in Section 3.1.

4.4 Material Property Definitions

Steels of various yield strength are used in the current study. The flanges consist 540.627 MPa (78.4 ksi) HPS steel throughout the investigation while yield strengths of the webs and stiffeners vary from 275.800 MPa (40 ksi) to 413.700 MPa (60 ksi). Web and stiffener yield strengths are composed of equal yield strengths in all models analyzed in the current study. ABAQUS requires that material properties for finite-strain calculations be given in terms of true stress (force per current area) and logarithmic strain as discussed in Section 3.4 of the current study (ABAQUS 1999). The true stress (s_{true}) and logarithmic plastic strain ($e_{\ln}^{pl}$) are expressed in terms of engineering stress and strain, respectively as:

$$s_{true} = s_{eng}(1 + e_{eng}) \tag{4-1}$$

$$e_{\ln}^{pl} = \ln(1 + e_{eng}) - \frac{s_{true}}{E} \tag{4-2}$$

Multiple material definitions are required in one input file since the current study deals with hybrid girders.

The input file must ensure that the material is adequately defined for the purpose of the analysis. The material specifications in the input file must include both elastic and plastic properties. The elastic properties are entered into the input file by specifying the modulus of elasticity (*E*) and poison's ratio (*?*). For the current study, *E* and *?* are equal to 200,000 MPa (29,000 ksi) and 0.3, respectively for all steels. The plastic values are specified as points along the true stress versus true strain plot shown in Figure 24 and given in Appendix 1. The plastic values for the HPS steel used in the flanges of the current model are based on the results of material tests performed on HPS steel used in experimental tests by Azizinamini et al. (1999) at the University of Nebraska. The plastic properties for the web steel used in all the models are a amalgam of values provided by Salmon and Johnson (1996) and the ASCE (1971) guide and commentary on plastic design in steel. ABAQUS uses uniaxial material properties to extrapolate a yield surface in three-dimensional principal stress space.

4.5 Verification Study

As a compliment to verification work performed by Earls and Shah (2001), additional verification work is performed in the current study to further demonstrate the validity of the nonlinear finite element modeling techniques used herein. This current verification work consists of analytically modeling experimental work done at the University of Lehigh on a conventional A36 steel I-shaped beam. Results of the analytical verification model, in comparison to the experimental model, are presented in terms of moment versus rotation plots and failure modes.

4.5.1 Verification Model Geometry

The analytical verification model is a representation of the experimental work performed by Green et al. (2002) on a simply supported doubly symmetric A36 beam subjected to a point load at midspan. This point load produces a moment gradient along the longitudinal axis of the beam. The analytical model is created in accordance with the model dimensions and material values given for Test Specimen 5 by Green et al. (2002). The geometric dimensions of the analytical model are shown in Figure 29. Figure 30 provides the Excel sheet used to generate the cross-sectional properties, plastic moment (M_p), and plastic rotation ($?_p$), based on the as-built geometric dimensions and material properties given by Green et al (2002). The Excel sheet is explained in Appendix D.

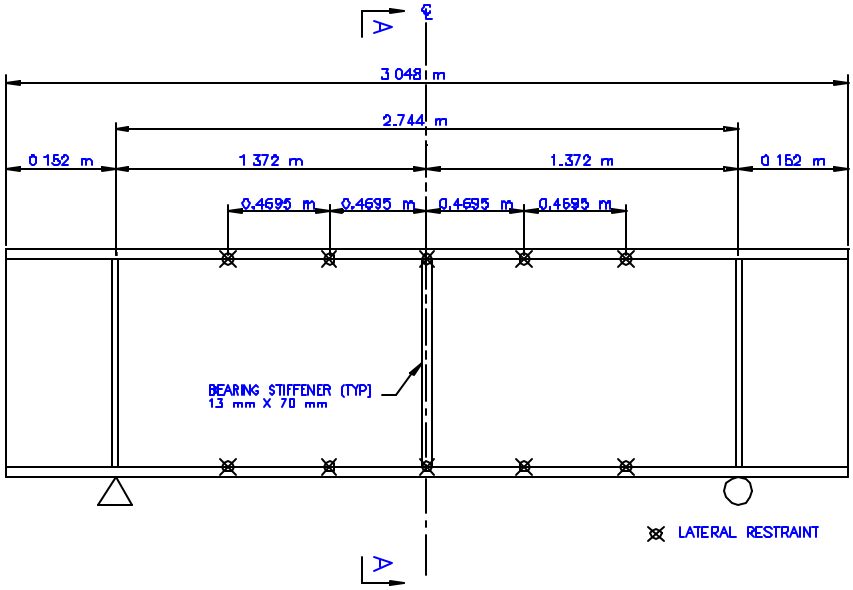

MODEL ELEVATION VIEW
NOT TO SCALE

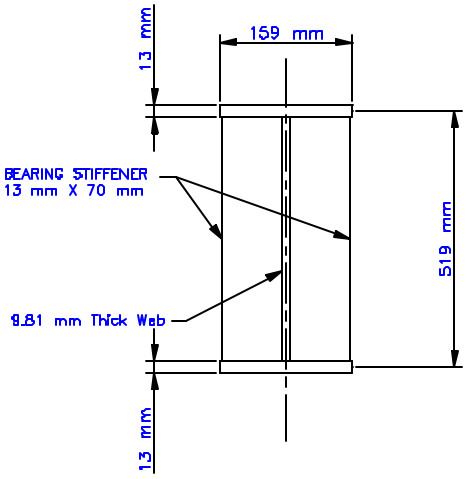

SECTION A–A

Figure 29 Finite Element Verification Model Dimensions

Calculation of Mp and Θp

Enter in the Dimensions of the Beam		
Height =	0.51929	*
Width =	0.1524	
Flange Thickness =	0.01301	
Web Thickness =	0.00981	
L btw Supports =	2.744	
A1 =	0.001983	m^2
A2 =	0.002483	m^2
A3 =	0.002483	m^2
A4 =	0.001983	m^2

Calculations of the Resultant Forces		
R1 =	615168.1	N
R2 =	770479.9	N
R3 =	770479.9	N
R4 =	615168.1	N

Enter Stresses in the 4 beam Sections (ksi)				
$\sigma y1$ =	45	=	310264100	Pa **
$\sigma y2$ =	45	=	310264100	Pa
$\sigma y3$ =	45	=	310264100	Pa
$\sigma y4$ =	45	=	310264100	Pa **

Cross Sectional Properties		
E =	1.99955E+11	Pa
Ixx =	0.000373475	m^4
Iyy =	7.71488E-06	m^4
ry =	0.029389269	
Sx =	0.001403251	
P =	749985.2936	N
Mp =	514489.9114	Nm
Θp =	0.004726144	

* Height is defined from the centroid of the top flange to the centroid of the bottom flange

Figure 30 Calculation Sheet for Verification Model

Figure 27 shows an elevation and cross-sectional view of the model geometry. The verification model has a total length of 3.048m and a depth of 0.52m from the center of the top flange to the center of bottom flange. The flange and web thicknesses are 13mm and 9.81mm, respectively. The flange width is 0.1524m and the web height is 0.506m. This results in a flange slenderness ratio ($b_f/2t_f$) equal to 5.86 and a web slenderness ratio (h/t_w) equal to 51.61 which agree with the values given by Green et al. (2002). The distance (L) between the two supports is 2.744m as shown in Figure 26. The analytical model has an overhang length of 15.2mm (in agreement with the experimental test).

Support and midspan full-depth bearing stiffeners are provided on both sides of the web as 13mm thick and 70mm wide plates. The analytical model is braced against out-of-plane translation by specifying bracing springs on the top and bottom flange at four locations orthogonal to the longitudinal axis of the model. These bracing springs model the flexible lateral bracing provided in the experimental work. The combined spring stiffness at each bracing location on the beam longitudinal axis is taken as six times the required AISC lateral bracing stiffness given in Chapter C of the AISC LRFD (1999). This value is based on recent research focusing on lateral bracing of HPS I-beams in flexure (Thomas and Earls 2002). The AISC required brace strength is given in Chapter C of the AISC Specification (1999) as

$$b_{br} = \frac{10 M_u C_d}{f L_b h_o} \tag{4-3}$$

where f = 0.75, Mu = required flexural strength (in this case M_p) (kN-mm), h_o = distance between flange centroids (mm), C_d = 1.0 for bending in single curvature, L_b = distance between braces (mm). Since the actual spacing of braced points is less than L_{pd}, L_{pd} is used for L_b as recommended by AISC (1999). The location of each lateral spring braces is denoted in Figure 29 by an "x". Figure 31 illustrates the lateral bracing in both the experimental test setup and the analytical verification model. Note that only one half-span of the beam's total length is shown.

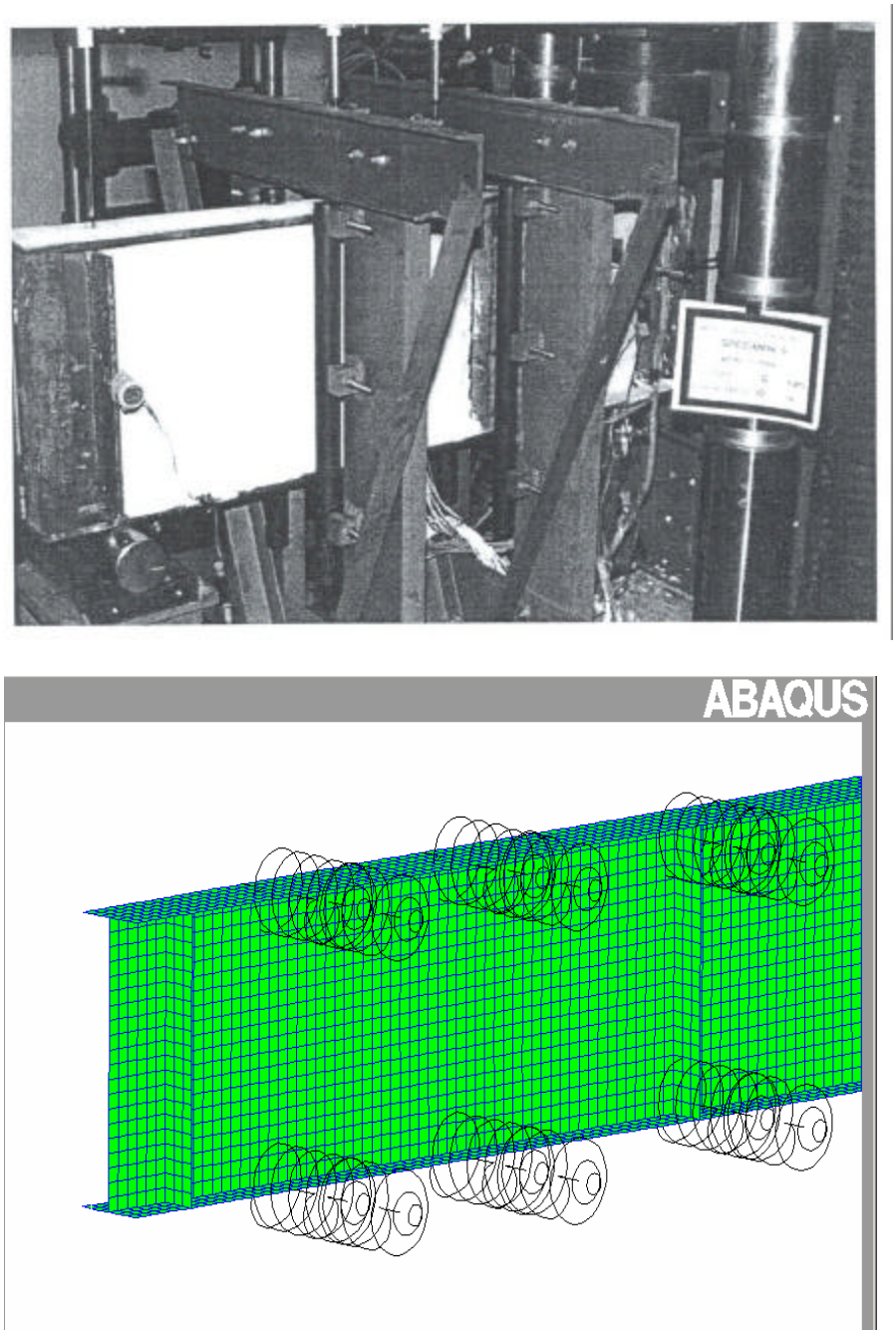

Figure 31 Illustration of Lateral Bracing for Experimental and Analytical Test of Test Specimen 5

4.5.2 Verification Model Mesh

The verification analytical model constructed for this study is built using identical mesh densities as those used for the parametric study reported herein with the ABAQUS S4R elements described in Section 3.5. The elements in the verification model have an aspect ratio equal to approximately one. The planes of the mesh surfaces correspond with the middle surfaces of the constituent cross-sectional plate components of the girder as shown in Figure 26. Similar to the description of the model used in the current parametric study, each cross-sectional plate component is comprised of a node set, which in turn, is used to create an element set (i.e. bottom flange). The flange, web and stiffeners are attached together in the same manner as discussed in Section 4.2. The strategy of seeding the finite element mesh of the beam with an initial displacement field, as discussed in Section 4.3, is also employed in the same manner for this verification model.

4.5.3 Verification Model Material Property Definitions

The material used for the verification analytical model is the conventional steel, A36. The material specifications in the input file must include both elastic and plastic properties. The elastic properties are entered into the input file by specifying the modulus of elasticity (E) and poison's ratio ($?$). For the current verification study, E and $?$ are equal to 200,000 MPa (29,000 ksi) and 0.3, respectively. The plastic values for A36

are specified as points along the true stress versus true strain plot shown in Figure 24 and given in Table 2.

Table 2 Material Properties Used for A36 Steel

	A36 Steel	
	ε_{ln}^{pl}	σ_{true} (MPa)
Yielding	0.000000	310.264
Strain Hardening (ε_y, F_y)	0.009229	319.537
Strain Hardening (ε_{st}, F_{st})	0.055724	482.633
Ultimate (ε_u, F_u)	0.090034	517.107
Rupture (ε_r, F_r)		

4.5.4 Verification Analysis Results

The rotation capacity (R) reported in the experimental results of Test Specimen 5 was 9.69 (Green et al. 2002). The current study's finite element verification model of Test Specimen 5 achieved a rotation capacity of 9.6. The experimental and finite element verification moment versus rotation plots of Test Specimen 5 are provided in Figures 32 and 33, respectively. As can be seen from Figures 32 and 33, the experimental test of Test Specimen 5 and the analytical verification modeling results of Test Specimen 5 are in close agreement. Failure mode comparisons between the experimental test and the analytical verification model are presented in Figures 34 and 35.

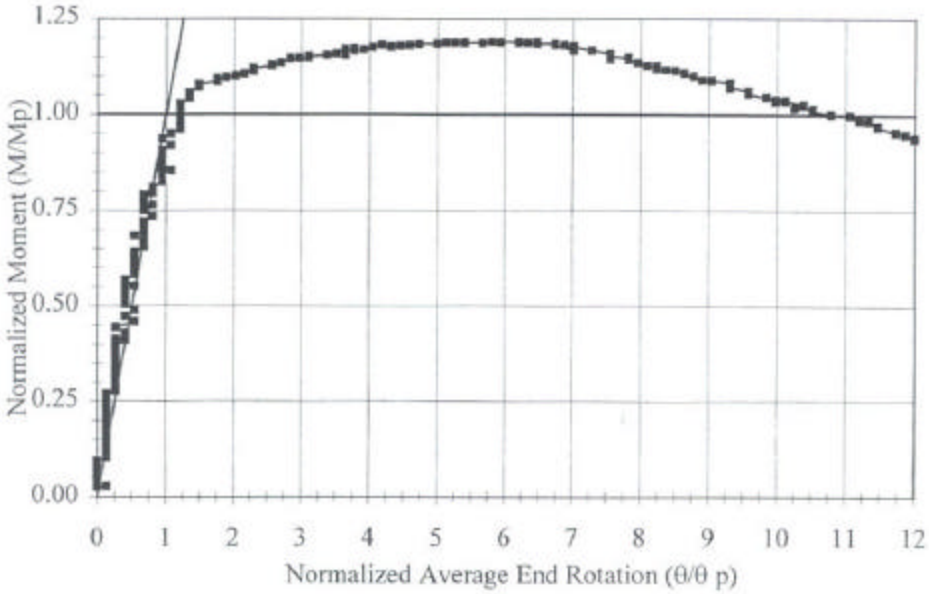

Figure 32 Test Specimen 5 Experimental Moment Gradient Response (Green et al. 2002)

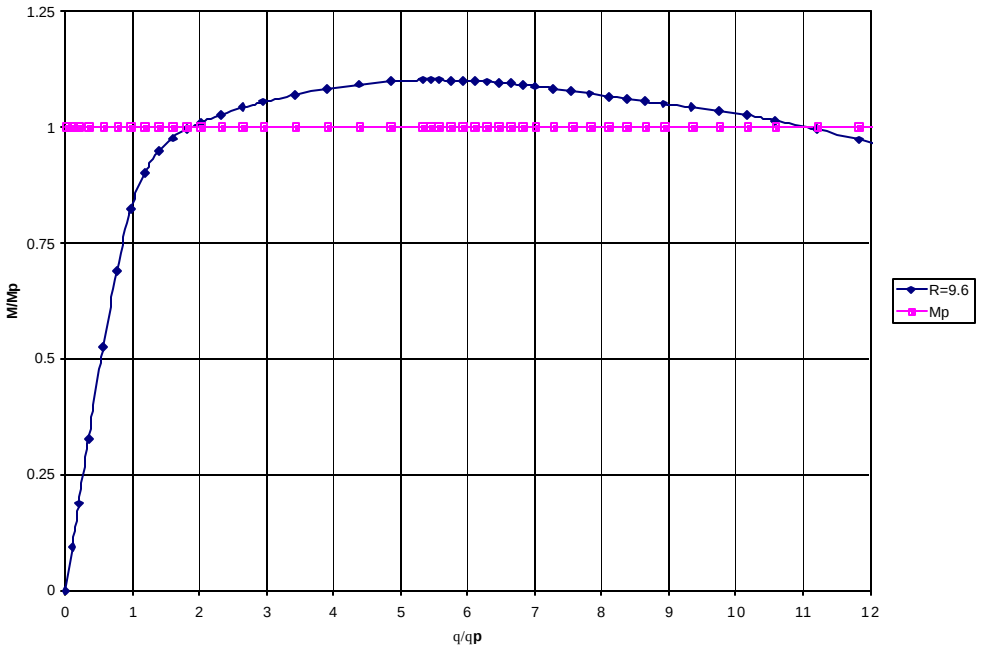

Figure 33 Test Specimen 5 Analytical Verification Model Moment Gradient Response

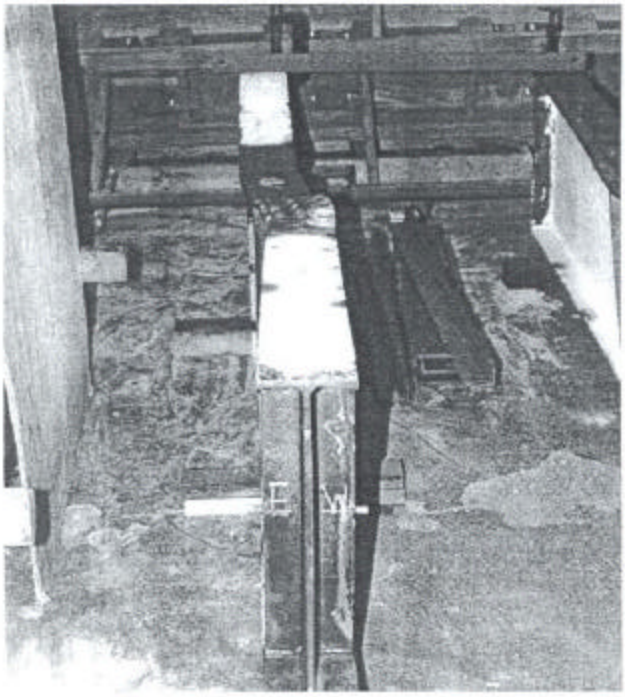

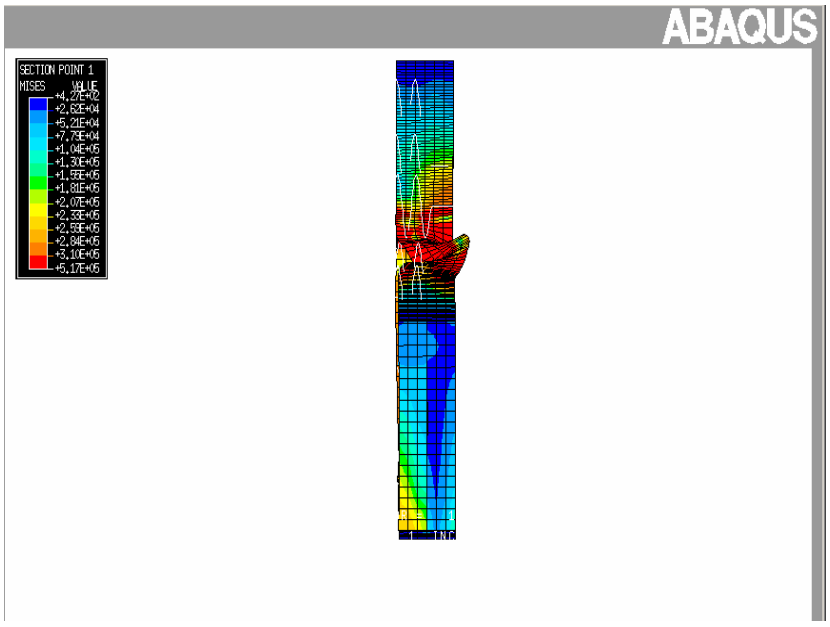

Figure 34 Longitudinal View Showing Lateral Compression Flange Movement in Midspan Region

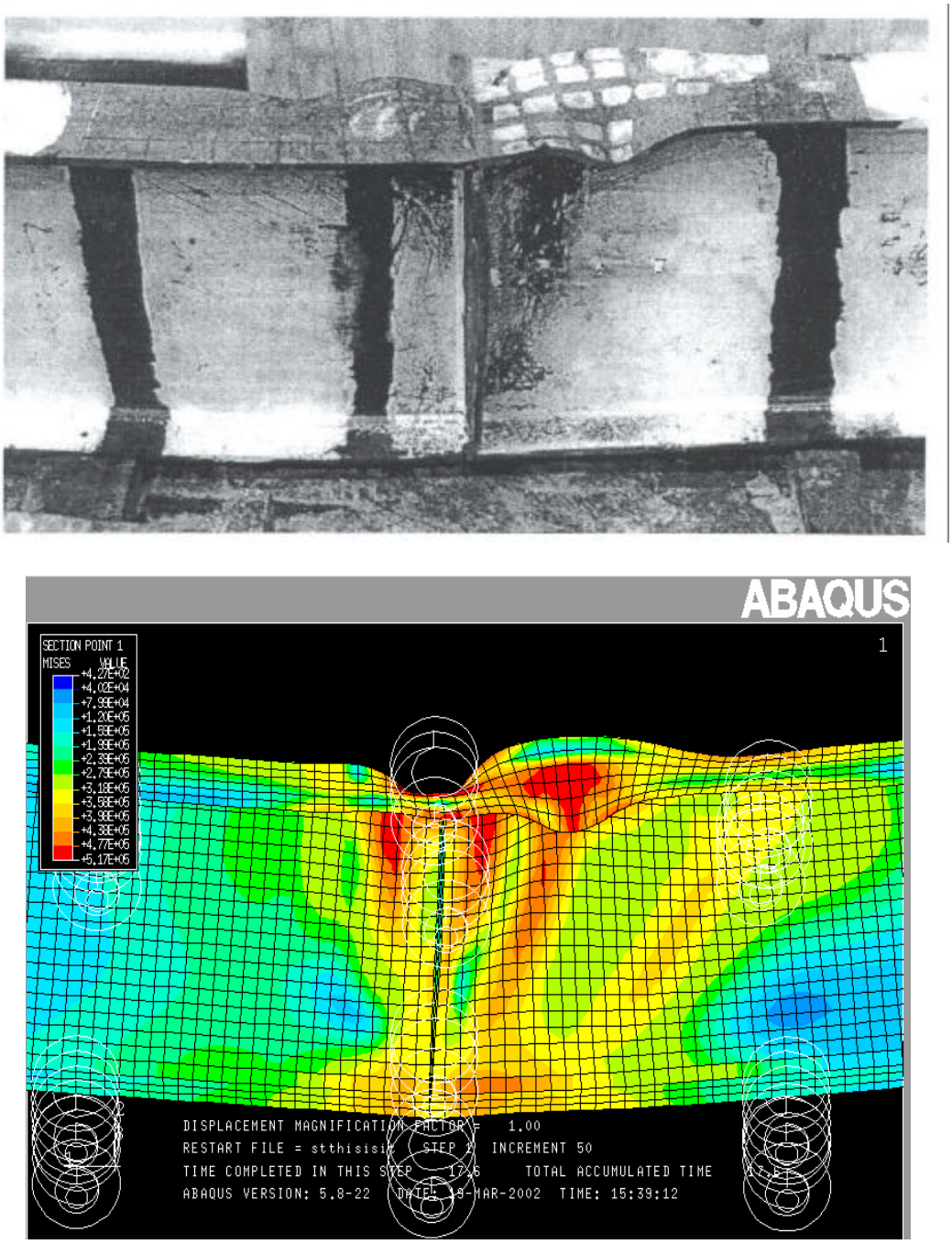

Figure 35 View of Midspan Region Showing Compression Flange Local Buckling

5.0 PARAMETRIC STUDY AND RESULTS

The analytical model described in Chapter 4.0 is used to carry out the current parametric study. The goal of the parametric study is to investigate the influence of HPS flanges on the flexural ductility of hybrid girders, as quantified by rotation capacity. This investigation arises from new research (Earls 1999, 2000a, 2000b, 2001) which is proving that the current American steel building and bridge design specifications' (AISC 1999, AASHTO 1998) independent treatment of local and global inelastic stability phenomenon is difficult to apply to the design of homogeneous HPS I-shapes in flexural.

The hybrid HPS girder is put into a state of flexure by subjecting the analytical model to a moment gradient which varies linearly along its longitudinal axis. The moment gradient is caused by applying a concentrated point load at the midspan of the simply supported configuration as shown in Figure 26.

The parametric study consists of investigating the influence of the HPS flange slenderness ratio on I-shaped hybrid member flexural ductility. This is done for three different flange and web steel combinations and in turn, three different bracing configurations. The flange slenderness influence in conjunction with the three bracing configurations will help shed light on the relationship between local and global inelastic stability phenomenon for hybrid HPS bridge girders. This will be quantified in terms of rotation capacity and observed failure modes. Similar studies will also be carried out on homogenous I-shaped girders in order to gauge the hybrid girder results.

5.1 Parametric Study

Three combinations of web and flange steel are analyzed in the hybrid HPS girder parametric study. Each combination consists of HPS flanges, F_y = 540.6 MPa (78.4 ksi) while the webs are constructed from three types of conventional steel yield strengths: (1) 413.7 MPa (60 ksi); (2) 344.8 MPa (50 ksi); (3) 275.8 MPa (40 ksi). From the three combinations of HPS flanges and conventional steel webs, hybrid HPS girder flexural behavior, as quantified by rotation capacity, is analyzed in terms of HPS flange slenderness for three bracing configurations.

5.1.1 HPS Flange Slenderness Ratio

When a beam's compression flange is adequately braced against lateral-torsional buckling, local buckling of the flange and/or web will govern the attainment of the beam's ultimate capacity, and rotation capacities of three or greater. In order to prevent local buckling of the cross-sectional plate components, current design provisions require that the flange and web be compact. The efficiency of an I-shaped cross-section in flexure is dependent primarily on the behavior of the compression flange as discussed in Chapter 2.

With this in mind, different HPS flange slenderness ratios are analyzed under three unbraced lengths (L_b). This is done for each of the three flange and web steel combinations discussed in Section 5.1.1. The conventional steel web is proportioned so

as to be compact and its plate slenderness (h/t_w) is held constant throughout the entire study. Bracing configurations will be discussed in Section 5.1.3.

From (2-7), the HPS compression flange (F_y = 540.627 MPa) has a limiting slenderness ratio (b/t) of 7.341, where b is half the full flange width (b_f). Five flange slenderness ratios are analyzed for the current study: (1) 5.0; (2) 4.5; (3) 4.0; (4) 3.5; (5) 3.0. The variation of this parameter is achieved by specifying a different flange thickness (t_f) for each ratio in the analytical model while holding the flange width (b_f) constant across all tests. Specific geometric dimensions for each flange slenderness ratio are given in Appendix B.

From (2-9) and (2-10), the web has a limiting slenderness ratio of 72.3 for a hybrid girder using high performance steel in the flanges. The web is held at a constant slenderness ratio (h/t_w) of approximately 45 throughout the entire study and is classified as compact for each of the conventional steels used according to (2-9) and (2-10). This parameter is held constant in order to isolate the effect HPS flange slenderness has on hybrid HPS girder flexural behavior. It must be noted that the web slenderness ratio deviates slightly from 45 for each of the five flange slenderness ratios. The web height is a function of the flange thickness due to reasons discussed in Section 4.2 of the current study. The web thickness is a constant value of 16mm throughout the entire study. Referring to Figure 28, the web height (h) may be expressed in terms of the flange thickness (t_f) as

$$h = 0.781m - t_f \tag{5-1}$$

The web height values for each flange slenderness ratio and the resulting web slenderness ratios are summarized in Table 3. It can be seen in Table 3 that the web slenderness ratio is roughly 45.

Table 3 Web Slenderness As a Function of Flange Slenderness

$b_f/2t_f$	Flange Thickness (m)	Web Height (m)	h/t_w
5.0	0.0406	0.7404	46.275
4.5	0.0450	0.7360	46.000
4.0	0.0508	0.7303	45.640
3.5	0.0580	0.7230	45.188
3.0	0.0677	0.7133	44.581

The influence of HPS flanges on hybrid girder flexural ductility will be observed through the variation of the flange slenderness parameter and constant web slenderness. The hybrid girder constituent cross-sectional plate components are proportioned so as to be compact for the entire study. In conjunction with adequate bracing, the cross-sectional compactness should allow the section to achieve M_p, and maintain this capacity through some rotation capacity. This notion will be investigated by analyzing the five cases of cross-sectional compactness with three unbraced lengths. These unbraced lengths are within the limiting unbraced length that allows the girder to achieve adequate rotation capacity as discussed in Chapter 2.

5.1.2 Bracing Configurations

The five flange slenderness ratios are analyzed for the three combinations of web and flange steel hybrid girders. Each of these hybrid girder configurations are evaluated at three different unbraced lengths. The unbraced length (L_b) is shown in Figure 26. For compact sections, the achievement of the girder's plastic capacity, M_p, depends on the laterally unbraced length. An appropriate L_b will prevent lateral torsional buckling from occurring prior to the attainment of the girder's plastic moment. Furthermore, the unbraced length will govern the type of failure mode the girder will experience. The additional 12mm thick and 200mm wide stiffeners are positioned along the longitudinal axis of the model to achieve the desired unbraced length. The three unbraced lengths considered in the current study are: (1) L_b according to AASHTO Specifications (Section 6.10.4.1.7); (2) L_b equal to one-half the total depth of the girder ($d/2$); (3) L_b equal to the total depth of the girder (d). The AASHTO specification is investigated in order to evaluate the independent treatment of local and global inelastic stability phenomenon by current design provisions. Alternative bracing configurations are analyzed based on the research findings of Earls (1999, 2000a, 2000b, 2001).

The first bracing configuration is based on Section 6.10.4.1.7 of the current American steel bridge design specification (AASHTO 1998). The unbraced length for compact cross-sections is calculated from Equation 6.10.4.1.7-1 of the AASHTO specification, expressed as

$$L_b \le \left[0.124 - 0.0759\left(\frac{M_1}{M_P}\right)\right]\left[\frac{r_y E}{F_{yc}}\right] \tag{5-2}$$

where: L_b = the unbraced length (mm, in); r_y = minimum radius of gyration of the steel section, with respect to the vertical axis (mm, in); M_1 = the smaller moment due to the factored loading at either end of the unbraced length (MPa, ksi); M_p = plastic moment (MPa, ksi); F_{yc} = specified minimum yield strength of the compression flange (MPa, ksi). This equation is applicable to both homogeneous and hybrid girders.

The AASHTO unbraced length (L_b) that is used for each of the flange slenderness ratios considered in the current study is determined from (5-2). The unbraced length will vary slightly for the five flange slenderness ratios due to the varying r_y. All other variables in (5-2) remain constant throughout the entire study: E = 200,000 MPa; F_{yc} = 540.6 MPa. The term M_1/M_p cancels out of the equation because the moment is equal to zero at the end of the unbraced length (either support location) due to the moment gradient. As a result, the AASHTO unbraced length used for each analytical model may be expressed as

$$L_b = 45.87 r_y \tag{5-3}$$

Values for the AASHTO bracing lengths for the varying flange slenderness ratios are given in Appendix B.

The alternative bracing schemes investigated in the current study are based on the research carried out by Earls (1999, 2000a, 2000b, 2001) on homogeneous HPS girders. This research is discussed in detail in Section 1.1 of the current study. It was found by Earls (1999) that the less favorable mode 2 inelastic buckling manifestations occurred at distance roughly equal to *d/2* from either side of the midspan-bearing stiffener. Earls (1999) found that imposing out-of-plane bracing at these locations had a significant impact on the flexural ductility of HPS homogenous girders Hence, braces are positioned at distances of *d/2* on either side of the midspan stiffener in the current study to investigate the impact this may have on compact hybrid HPS girders. In addition to this bracing scheme, a third configuration is investigated which consists of situating stiffeners a distance of *d* on either side of the midspan stiffener. This last bracing configuration is based on results from a study carried out by Earls and Thomas (2002).

Thus, the hybrid girder parametric study consists of varying HPS flange slenderness ratios in conjunction with three bracing configurations for three combinations of flange and web steel. The relationship between local and global inelastic stability phenomenon for hybrid HPS girders are subsequently studied as these parameters are varied. Hybrid HPS girder flexural ductility will be quantified in terms of rotation capacity.

5.2 Additional Parametric Studies

Additional finite element parametric studies are carried out on homogeneous girders. The hybrid analytical model is transformed into a homogeneous analytical model by simply defining equal strength flange and web steel in the model input file. This has no effect on the analytical model geometry. The steel yield strength (F_y) for the homogeneous model is 344.8 MPa (50 ksi). This yield strength is chosen so as to model the flexural behavior of a conventional steel girder. The independent treatment of local and global inelastic stability in order to achieve sufficient flexural ductility has been proven to be valid with conventional steel. This notion is investigated within the context of a homogeneous analytical model (F_y = 344.8 MPa) by performing a similar parametric study to the set outlined in Section 5.1. In addition to the homogeneous girder of F_y = 344.8, one case of AASHTO bracing with, flange slenderness ratio of 4.0, and homogenous steel of F_y = 275.8 MPa (40 ksi) is analyzed.

The last parametric study deals with AASHTO interaction equation, (2-12) discussed in Chapter 2 of the current study. According to AASHTO Specification, This interaction equation must be considered when the girder web slenderness and/or flange slenderness is greater than 75 percent of their respective limit Two cases are analyzed in this study: (1) the web slenderness is equal to the limit given by (2-11) with 75 percent of the flange slenderness limit given by (2-7); (2) the flange slenderness is equal to its limit given by (2-7) 75 percent of the resulting web slenderness given by (2-11). These two cases are considered for each combination of flange and web steel discussed in

Section 5.1. The girder cross-sectional geometries of the two interaction cases are given in Appendix B. The unbraced lengths are calculated according to (5-3). Using this distance, stiffeners are positioned on either side of the midspan-bearing stiffener along the longitudinal axis of the girder. All other stiffener locations remain at the positions specified in Figure 26 and discussed in Section 4.1.

5.3 Results

This section discusses the results obtained from the parametric studies described in Sections 5.1 and 5.2. The results are categorized in terms of the three bracing configurations described in Section 5.1.2 of the current study. The main objective of the current study is to investigate the influence of HPS steel flanges on the flexural behavior of hybrid steel girders in the context of the current design specification provisions presented in Chapter 2.0. Thus, the hybrid girder's achievement of a rotation capacity equal to three or greater and its resulting failure modes will now be carefully considered.

A table indicating the general flexural behavior of each bracing configuration is provided at the end of each result section. The occurrence of a specific buckling failure mode, and the attainment of a rotation capacity of three or greater are indicated by a check mark for each flange slenderness ratio in all hybrid steel girder combinations. In addition, the maximum and minimum rotation capacities are indicated by a check mark for each hybrid steel girder combination in the respective flange slenderness ratio row. The buckling failure modes that are recorded are local buckling (web and/or flange),

lateral torsional buckling, vertical flange buckling, and interactive local and lateral torsional buckling. The reporting of these buckling failure modes employs a three check mark system in which minimal, moderate, and extreme degrees of buckling are represented by one, two, and three check marks, respectively. "Interactive local and lateral torsional buckling" refers to local and lateral torsional buckling being highly coupled at a specific location within the girder model. Illustrations of the three degrees of buckling for each buckling failure mode are shown in Figures 36 through 47.

Moment versus rotation plots for all models analyzed in the current study are given in Appendix C (Figures C1 through C15). Each model's rotation capacity, calculated from their respective moment versus rotation plot, is also given in Appendix C (Tables C1 through C4). Appendix D includes calculation sheets (Figures D2 through D34) used to calculate cross-sectional properties needed to generate the moment versus rotation plots and spreadsheets used to calculate the rotation capacity based on the respective moment versus rotation plot (Figures D37 through D40).

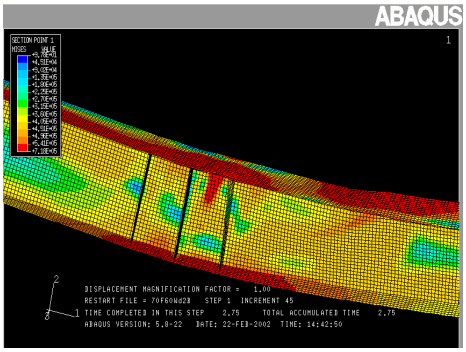

Figure 36 Minimal Local Buckling

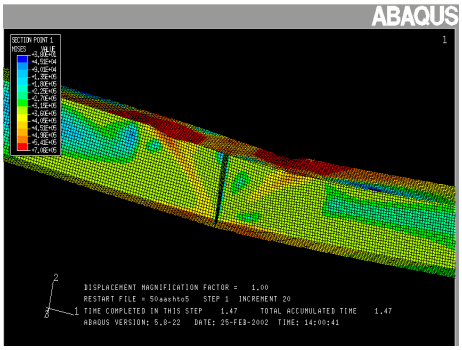

Figure 37 Moderate Local Buckling

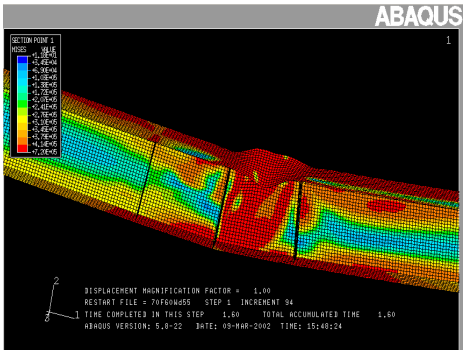

Figure 38 Extreme Local Buckling

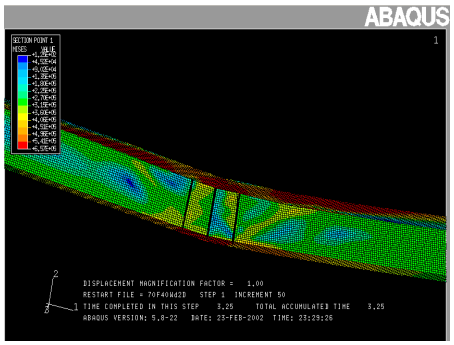

Figure 39 Minimal Lateral Torsional Buckling

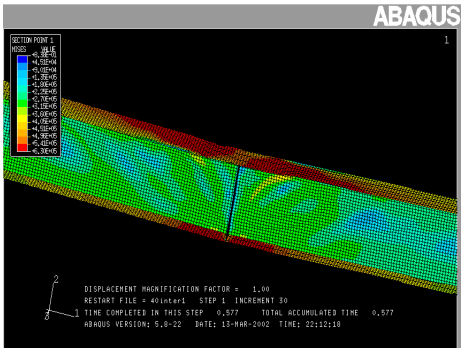

Figure 40 Moderate Lateral Torsional Buckling

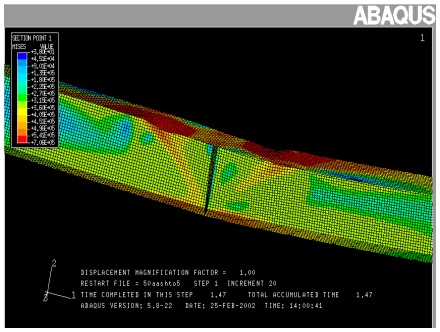

Figure 41 Extreme Lateral Torsional Buckling

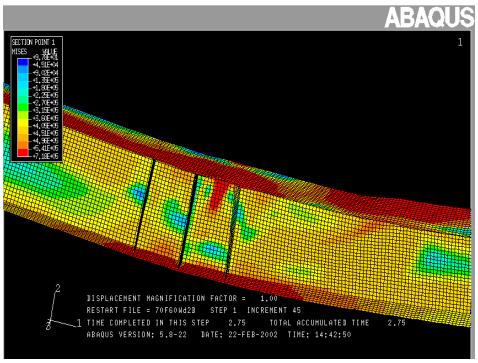

Figure 42 Minimal Vertical Flange Buckling

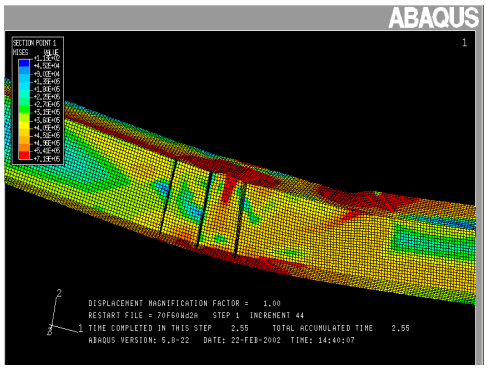

Figure 43 Moderate Vertical Flange Buckling

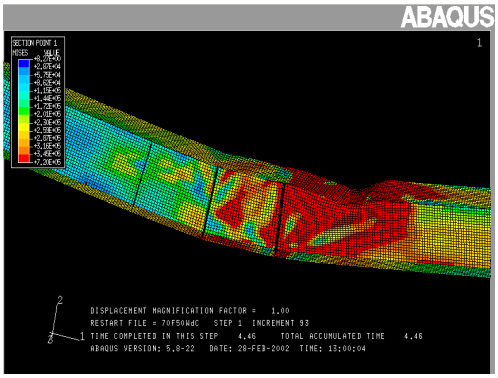

Figure 44 Extreme Vertical Flange Buckling

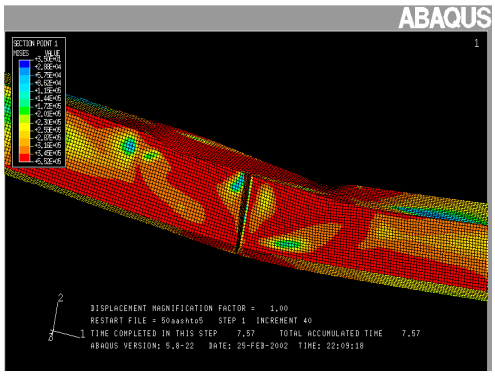

Figure 45 Minimal Interactive Local and Global Buckling

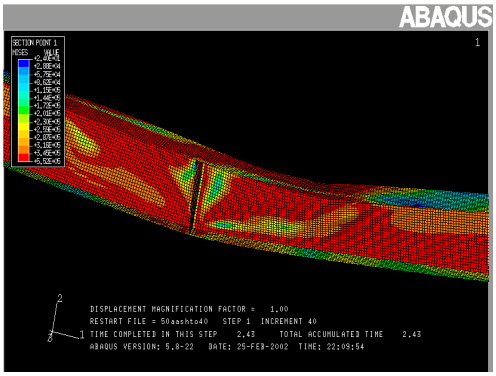

Figure 46 Moderate Interactive Local and Global Buckling

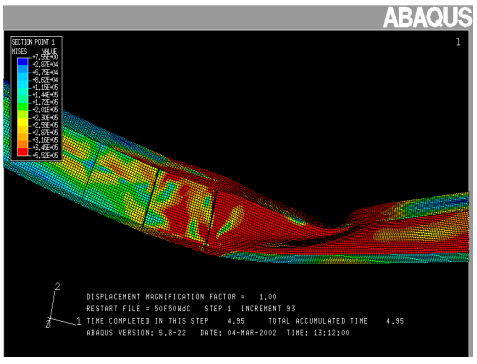

Figure 47 Extreme Interactive Local and Global Buckling

5.3.1 AASHTO Bracing Results

As can be seen in Table 4 and Table C1, all hybrid HPS girders braced according to AASHTO Specification (Section 6.10.4.1.7), were not able to attain the desired rotation capacity (*R*) of three as needed for moment redistribution. For each flange and web steel combination, these hybrid HPS girders were able to reach their plastic moment but with very little rotation capacity, as can be seen from Figures C1 through C3. All moment versus rotation plots for AASHTO bracing (Figures C1 – C4) are characteristic of Mode 2 moment-rotation plots described by Earls (1999). The attainment of the peak moment in the AASHTO bracing moment versus rotation plots is followed by a gradual and constant decrease in nominal moment capacity as beam cross-sectional rotation increases. The largest rotation capacities for all hybrid HPS girders occurred at the largest flange slenderness ratio considered for this bracing configuration, 5.0. As the flange slenderness decreased to 3.0, so did the rotation capacity of all hybrid HPS girders. This is contrary to the general belief that rotation capacity increases with a decrease in flange slenderness ratio. It is interesting to note that the homogeneous 344.8 MPa (50 ksi) girder with AASHTO bracing did not achieve a rotation capacity with five flange slenderness ratios considered. However, the rotation capacities achieved by the homogeneous girders are much greater than those of the hybrid girders. A maximum rotation capacity was achieved by the homogeneous girder with a flange slenderness ratio equal to 4.0. As the flange slenderness ratio either increased or decreased from 4.0, the rotation capacity of the homogeneous girder decreased.

5.3.1.1 Detailed description of model behavior with AASHTO bracing. The hybrid HPS girder with a 413.7 MPa (60 ksi) web experienced severe flange local buckling with flange slenderness ratios of 5.0, 4.5, and 4.0. The local buckling was symmetric about the midspan stiffener and the longitudinal axis of the beam for all three of the flange slenderness ratios. This severe local buckling was accompanied by some moderate vertical flange buckling occurring near the midspan stiffener in only one-half span of the beam. This failure mode is illustrated in Figure 48. As the flange slenderness ratio decreased to 3.0, the beam experienced a decrease in local buckling severity and an increase in the vertical flange buckling severity as seen in Figure 49. There was slight interactive local and lateral torsional buckling for all flange slenderness ratios of the hybrid HPS girder with a 413.7 MPa (60 ksi) web.

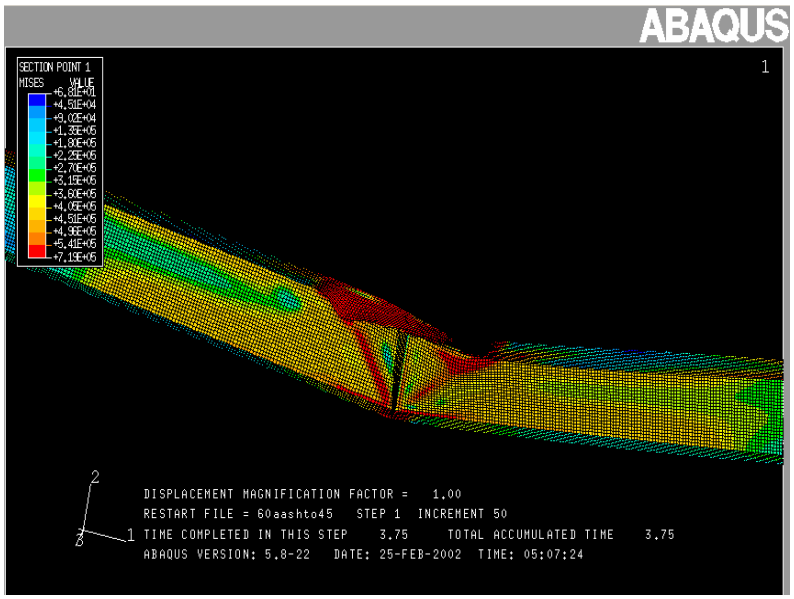

Figure 48 Illustration of Failure Mode for Hybrid HPS Girder with a 413.7 MPa (60 ksi) web; bf/2tf = 5.0

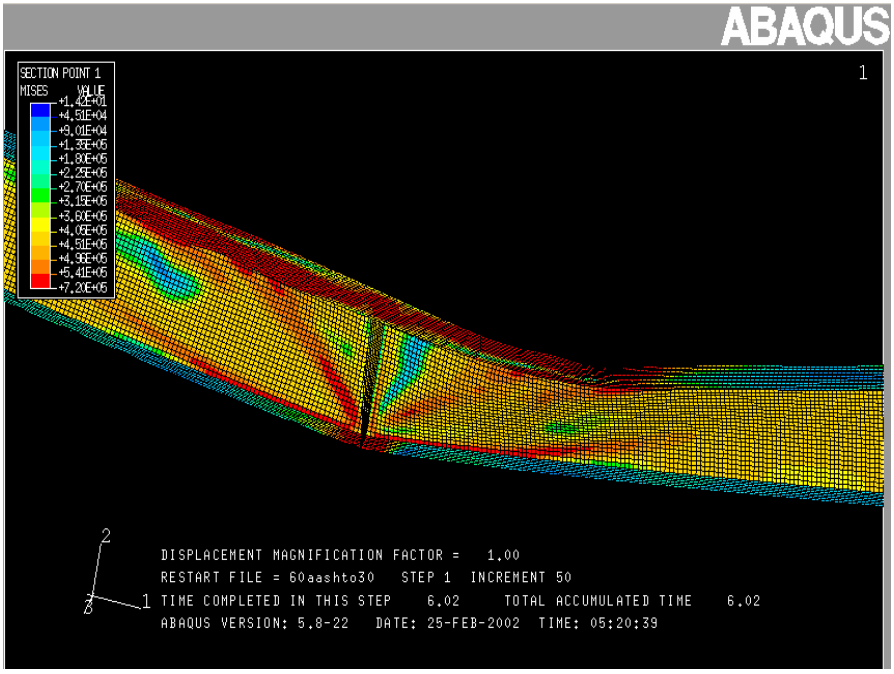

Figure 49 Illustration of Failure Mode for Hybrid HPS Girder with a 413.7 MPa (60 ksi) web; bf/2tf = 3.0

The hybrid HPS girder with a 344.8 MPa (50 ksi) web experienced similar, but less severe failure modes than the hybrid HPS girder with a 413.7 MPa (60 ksi) web. Symmetric local buckling about the midspan stiffener and the longitudinal axis, as well as lateral torsional buckling, was experienced in conjunction with all flange slenderness ratios. The most pronounced failure modes for this flange and web steel combination occurred at flange slenderness ratios of 5.0 and 3.0 shown in Figure 50. Similar rotation capacities to the hybrid HPS girder with a 413.7 MPa (60 ksi) web were attained.

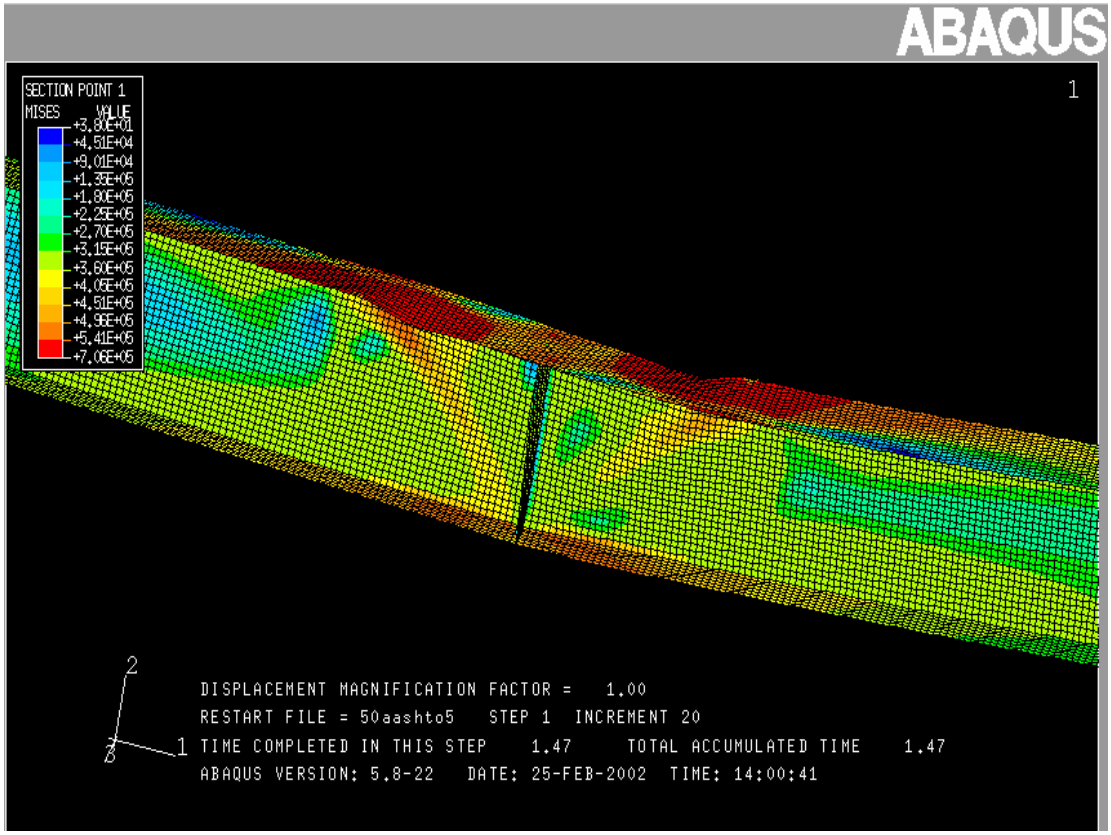

Figure 50 Illustration of Failure Mode for Hybrid HPS Girder with a 344.8 MPa (50 ksi) web; bf/2tf = 5.0 and 3.0

The hybrid HPS girder with a 275.8 MPa (40 ksi) web experienced the least severe failure modes of all three flange and web steel combinations for AASHTO bracing. However, as seen from Table C1, this hybrid HPS girder also attained the smallest rotation capacities of all three flange and web steel combinations. Each flange slenderness ratio analyzed experienced minimal local and lateral torsional buckling. The flange slenderness ratio of 3.0 experienced slight local and lateral torsional buckling interaction occurring near the midspan stiffener in only one-half span of the beam.

The homogeneous 344.8 MPa (50 ksi) girder experienced flange local buckling about the midspan stiffener for each flange slenderness ratio. The local buckling was most severe for the flange slenderness ratio of 5.0. As the flange slenderness ratio decreased, interactive local and lateral torsional buckling increased. This failure mode occurred near the midspan stiffener in only one-half span of the beam. The interactive local and lateral torsional buckling was most severe for the flange slenderness ratio of 3.0, which resulted in a rotation capacity of 2.4 that is much smaller than the other flange slenderness ratio's rotation capacity (Table C1). This is illustrated in Figure 51. It is interesting to note that this failure mode is very similar to the failure mode experienced by the hybrid HPS Girder with a 413.7 MPa (60 ksi) web and a flange slenderness ratio of 3.0. However, the hybrid HPS girder exhibits a much lower rotation capacity.

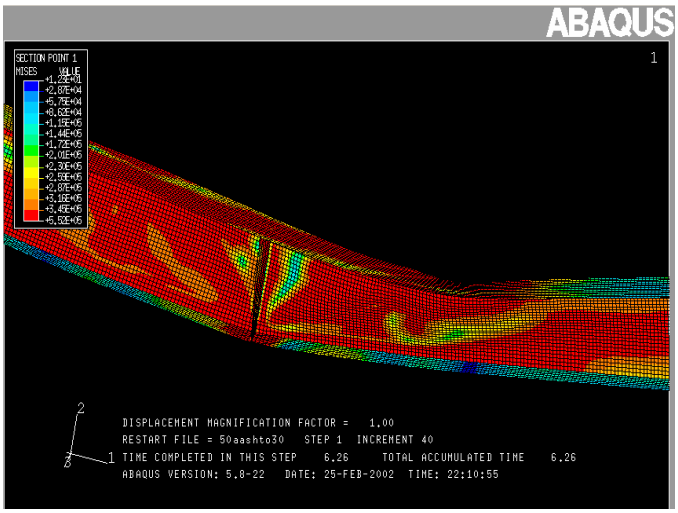

Figure 51 Illustration of Failure Mode for Homogeneous 344.8 MPa (50 ksi) Girder; bf/2tf = 3.0

All flange and web steel combinations at the AASHTO bracing limit demonstrate severe failure modes in the extreme flange slenderness ratios analyzed in the current study, 5.0 and 3.0. The more slender flange ($b_f/2t_f$ = 5.0) is dominated by flange local buckling. The more stocky flange ($b_f/2t_f$ = 3.0) fails by either vertical flange buckling in the hybrid HPS girder with 413.7 MPa (60 ksi) case or global buckling in all other flange and web steel combinations. For the hybrid HPS girders, the failure modes tend to be less severe as the web yield strength decreases. However, the rotation capacities are smaller as the web yield strength decreases as well.

Table 4 General Flexural Behavior of Girders with AASHTO Bracing

HPS Hybrid Girder w/ 413.7 MPa (60 ksi), AASHTO Bracing

$b_f/2t_f$	Local Buckling (*)	Lateral Torsional Buckling	Vertical Flange Buckling	Interactive Local Buckling & LTB (**)	R = 3	Minimum R	Maximum R
5.0	✔ ✔ ✔		✔	✔			✔
4.5	✔ ✔ ✔		✔	✔			
4.0	✔ ✔ ✔		✔	✔			
3.5	✔ ✔		✔ ✔	✔			
3.0	✔		✔ ✔	✔		✔	

HPS Hybrid Girder w/ 344.75 MPa (50 ksi), AASHTO Bracing

$b_f/2t_f$	Local Buckling (*)	Lateral Torsional Buckling	Vertical Flange Buckling	Interactive Local Buckling & LTB (**)	R = 3	Minimum R	Maximum R
5.0	✔ ✔	✔ ✔					✔
4.5	✔ ✔	✔	✔				
4.0	✔	✔					
3.5	✔	✔					
3.0	✔ ✔	✔ ✔				✔	

HPS Hybrid Girder w/ 275.8 MPa (40 ksi), AASHTO Bracing

$b_f/2t_f$	Local Buckling (*)	Lateral Torsional Buckling	Vertical Flange Buckling	Interactive Local Buckling & LTB (**)	R = 3	Minimum R	Maximum R
5.0	✔ ✔	✔					✔
4.5	✔	✔					
4.0	✔	✔					
3.5		✔					
3.0	✔	✔ ✔		✔		✔	

Homogeneous 344.75 MPa (50 ksi) Girder, AASHTO Bracing

$b_f/2t_f$	Local Buckling (*)	Lateral Torsional Buckling	Vertical Flange Buckling	Interactive Local Buckling & LTB (**)	R = 3	Minimum R	Maximum R
5.0	✔ ✔	✔		✔			
4.5	✔	✔		✔			
4.0	✔			✔ ✔			✔
3.5	✔			✔ ✔			
3.0	✔			✔ ✔ ✔		✔	

* Refers to isolated local buckling of the flange

** Refers to local and lateral torsional buckling occuring at a specific region along the longitudinal axis

5.3.2 *d/2* Bracing Results

As can be seen in Table 5 and Table C2, most of the hybrid HPS girders braced with an unbraced length (L_b) equal to half the depth of the girder (*d/2*), were able to attain the desired rotation capacity (R) of three as needed for moment redistribution. All moment versus rotation plots for *d/2* bracing (Figures C5 – C8) are characteristic of Mode 1 moment-rotation response as described by Earls (1999). The *d/2* moment versus rotation plots exhibit a fairly constant inelastic plateau corresponding to the ultimate moment capacity. This constant moment plateau is followed by a well-defined "knee" region where the nominal moment capacity diminishes quickly. The maximum rotation capacity for all girders (both hybrid and homogeneous) with unbraced lengths of *d/2* occurred with a flange slenderness equal to 4.5 or 4.0. As the flange slenderness ratio either increased or decreased from these optimal flange slenderness values, the rotation capacity of the girder decreased. The maximum rotation capacity, for each flange and web steel combination, increased as the web yield strength decreased. The minimum rotation capacity achieved for all *d/2* bracing flange and web steel combinations was with the smallest flange slenderness ratio analyzed, 3.0 (again, it is pointed out that vertical flange buckling was responsible for this). The homogeneous 344.8 MPa (50 ksi) girders achieved almost twice the rotation capacities than the hybrid HPS girders with equal flange slenderness ratios and braced at *d/2*.

5.3.2.1 Detailed description of model behavior with *d/2* bracing. The HPS hybrid steel girder with a 413.7 MPa (60 ksi) web experienced slight interactive and local buckling for each flange slenderness ratio. Local buckling of the flange occured between the midspan bearing stiffener and an adjacent intermediate stiffener for a flange slenderness of 5.0, as seen in Figure 52. This flange local buckling mode also occurs in the other girders failures but it becomes less pronounced as the flange slenderness ratios decrease. Moderate vertical buckling of the flange occurs in the same half span of the girder as the local buckling for flange slenderness ratios of 5.0 and 3.0 also seen in Figure 52.

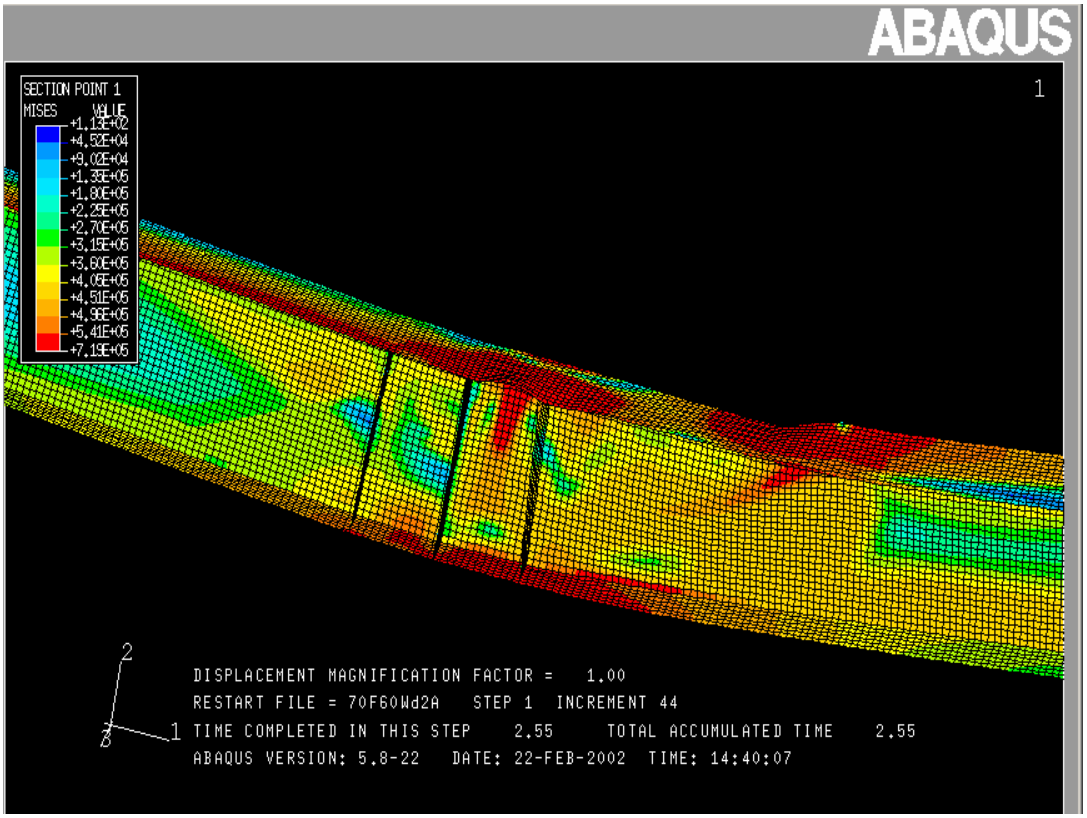

Figure 52 Illustration of Failure Mode for Hybrid HPS Girder with a 413.7 MPa (60 ksi) web; bf/2tf = 5.0

The hybrid HPS girder with a 344.8 MPa (50 ksi) web experiences flange local buckling in the same location as the hybrid HPS girder with 413.7 MPa web. This flange local buckling occurred for all flange slenderness ratios except 3.0. For the flange slenderness ratios of 5.0 and 4.5, vertical flange buckling occurred in the same half span of the girder as the flange local buckling, similar to the hybrid HPS girder with a 413.7 MPa (60 ksi) web. The hybrid HPS girder with a flange slenderness ratio of 3.0 experienced severe vertical flange buckling, as can be seen in Figure 53. This severe vertical flange buckling occurred in the same location as the vertical flange buckling of the hybrid HPS girders of 5.0 and 4.5. As a result of this severe vertical flange buckling, the girder's rotation capacity is smaller than the other girders.

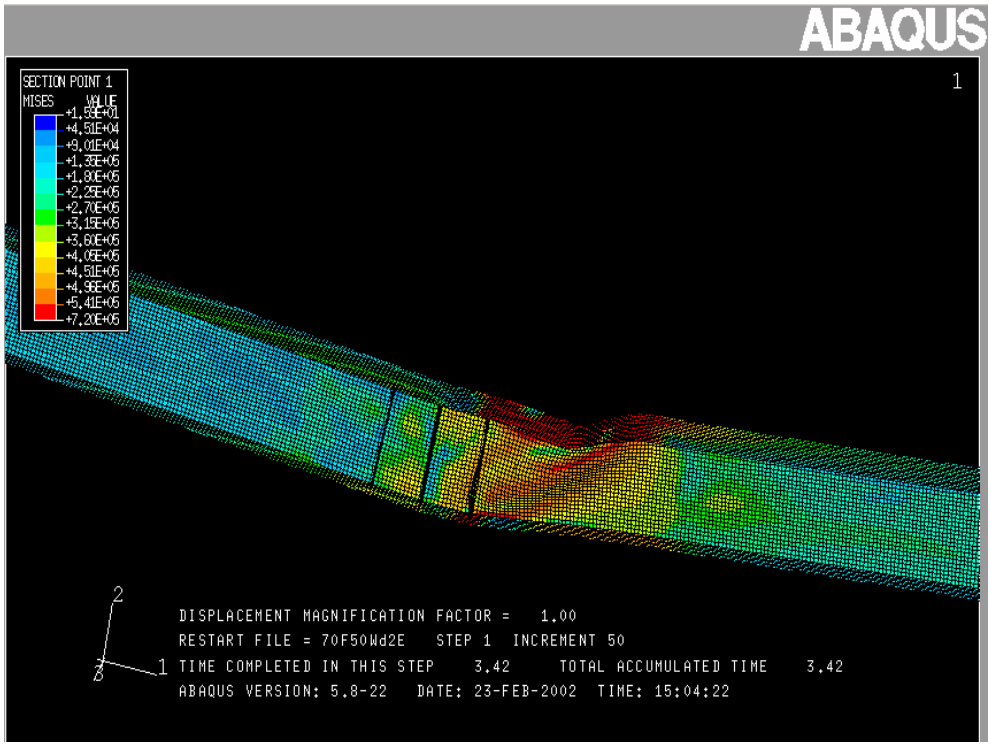

Figure 53 Illustration of Failure Mode for Hybrid HPS Girder with a 344.8 MPa (50 ksi) web; bf/2tf = 3.0

The failure modes of the hybrid HPS girder with a 275.8 MPa (40 ksi) web were similar to those of the hybrid HPS girder with a 344.8 MPa (50 ksi) web. The only major difference seen was with the girder having a flange slenderness ration of 4.0. For the hybrid HPS girder with a 275.8 MPa web and a flange slenderness ratio of 4.0, the girder experienced severe interactive lateral and local buckling in the same region where the vertical flange buckling would usually occur. For a flange slenderness ratio of 3.0, the hybrid HPS girder once again experienced severe vertical flange buckling, very similar to that shown in Figure 53.

The homogeneous 344.8 MPa girder with *d/2* bracing is dominated by the failure mode consisting with interactive local and lateral torsional buckling. This failure mode is severe for the girder with a flange slenderness ratio of 5.0 but gradually diminishes as the flange slenderness ratio decreases to three. The interactive local and lateral torsional buckling occurs in the same region along the longitudinal axis of the girder as the hybrid HPS girders. Similar to the hybrid HPS girders, flange local buckling occurs between the midspan stiffener and an adjacent intermediate stiffener.

In general, the following observations are made for the *d/2* case. For flange slenderness ratios of 5.0 and 4.5, moderate local flange buckling and moderate vertical flange buckling occur in the same half span of the girder, as described for the particular cases above and seen in Figure 52. The hybrid HPS girders in these cases are still able to achieve rotation capacities close to or just above three. With a flange slenderness ratio of 3.0, all hybrid HPS girders with *d/2* bracing experience severe vertical flange buckling and a significant decline in rotation capacity. In addition, this abrupt reduction in rotation

capacity becomes more severe as the web yield strength declines from 413.7 MPa (60 ksi) to 275.8 MPa (40 ksi).

Table 5 General Flexural Behavior of Girders with *d/2* Bracing

HPS Hybrid Girder w/ 413.7 MPa (60 ksi), d/2 Bracing

$b_f/2t_f$	Local Buckling (*)	Lateral Torsional Buckling	Vertical Flange Buckling	Interactive Local Buckling & LTB (**)	R = 3	Minimum R	Maximum R
5.0	✔ ✔		✔ ✔	✔			
4.5	✔		✔	✔	✔		
4.0	✔			✔	✔		✔
3.5	✔			✔	✔		
3.0	✔		✔ ✔	✔		✔	

HPS Hybrid Girder w/ 344.75 MPa (50 ksi), d/2 Bracing

$b_f/2t_f$	Local Buckling (*)	Lateral Torsional Buckling	Vertical Flange Buckling	Interactive Local Buckling & LTB (**)	R = 3	Minimum R	Maximum R
5.0	✔ ✔		✔	✔			
4.5	✔ ✔	✔		✔ ✔	✔		✔
4.0	✔	✔		✔	✔		
3.5	✔	✔			✔		
3.0		✔	✔ ✔ ✔			✔	

HPS Hybrid Girder w/ 275.8 MPa (40 ksi), d/2 Bracing

$b_f/2t_f$	Local Buckling (*)	Lateral Torsional Buckling	Vertical Flange Buckling	Interactive Local Buckling & LTB (**)	R = 3	Minimum R	Maximum R
5.0	✔ ✔	✔	✔ ✔		✔		
4.5	✔	✔			✔		✔
4.0	✔			✔ ✔ ✔	✔		
3.5	✔	✔		✔			
3.0		✔	✔ ✔ ✔			✔	

Homogeneous 344.75 MPa (50 ksi) Girder, d/2 Bracing

$b_f/2t_f$	Local Buckling (*)	Lateral Torsional Buckling	Vertical Flange Buckling	Interactive Local Buckling & LTB (**)	R = 3	Minimum R	Maximum R
5.0	✔			✔ ✔ ✔	✔		
4.5	✔			✔ ✔ ✔	✔		
4.0	✔			✔ ✔	✔		✔
3.5	✔			✔	✔		
3.0	✔			✔	✔	✔	

* Refers to isolated local buckling of the flange

** Refers to local and lateral torsional buckling occuring at a specific region along the longitudinal axis

5.3.3 *d* Bracing Results

As can be seen in Tables 6 and C3, almost all hybrid HPS girders analyzed with an unbraced length of *d* were able to attain and surpass the desired rotation capacity (*R*) of three as needed for moment redistribution. In addition, the homogeneous 344.8 MPa (50 ksi) girder, so braced, was able to attain the largest rotation capacities of any girder analyzed in the entire parametric study. The *d* bracing case demonstrated the most favorable and consistent results of the three bracing cases analyzed. The maximum rotation capacity for all girders (both hybrid and homogeneous) with unbraced lengths of *d* occurred with a flange slenderness equal to 3.5. For both the hybrid HPS and homogenous girders, as the flange slenderness ratio increased from 3.5 to 5.5, the rotation capacity decreased. Like the *d/2* case, a significant decline in rotation capacity resulted from a flange slenderness ratio of 3.0. This is due to severe vertical buckling of the flange similar to that of the *d/2* bracing case. The moment versus rotation plots for *d* bracing (Figures C9 – C11) are characteristic of Mode 1 moment-rotation plots as described by Earls (1999) and discussed in the previous section.

5.3.3.1 Detailed description of model behavior with *d* bracing. The failure modes for each hybrid HPS girder flange and web steel combination followed the same pattern: severe flange local buckling occurred between the midspan stiffener and an adjacent intermediate stiffener for flange slenderness ratios of 5.5, 5.0, and 4.5. This is illustrated in Figure 54. For the flange slenderness ratio of 4.0, severe vertical flange buckling

occurred away from the intermediate stiffeners as shown in Figure 55. Severe vertical flange buckling also occurred for the flange slenderness ratio of 3.5 but directly at the load point as illustrated in Figure 56. The midspan stiffener also buckled slightly in this case. The flange slenderness ratio of 3.0 experienced even more severe flange vertical buckling at the load point as shown in Figure 57. The midspan stiffener was severely buckled in this case. As a result of the high flange slenderness ratio of 5.5, the severe flange local buckling either prevented the hybrid HPS girder from reaching a rotation capacity of three or barely allowed the hybrid HPS girder to obtain a capacity of three. In contrast, as a result of the stocky flange slenderness ratio of 3.0, the more severe vertical flange buckling, in conjunction with the buckling of the midspan bearing stiffener, resulted in a very low rotation capacity.

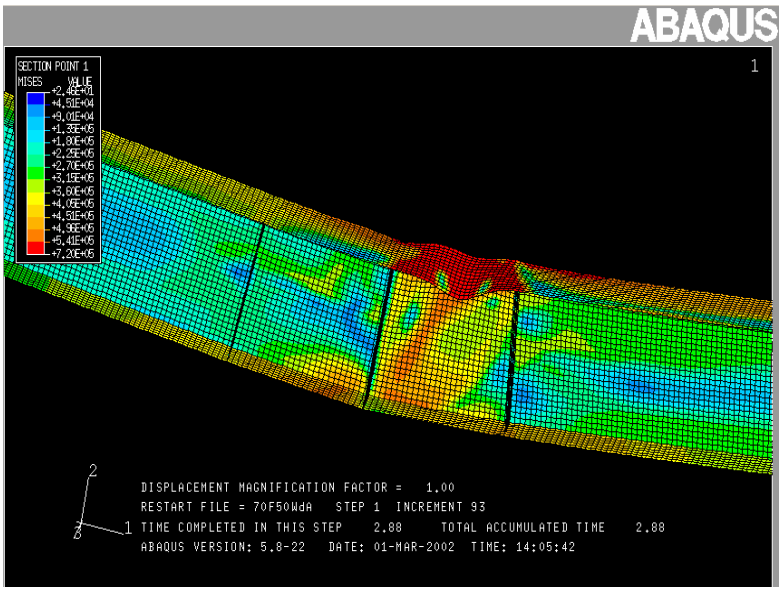

Figure 54 Illustration of Local Buckling for Hybrid HPS Girder with *d* Bracing

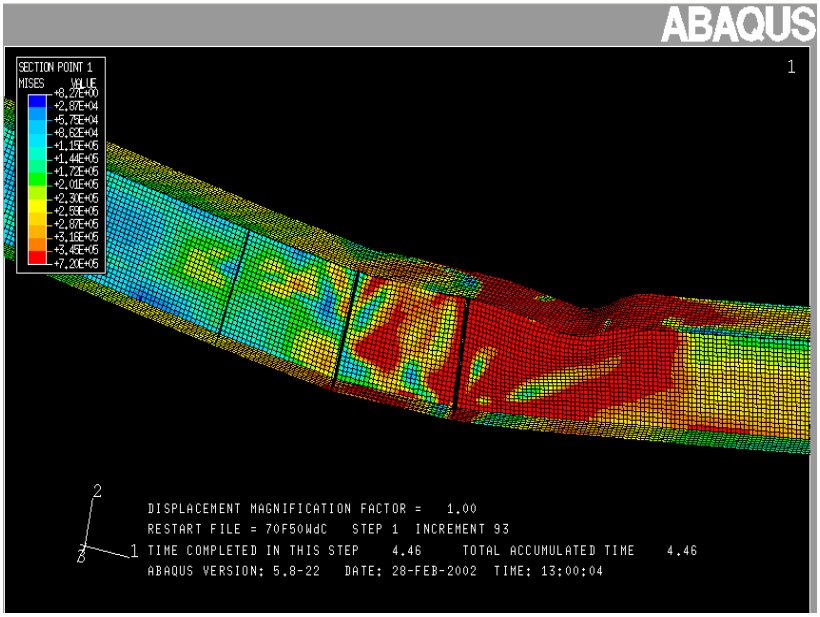

Figure 55 Illustration of Vertical Flange Buckling for hybrid HPS girder with *d* Bracing; $b_f/2t_f = 4.0$

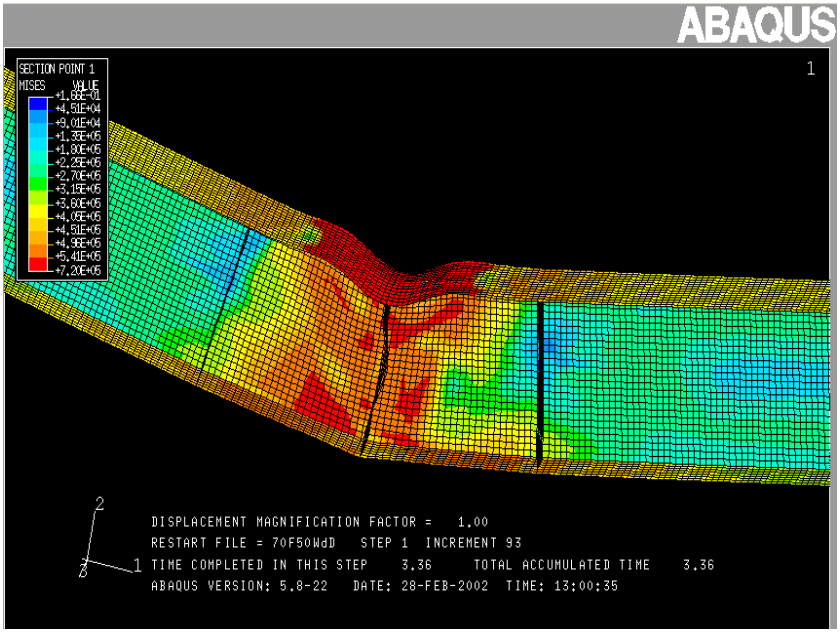

Figure 56 Illustration of Vertical Flange Buckling for hybrid HPS girder with *d* Bracing; $b_f/2t_f = 3.5$

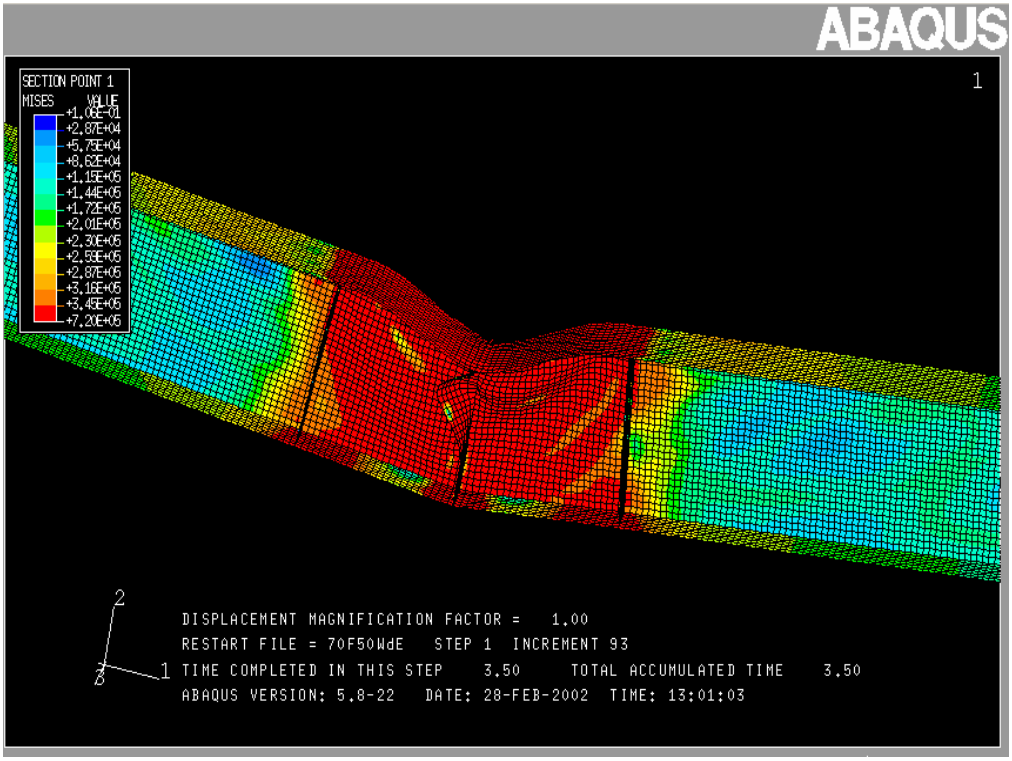

Figure 57 Illustration of Vertical Flange Buckling for Hybrid HPS Girder with *d* Bracing; $b_f/2t_f = 3.0$

The failure modes of the homogeneous 344.8 MPa girders with *d* bracing were dominated by extreme interactive local and global buckling of the girder. This was accompanied by severe local buckling about the midspan in most cases. This failure mode is illustrated in Figure 58. The one exception is the homogeneous girder with a flange slenderness ratio of 3.5, which experienced extremely large in-plane deformations illustrated in Figure 59. This girder achieved the highest rotation capacity as seen in Table C3.

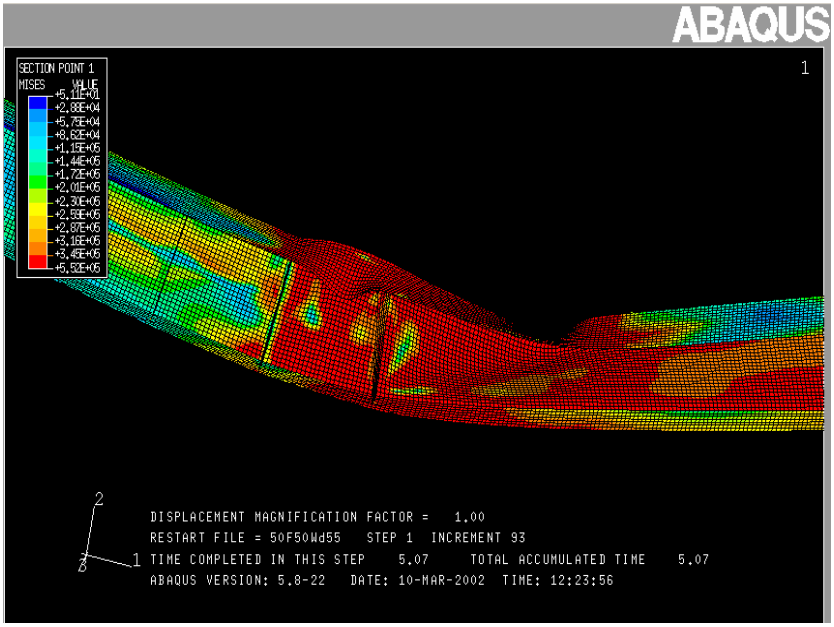

Figure 58 Illustration of Dominant Failure Mode for Homogeneous 344.8 MPa (50 ksi) with *d* bracing

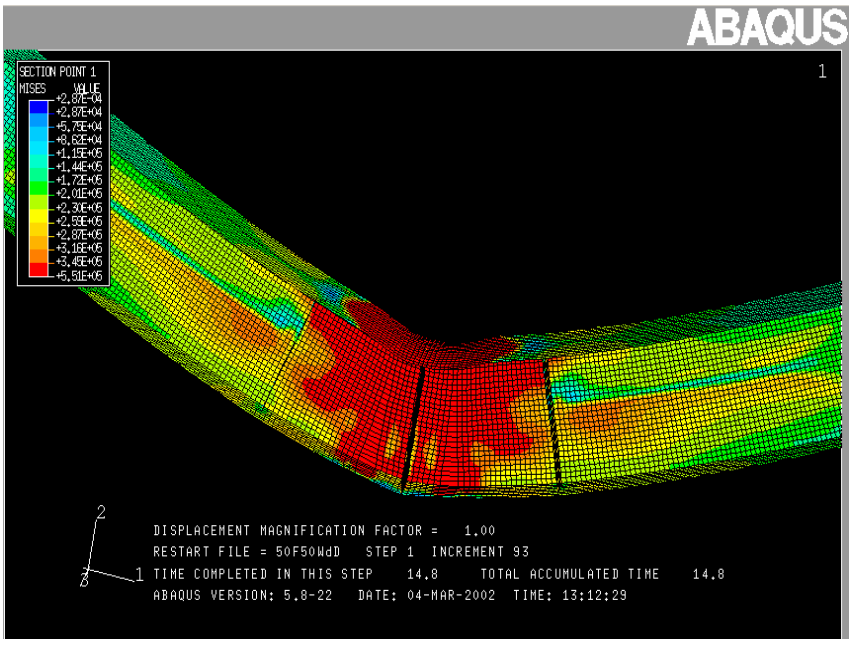

Figure 59 Illustration of Dominant Failure Mode for Homogeneous 344.8 MPa (50 ksi) with *d* bracing

Table 6 General Flexural Behavior of Girders with *d* Bracing

HPS Hybrid Girder w/ 413.7 MPa (60 ksi), d Bracing Bracing

$b_f/2t_f$	Local Buckling (*)	Lateral Torsional Buckling	Vertical Flange Buckling	Interactive Local Buckling & LTB (**)	R = 3	Minimum R	Maximum R
5.5	✔ ✔ ✔					✔	
5.0	✔ ✔ ✔				✔		
4.5	✔ ✔ ✔				✔		
4.0	✔ ✔	✔	✔ ✔ ✔		✔		
3.5			✔ ✔ ✔		✔		✔
3.0							

HPS Hybrid Girder w/ 344.75 MPa (50 ksi), d Bracing

$b_f/2t_f$	Local Buckling (*)	Lateral Torsional Buckling	Vertical Flange Buckling	Interactive Local Buckling & LTB (**)	R = 3	Minimum R	Maximum R
5.5	✔ ✔ ✔						
5.0	✔ ✔ ✔				✔		
4.5	✔ ✔ ✔				✔		
4.0	✔ ✔	✔	✔ ✔ ✔		✔		
3.5			✔ ✔ ✔		✔		✔
3.0			✔ ✔ ✔			✔	

HPS Hybrid Girder w/ 275.8 MPa (40 ksi), d Bracing

$b_f/2t_f$	Local Buckling (*)	Lateral Torsional Buckling	Vertical Flange Buckling	Interactive Local Buckling & LTB (**)	R = 3	Minimum R	Maximum R
5.5	✔ ✔ ✔				✔		
5.0	✔ ✔ ✔				✔		
4.5	✔ ✔ ✔				✔		
4.0	✔ ✔	✔	✔ ✔ ✔		✔		
3.5			✔ ✔ ✔		✔		✔
3.0			✔ ✔ ✔			✔	

Homogeneous 344.75 MPa (50 ksi) Girder, d Bracing

$b_f/2t_f$	Local Buckling (*)	Lateral Torsional Buckling	Vertical Flange Buckling	Interactive Local Buckling & LTB (**)	R = 3	Minimum R	Maximum R
5.5	✔ ✔ ✔			✔ ✔ ✔	✔	✔	
5.0	✔ ✔ ✔			✔ ✔ ✔	✔		
4.5	✔			✔ ✔ ✔	✔		
4.0	✔			✔ ✔ ✔	✔		
3.5	✔ ✔ ✔				✔		✔
3.0	✔ ✔			✔ ✔ ✔	✔		

* Refers to isolated local buckling of the flange

** Refers to local and lateral torsional buckling occuring at a specific region along the longitudinal axis

5.3.4 Additional Parametric Studies Results

As can be seen from Table 7 and C4, neither the AASHTO Interaction (as described in Chapter 2.0) Case 1 nor Case 2 was able to attain the desired rotation capacity (R) of three as needed for moment redistribution. The three AASHTO Interaction Case 1 hybrid HPS girders were able to achieve their respective plastic moments but with very little rotation capacity, as seen in Figure C13. The three AASHTO Interaction Case 2 hybrid HPS girders were not able to achieve their respective plastic moments as seen in Figure C14. All AASHTO Interaction Case 1 hybrid HPS girders experienced moderate flange local buckling about the midspan stiffener as well as moderate lateral torsional buckling as illustrated in Figure 60. The AASHTO interaction Case 2 hybrid HPS girders experienced severe flange local buckling symmetric about the midspan stiffener and longitudinal axis. This is shown in Figure 61.

The homogeneous 275.8 MPa (40 ksi) girder braced according to AASHTO Specification (Section 6.10.4.1.7), was able to attain and surpass the desired rotation capacity (R) of three as needed for moment redistribution as seen in Table C4. The moment versus rotation plot is characteristic of Mode 1 moment-rotation plots described by Earls (1999) and discussed in Section 5.3.2. This is illustrated in Figure C15. The failure mode consisted of moderate flange local buckling on one side of the midspan stiffener and interactive local and lateral torsional buckling on the other. This is illustrated in Figure 62.

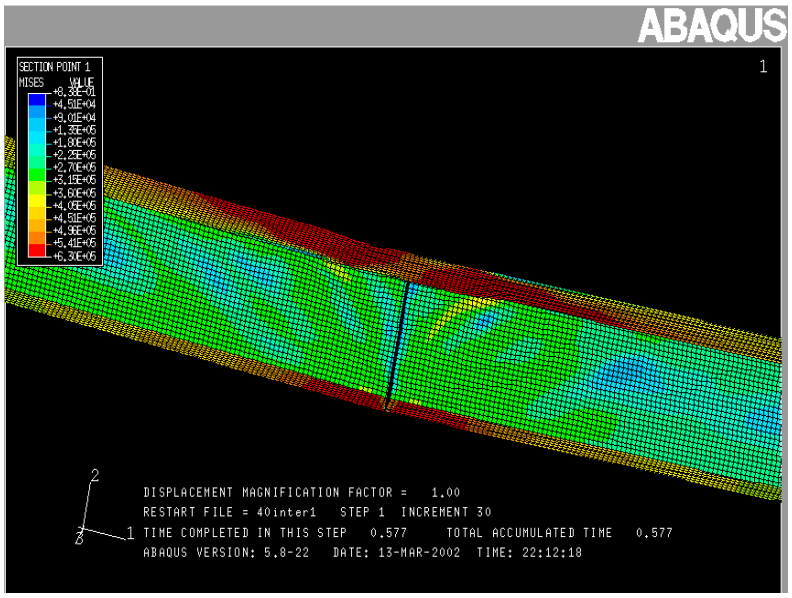

Figure 60 Illustration of Failure Mode for AASHTO Interaction Case 1 Hybrid HPS Girders

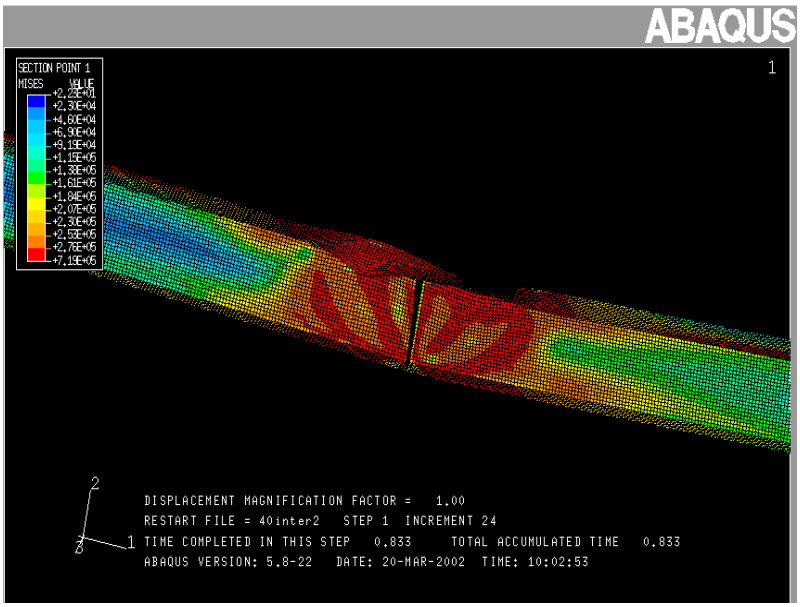

Figure 61 Illustration of Failure Mode for AASHTO Interaction Case 2 Hybrid HPS Girders

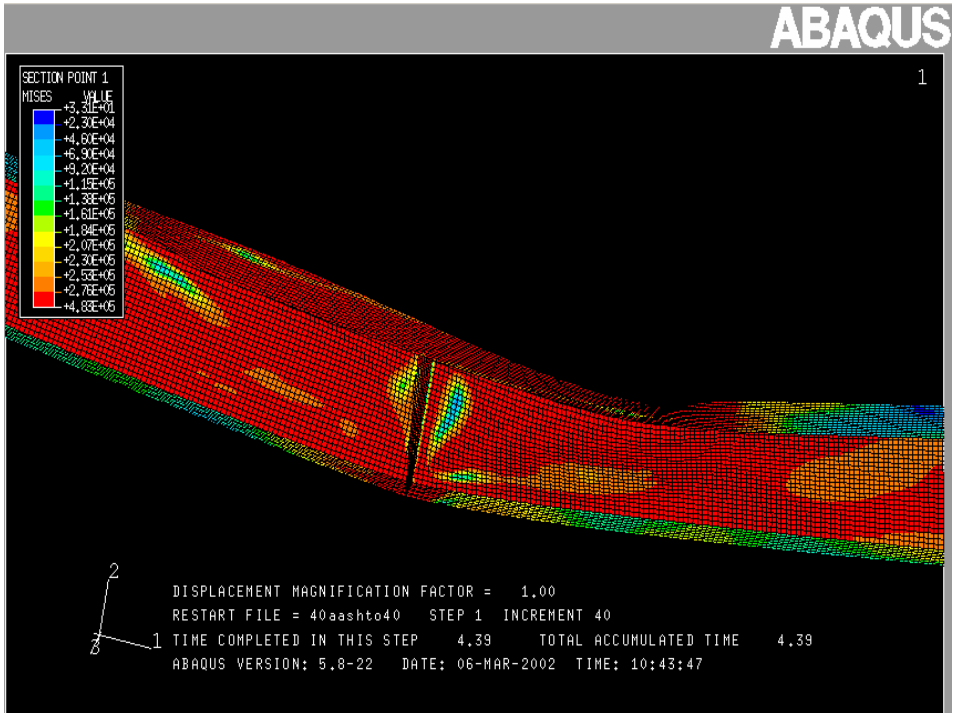

Figure 62 Illustration of Failure Mode for Homogeneous 275.8 MPa (40 ksi) Girder; AASHTO Bracing

Table 7 General Flexural Behavior of Additional Parametric Studies

AASHTO Interaction Case 1 (bf/2tf = 5.51, h/tw = 72.3)

Web Yield Strength (MPa)	Local Buckling (*)	Lateral Torsional Buckling	Vertical Flange Buckling	Interactive Local Buckling & LTB (**)	R = 3	Minimum R	Maximum R
540.7	✔	✔				✔	
413.7	✔ ✔	✔ ✔					✔
344.8	✔ ✔	✔ ✔					

AASHTO Interaction Case 2 (bf/2tf = 7.34, h/tw = 54.2)

Web Yield Strength (MPa)	Local Buckling (*)	Lateral Torsional Buckling	Vertical Flange Buckling	Interactive Local Buckling & LTB (**)	R = 3	Minimum R	Maximum R
540.7	✔ ✔ ✔						
413.7	✔ ✔ ✔						
344.8	✔ ✔ ✔						

Homogeneous 275.8 MPa (40 ksi) Girder, AASHTO Bracing

$b_f/2t_f$	Local Buckling (*)	Lateral Torsional Buckling	Vertical Flange Buckling	Interactive Local Buckling & LTB (**)	R = 3	Minimum R	Maximum R
4	✔ ✔			✔ ✔ ✔	✔		

* Refers to isolated local buckling of the flange
** Refers to local and lateral torsional buckling occuring at a specific region along the longitudinal axis

6.0 CONCLUSIONS

The current study employs experimentally verified nonlinear finite element techniques to explore hybrid HPS girder compactness and bracing requirements. While the AASHTO (1998) provisions have been shown in the current study to be adequate for homogeneous girders made of conventional steels (344.8 MPa and 275.8 MPa), it is concluded from the current work that the existing AASHTO bridge specification compactness and bracing provisions, as applied to hybrid HPS girders, are insufficient for providing adequate rotation capacity for inelastic force redistribution to take place. As a result of the applied unbraced length according to AASHTO (1998) Section 6.10.4.1.7, compact web hybrid HPS girders experience local and/or global buckling which prohibits the achievement of a rotation capacity equal to or greater than 3. In addition, the rotation capacity results obtained in the current study are contrary to the notion that rotation capacity increased with decreasing flange slenderness.

From the current study it is observed that a significant improvement in rotation capacity (more than double that of the AASHTO bracing case) can be achieved with HPS girders when utilizing an unbraced length equal to half the depth (d) of the compact hybrid HPS girders by the current study. It is noted that low flange slenderness values ($b_f/2t_f$ = 3.0) result in severe vertical flange buckling. Also, in some high flange slenderness cases ($b_f/2t_f$ = 5.5), local buckling prohibits the achievement of a rotation capacity of 3.

Based on the current parametric study, it is recommended that an unbraced length equal to the depth of the girder be applied to hybrid HPS girders in flexure. In addition, it is recommended that a lower and upper bound to the flange slenderness ratio of 5.0 and 3.5, respectively, be applied to hybrid HPS girders in flexure in order to prevent the occurrence of local and or vertical buckling interfering with the attainment of a rotation capacity of three or more.

In summary, for hybrid HPS girders to achieve $R = 3$:

L_b = depth of cross-section

$3.5 = b_f/2t_f = 5.0$

$h/t_w \tilde{} 45$

The conclusions are tentative since web slenderness and bracing stiffeness were not examined as part of this study.

6.1 Recommendations

Future research is needed in order to further investigate the flexural behavior of hybrid HPS girder in flexure and eventually formulate design provisions that can assure the attainment of a sufficient rotation capacity. Web slenderness ratios of various conventional steels need to be investigated in conjunction with the flange slenderness ratios considered in the current parametric study in order to access the effects that this parameter has on hybrid HPS girder rotation capacity. In addition, different values for the lateral bracing stiffness need to be considered based on the findings of Thomas and Earls (2002). With this future research, a more conclusive analysis may be done on the flexural behavior of hybrid girders using HPS flanges and conventional steel webs.

APPENDIX

APPENDIX A

Appendix A

Material Properties

Table A1 gives the material properties of the different steels used in the current study. The plastic values of the respective materials are specified as points along the true stress versus true strain plot shown in Figure A1. These values are included in the ABAQUS Input file. ABAQUS will use these material properties to extrapolate a yield surface in three-dimensional principal stress space as described in Sections 3.3 and 3.4.

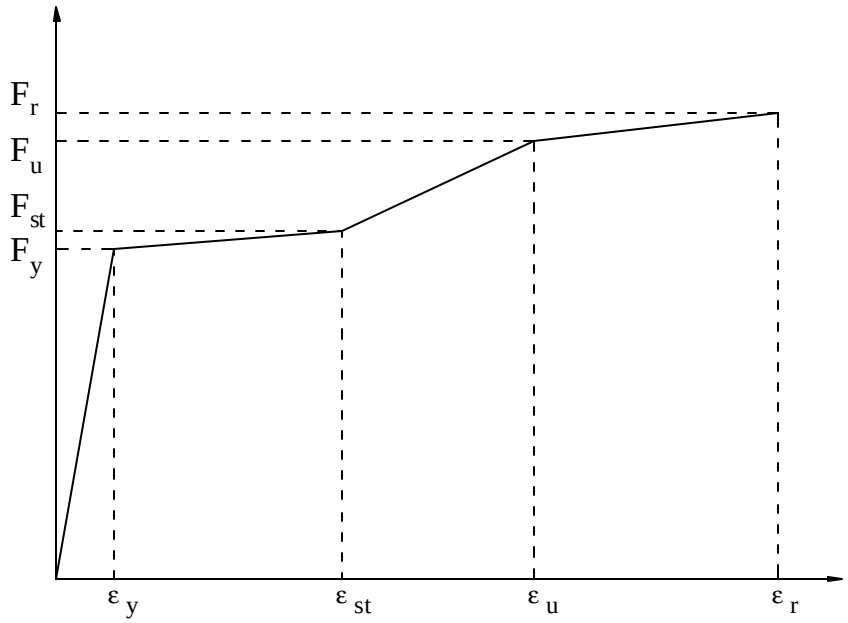

Figure A1 Constitutive Law – True Stress versus True Strain (Logarithmic Strain)

Table A1 Material Properties for Steels Used in Current Study

	HPS Steel		40 ksi Steel	
	ε_{ln}^{pl}	σ_{true} (MPa)	ε_{ln}^{pl}	σ_{true} (MPa)
Yielding	0	540.627	0	275.800
Strain Hardening (ε_y, F_y)	0.009667822	550.799	0.009229480	285.073
Strain Hardening (ε_{st}, F_{st})	0.049084972	653.885	0.055723800	448.175
Ultimate (ε_u, F_u)	0.091786387	704.579	0.090034000	482.650
Rupture (ε_r, F_r)	0.114179156	720.592	---	---

	50 ksi Steel		60 ksi Steel	
	ε_{ln}^{pl}	σ_{true} (MPa)	ε_{ln}^{pl}	σ_{true} (MPa)
Yielding	0	344.750	0	413.700
Strain Hardening (ε_y, F_y)	0.009229480	354.023	0.009229480	422.973
Strain Hardening (ε_{st}, F_{st})	0.055723800	517.125	0.055723800	586.075
Ultimate (ε_u, F_u)	0.090034000	551.600	0.090034000	620.550
Rupture (ε_r, F_r)	---	---	---	---

The true stress (σ_{true}) and logarithmic plastic strain ($\varepsilon_{\ln}^{pl}$) are expressed in terms of engineering stress and strain, respectively as:

$$\sigma_{true} = \sigma_{eng}(1+\varepsilon_{eng})$$

$$\varepsilon_{\ln}^{pl} = \ln(1+\varepsilon_{eng}) - \frac{\sigma_{true}}{E}$$

Table A2 Yield Stress Conversions

F_y (ksi)	F_y (MPa)
78.411	540.627
60.000	413.700
50.000	344.750
40.000	275.800

APPENDIX B

Appendix B

Model Geometry

B.1 Geometry of Models for HPS Flange Slenderness Parametric Study

This section of Appendix B deals with the geometric properties of the model used for the HPS flange slenderness parametric study described in Section 5.1. Table B1 lists the cross-sectional dimensions that change as a function of the flange slenderness ratio. Included in Table B1 is the AASHTO bracing model's unbraced length associated with each flange slenderness ratio. The AASHTO unbraced length is a function of the cross-section's radius of gyration about the weak axis (r_y). All other unbraced lengths, *d* and *d/2*, remain constant with each flange slenderness ratio and are therefore, not listed. Figures B1 and B2 illustrate the values contained in Table B1.

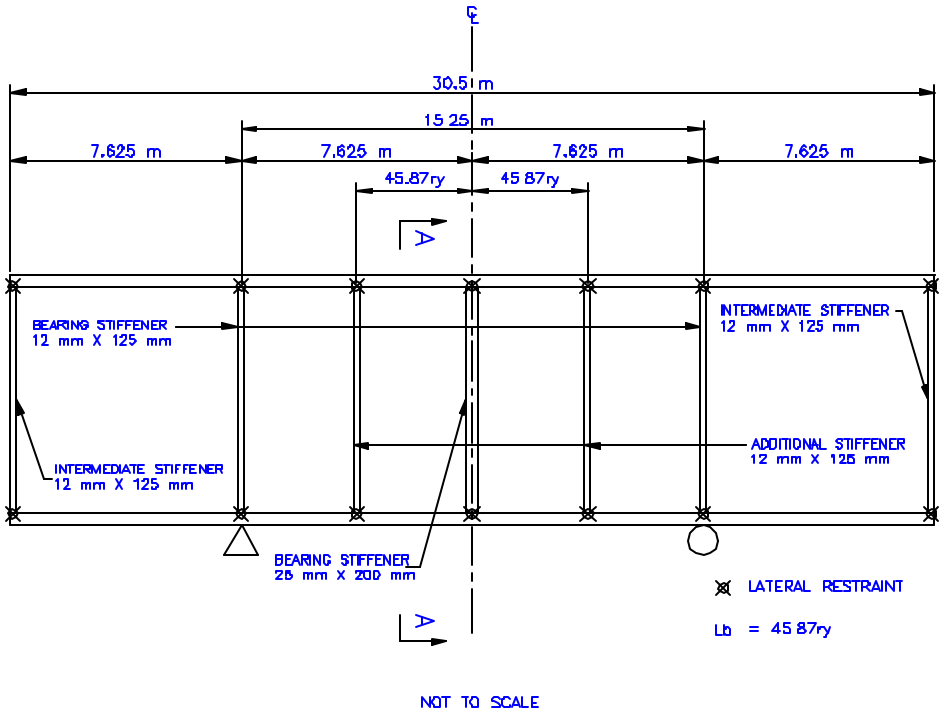

Figure B1 Elevation view of AASHTO Bracing Model Illustrating L_b as a Function of r_y

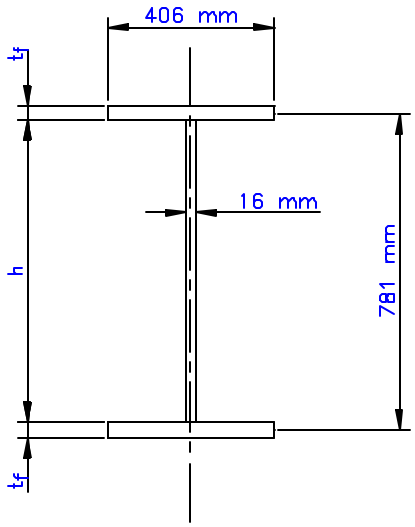

Figure B2 Illustration of Cross-Sectional Dimension

Table B1 Cross-Section Dimensions as a Function of Flange Slenderness RatiO

bf/2tf	b_f (mm)	t_f (mm)	h (mm)	t_w (mm)	h/t_w	r_y (m)	AASHTO Bracing L_b (m)
5.5	0.406	0.03691	0.74409	0.016	46.5056250	0.099182	4.54947834
5.0	0.406	0.04060	0.74040	0.016	46.2750000	0.100552	4.61232024
4.5	0.406	0.04500	0.73600	0.016	46.0000000	0.101949	4.67640063
4.0	0.406	0.05075	0.73025	0.016	45.6406250	0.103473	4.74630651
3.5	0.406	0.05800	0.72300	0.016	45.1875000	0.105032	4.81781784
3.0	0.406	0.06770	0.71330	0.016	44.5812500	0.106669	4.89290703

B.1 Geometry of Models for AASHTO Interaction Equation Investigation

This section of Appendix B deals with the geometric properties of the model used for the AASHTO interaction equation investigation described in Section 5.2. Two cases are analyzed in this investigation: (Interaction Case 1) the web slenderness is equal to the limit given by (2-11) with 75 percent of the flange slenderness limit given by (2-7); (Interaction Case 2) the flange slenderness is equal to its limit given by (2-7) with 75 percent of the resulting web slenderness given by (2-11). These two cases are considered for each combination of flange and web steel discussed in Section 5.1. The girder cross-sectional geometries of the two interaction cases are given in Table B2. Figures B1 and B2 may be used in conjunction with Table B2. In this study, the unbraced length is also calculated according to the AASHTO specifications.

Table B2 Cross-Section Dimensions for AASHTO Interaction Cases 1 and 2

	$b_f/2t_f$	b_f (mm)	t_f (mm)	h (mm)	t_w (mm)	h/t_w	r_y (mm)	AASHTO Bracing L_b (m)
Interaction Case 1	5.51	0.406	0.03684	0.74416	0.010802	72.3	0.104062981	4.773368938
Interaction Case 2	7.34	0.406	0.02766	0.75334	0.01441	54.2	0.096258582	4.415381156

APPENDIX C

Appendix C

Results

The rotation capacity values and moment versus rotation plots for all models analyzed in the current study are contained in this Appendix. The results of the parametric study are grouped into three main categories according to bracing schemes. The three main categories contain moment versus rotation plots of flange slenderness ratios ($b_f/2t_f$) for each flange and web yield strength combination, described in Section 5.1. Following the moment versus rotation plots of the parametric study are the moment versus rotation plots of the AASHTO interaction equation investigation and the homogeneous 275.8 MPa (40 ksi) girder analysis. The set of figures can be grouped into the following categories:

1. AASHTO Bracing Models; Figures C1 - C4
2. *d/2* Bracing Models; Figures C5 - C8
3. *d* Bracing Models; Figures C9 – C12
4. AASHTO Interaction Equation Case 1; Figure C13
5. AASHTO Interaction Equation Case 2; Figure C14
6. Homogeneous 275.8 MPa (40 ksi) Girder; Figure C15

Appendix C concludes with Tables C1 – C4 which summarize the rotation capacities of each model analyzed based on the preceding moment versus rotation plots. A more detailed description of the parametric study and additional studies are provided in

Section 5.1 and 5.2, respectively. Note that “70F60W” stands for a girder comprised of a HPS flange (F) with 60 ksi web (W).

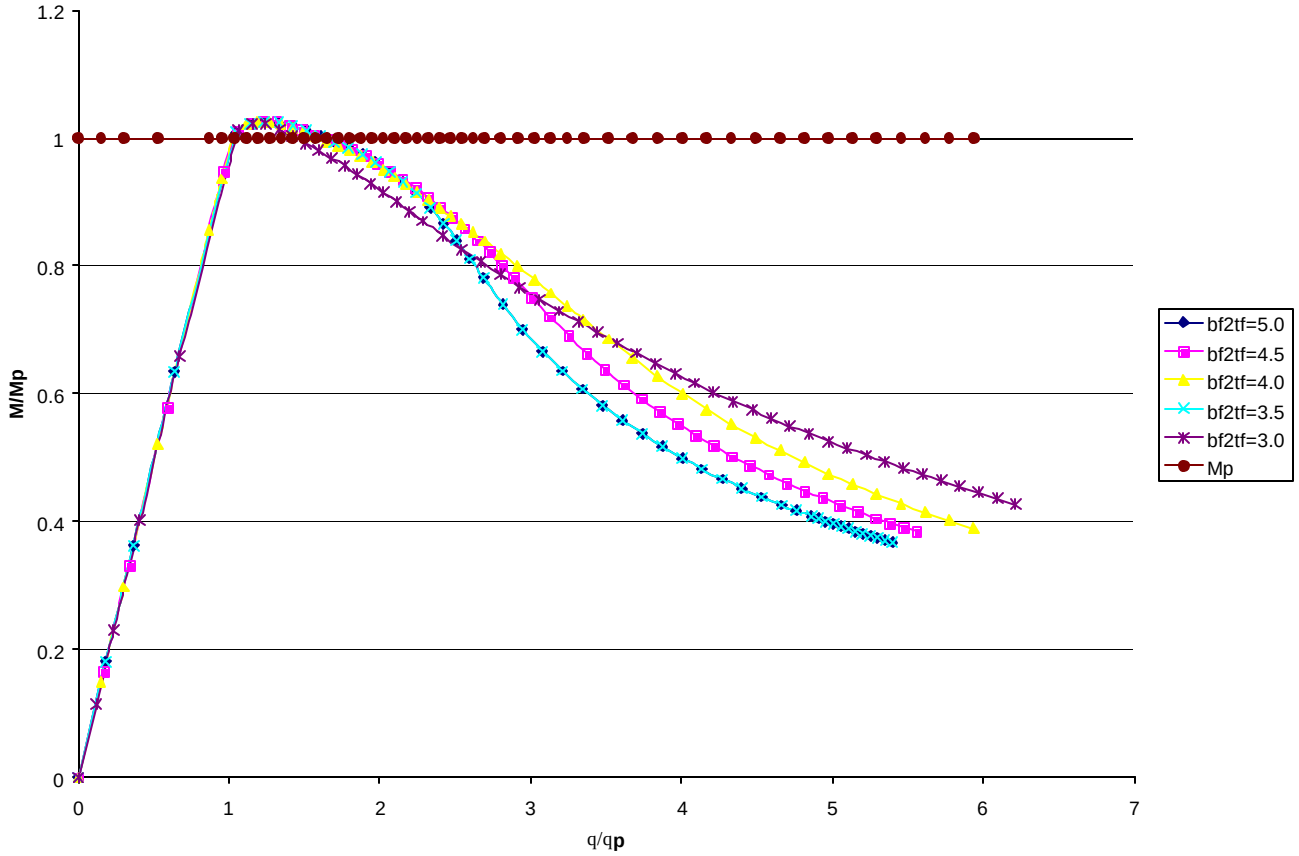

Figure C1 Moment Gradient Response of HPS Hybrid Girder with 413.7 MPa (60 ksi) Web; AASHTO Bracing

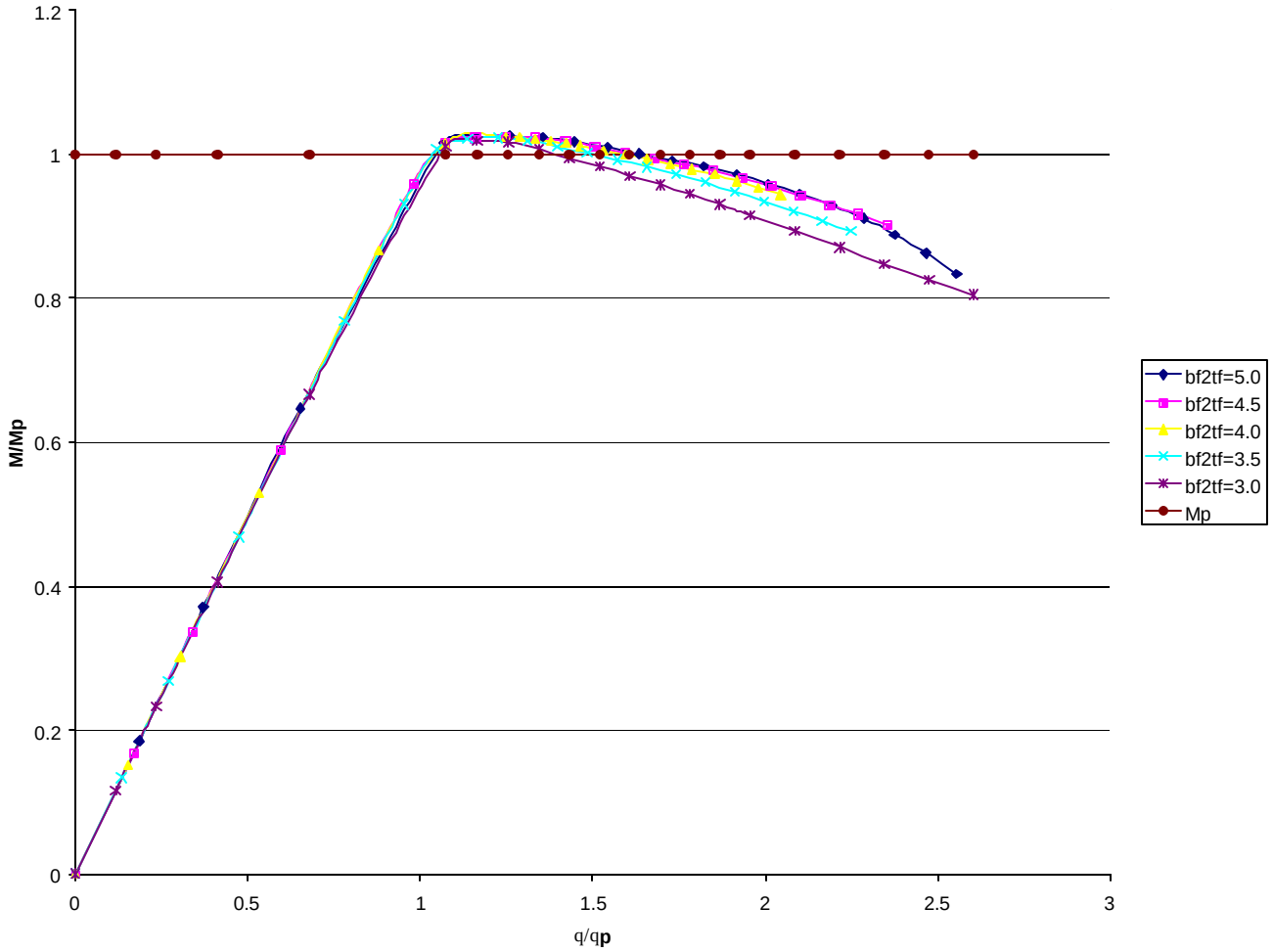

Figure C2 Moment Gradient Response of HPS Hybrid Girder with 344.75 MPa (50 ksi) Web; AASHTO Bracing

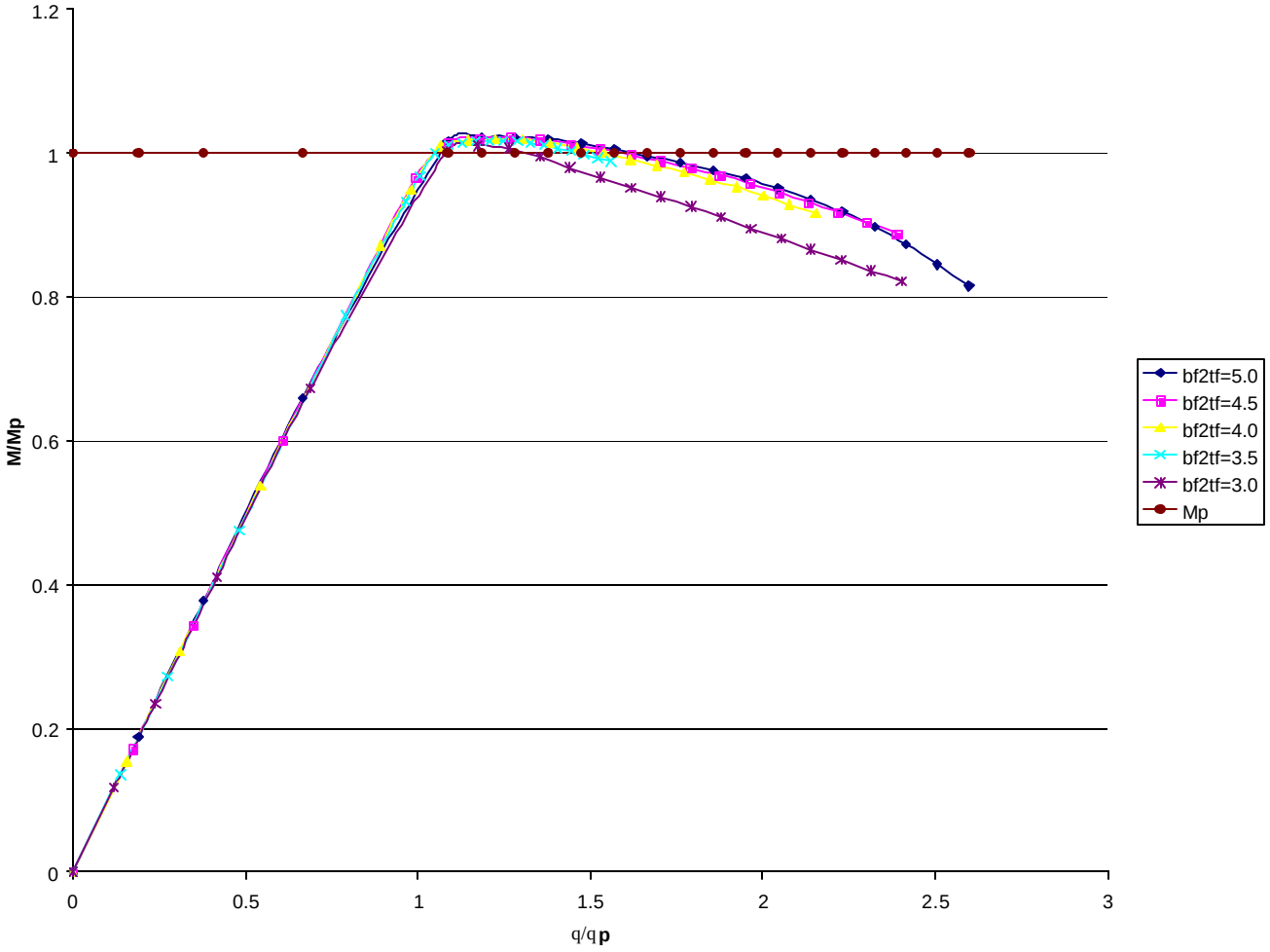

Figure C3 Moment Gradient Response of HPS Hybrid Girder with 275.8 MPa (40 ksi) Web; AASHTO Bracing

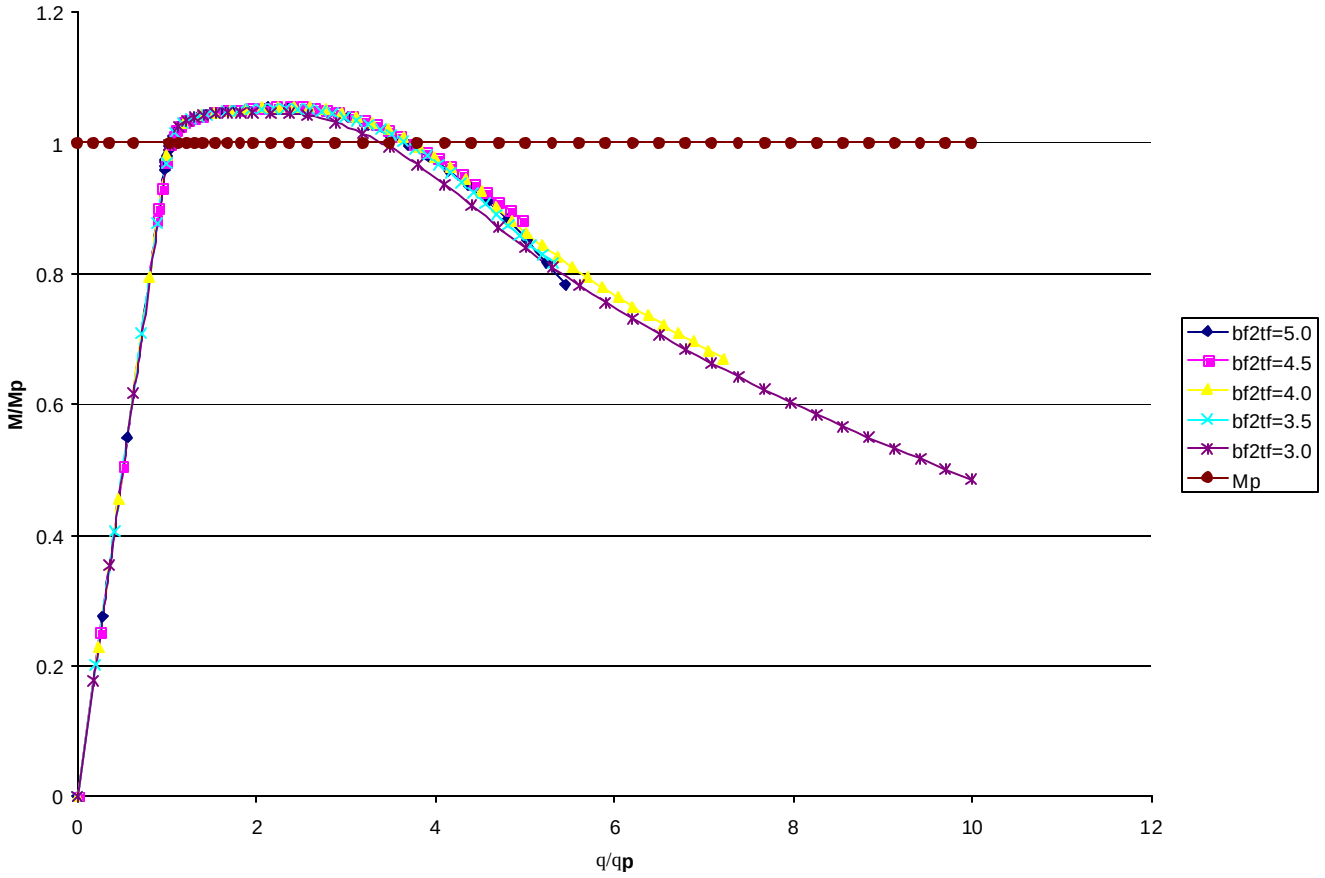

Figure C4 Moment Gradient Response of Homogeneous 344.75 MPa (50 ksi) Girder; AASHTO Bracing

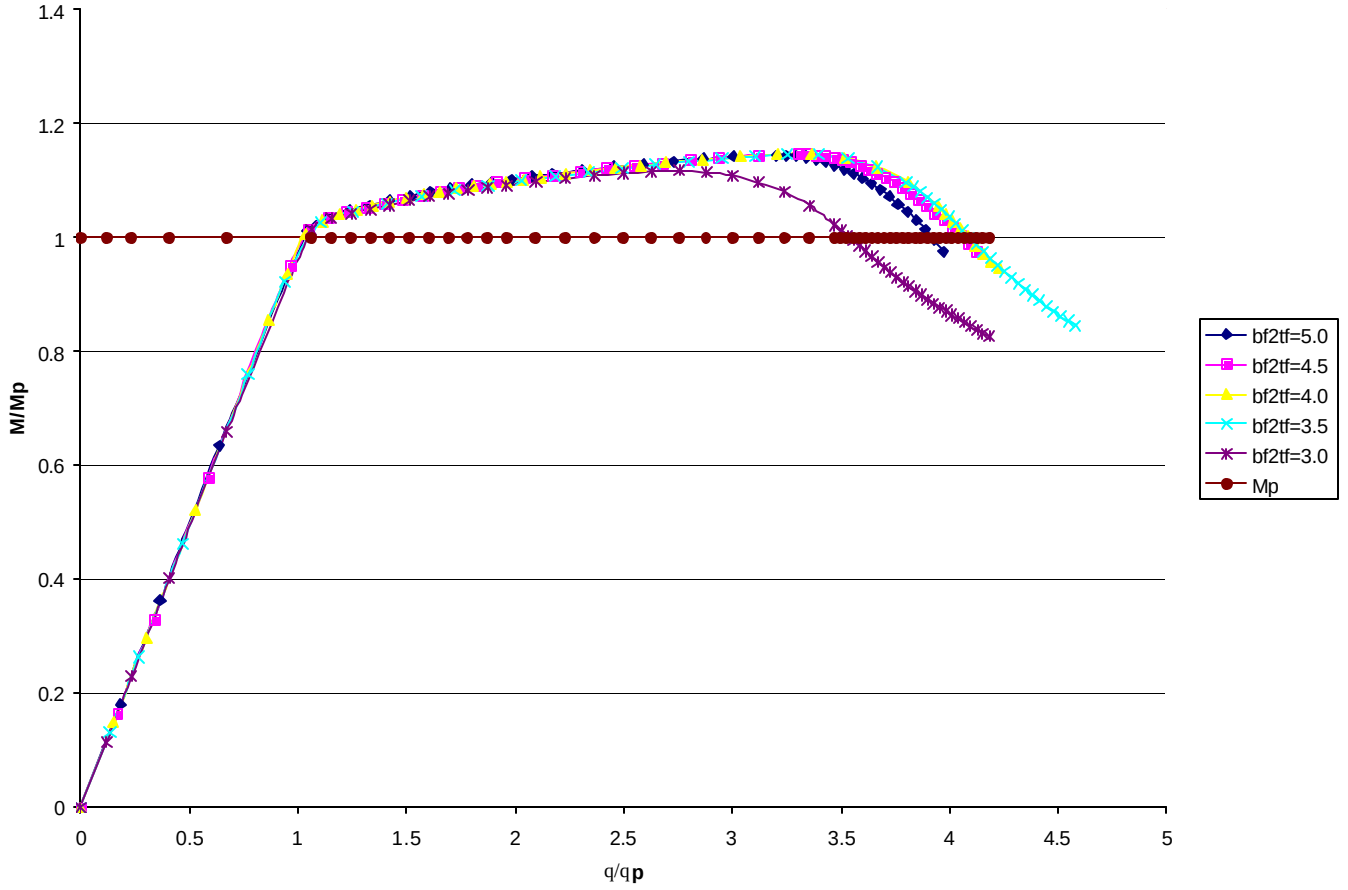

Figure C5 Moment Gradient Response of HPS Hybrid Girder with 413.7 MPa (60 ksi) Web; *d/2* Bracing

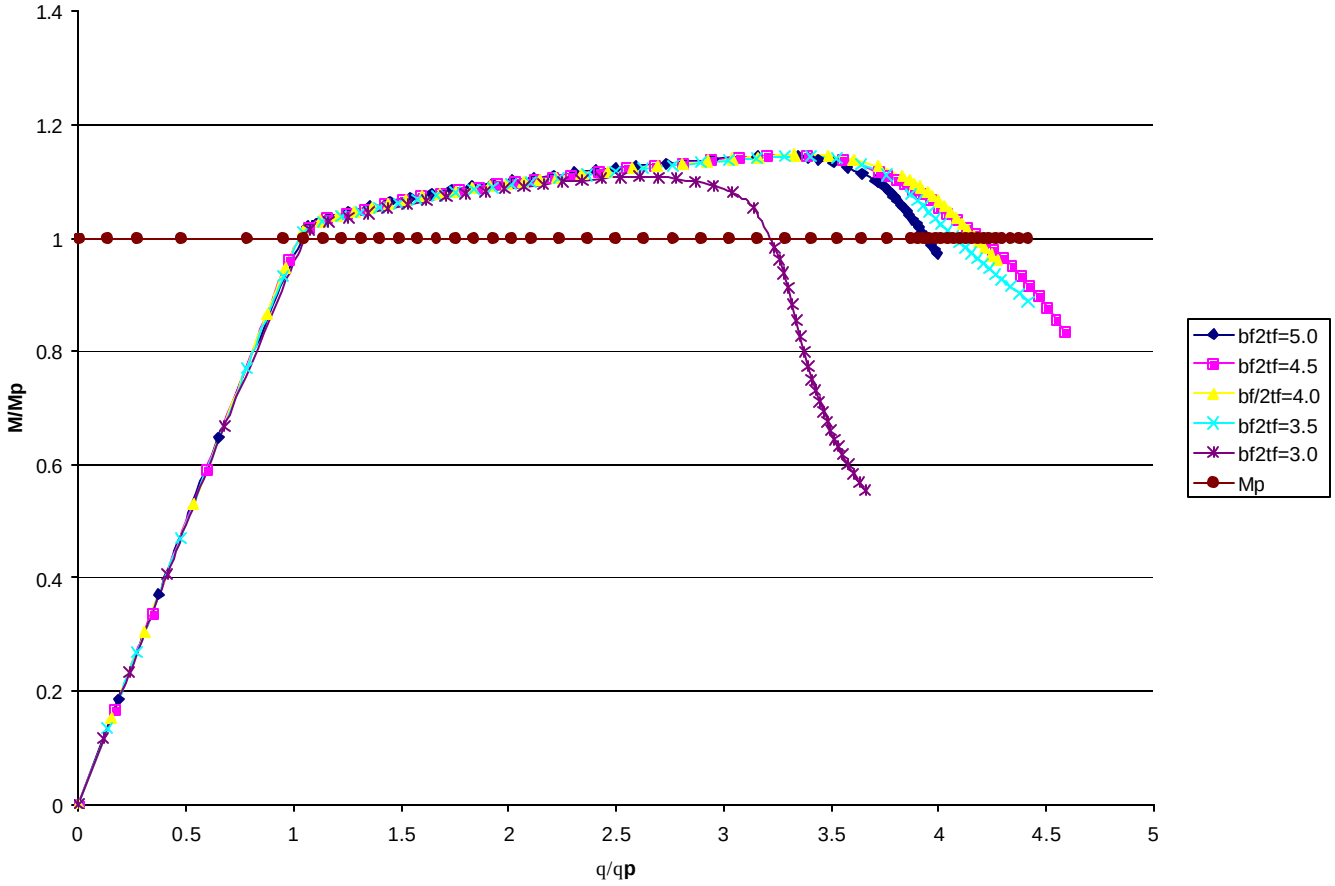

Figure C6 Moment Gradient Response of HPS Hybrid Girder with 344.75 MPa (50 ksi) Web; *d/2* Bracing

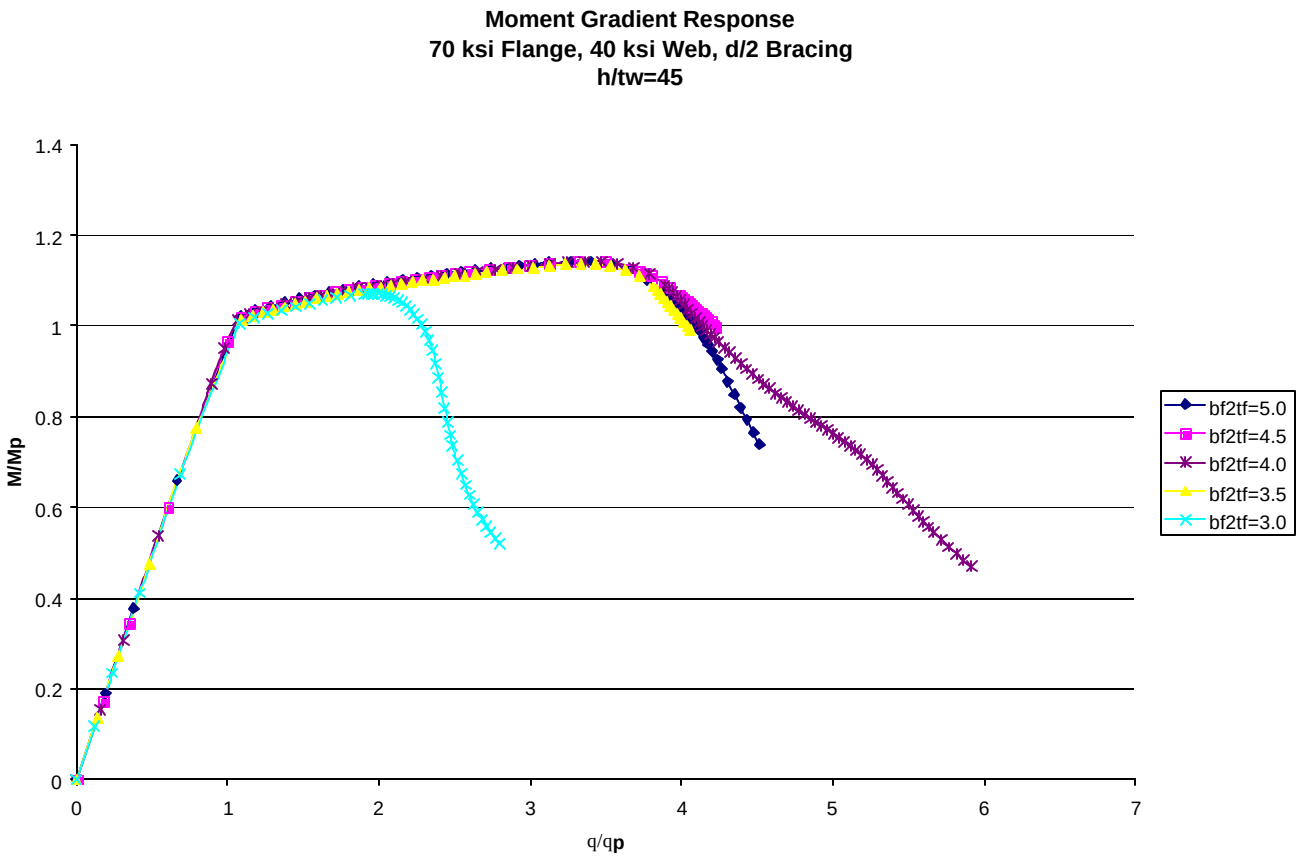

Figure C7 Moment Gradient Response of HPS Hybrid Girder with 344.75 MPa (40 ksi) Web; *d/2* Bracing

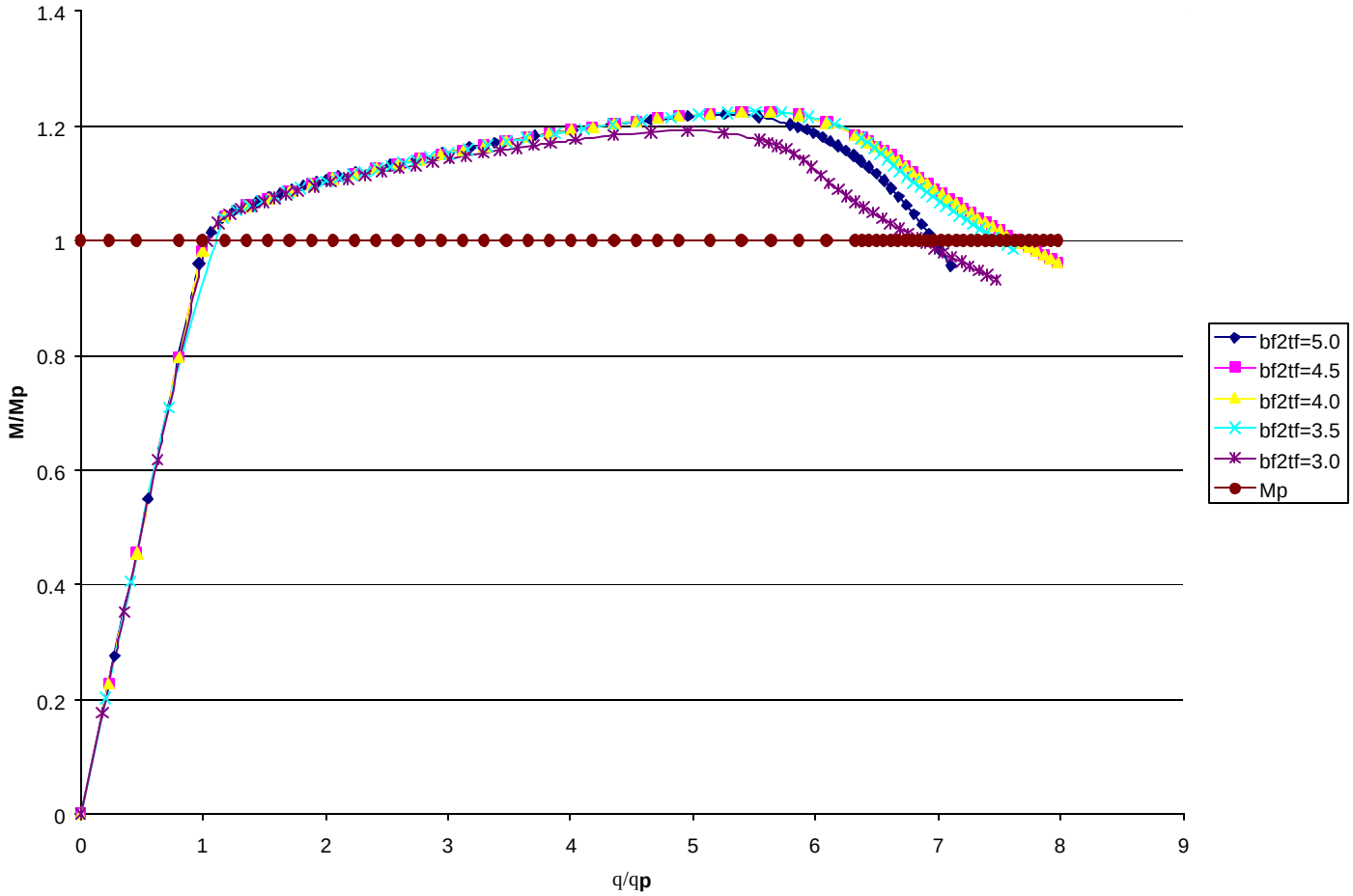

Figure C8 Moment Gradient Response of Homogeneous 344.75 MPa (50 ksi) Girder; *d/2* Bracing

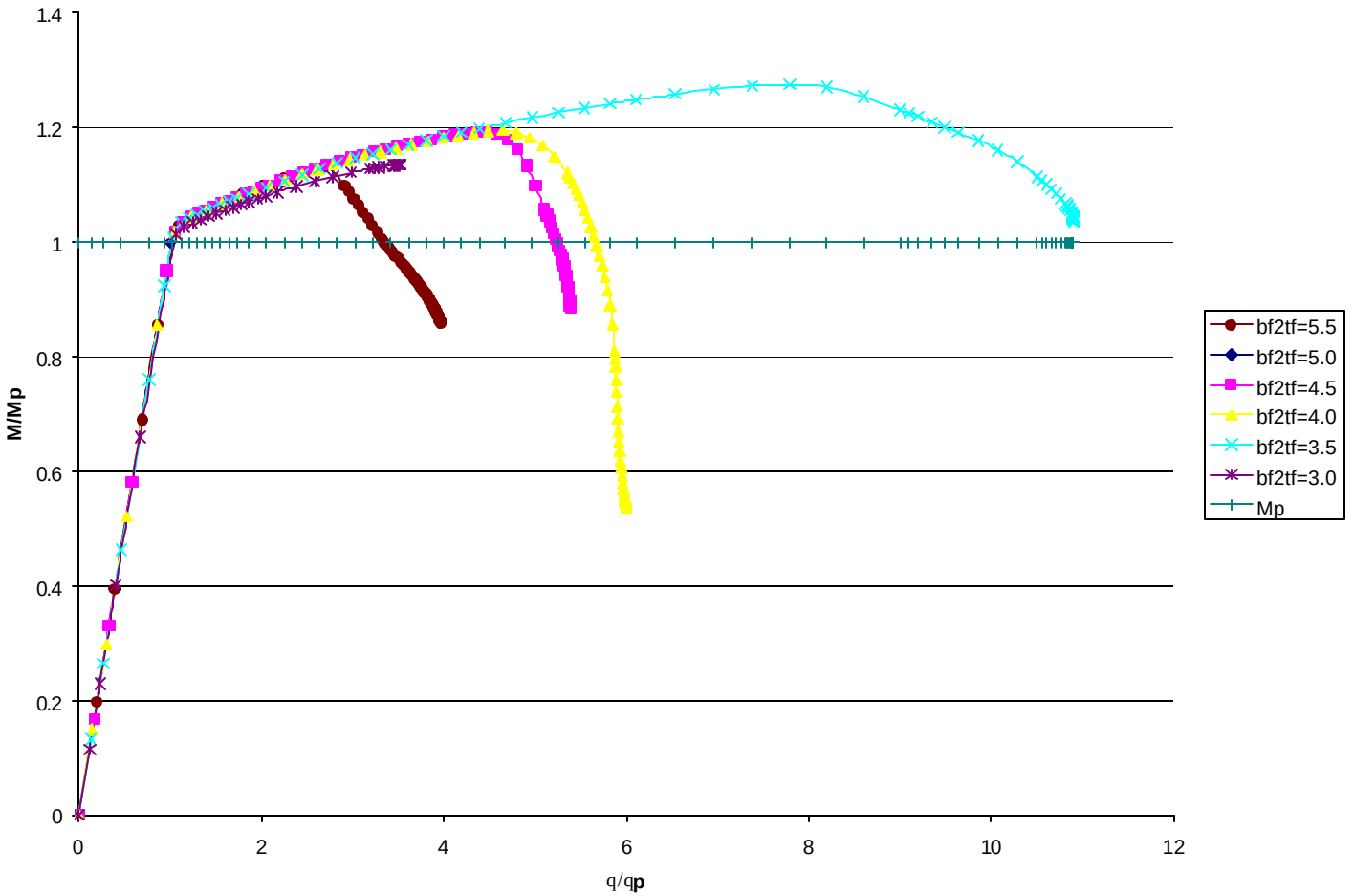

Figure C9 Moment Gradient Response of HPS Hybrid Girder with 413.7 MPa (60 ksi) Web; *d* Bracing

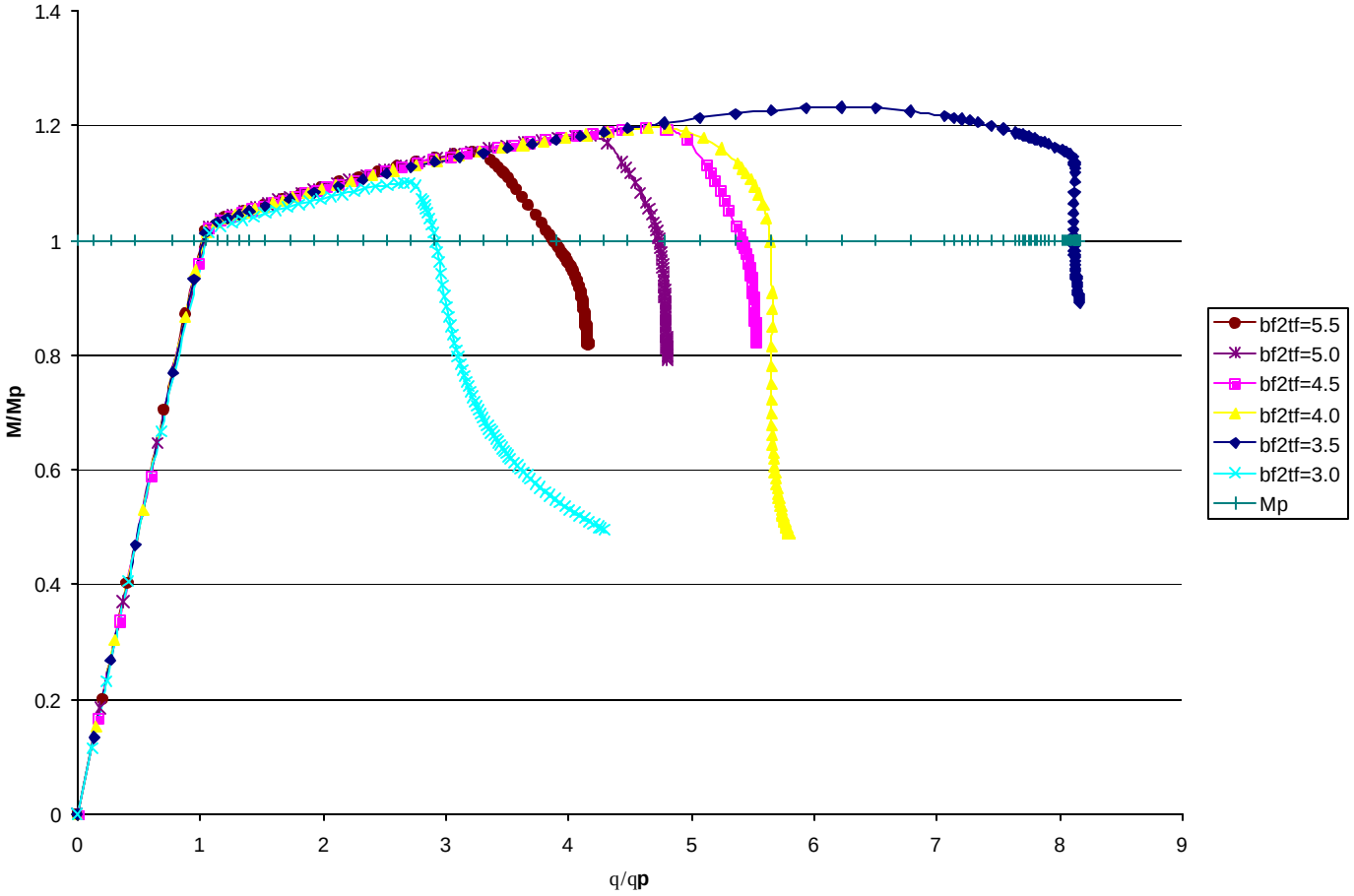

Figure C10 Moment Gradient Response of HPS Hybrid Girder with 344.75 MPa (50 ksi) Web; *d* Bracing

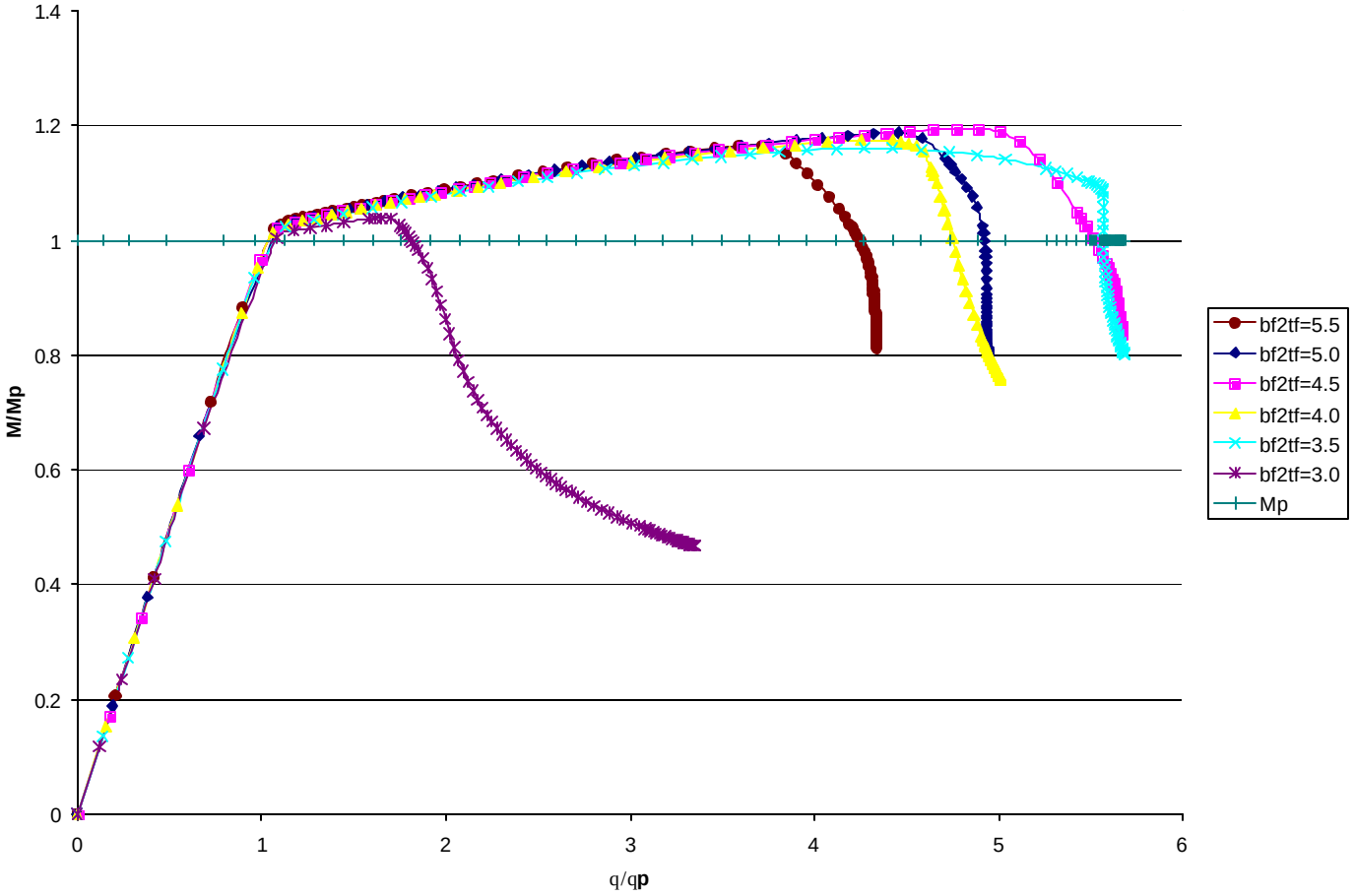

Figure C11 Moment Gradient Response of HPS Hybrid Girder with 275.8 MPa (40 ksi) Web; *d* Bracing

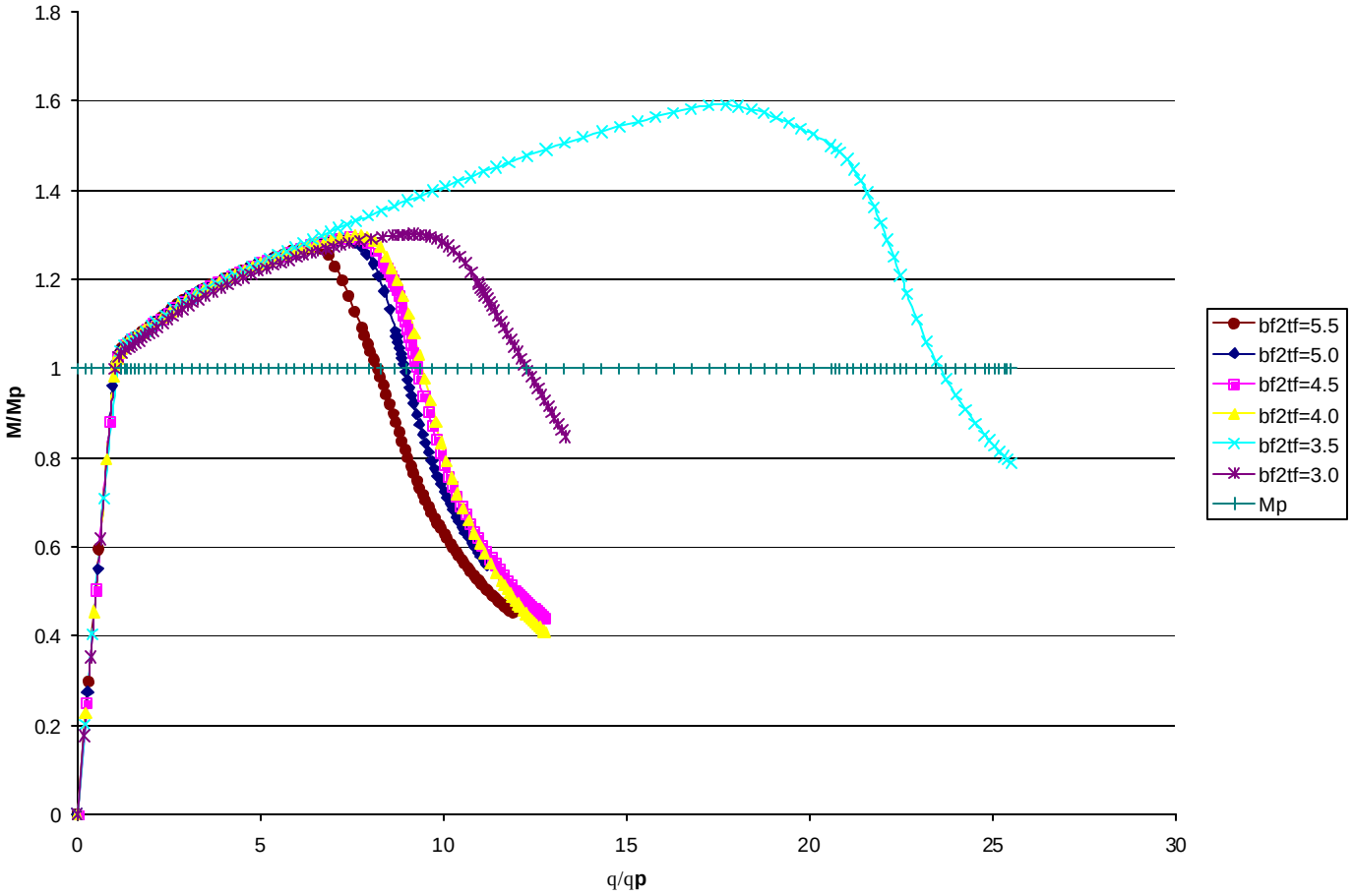

Figure C12 Moment Gradient Response of Homogeneous 344.75 MPa (50 ksi) Girder; *d* Bracing

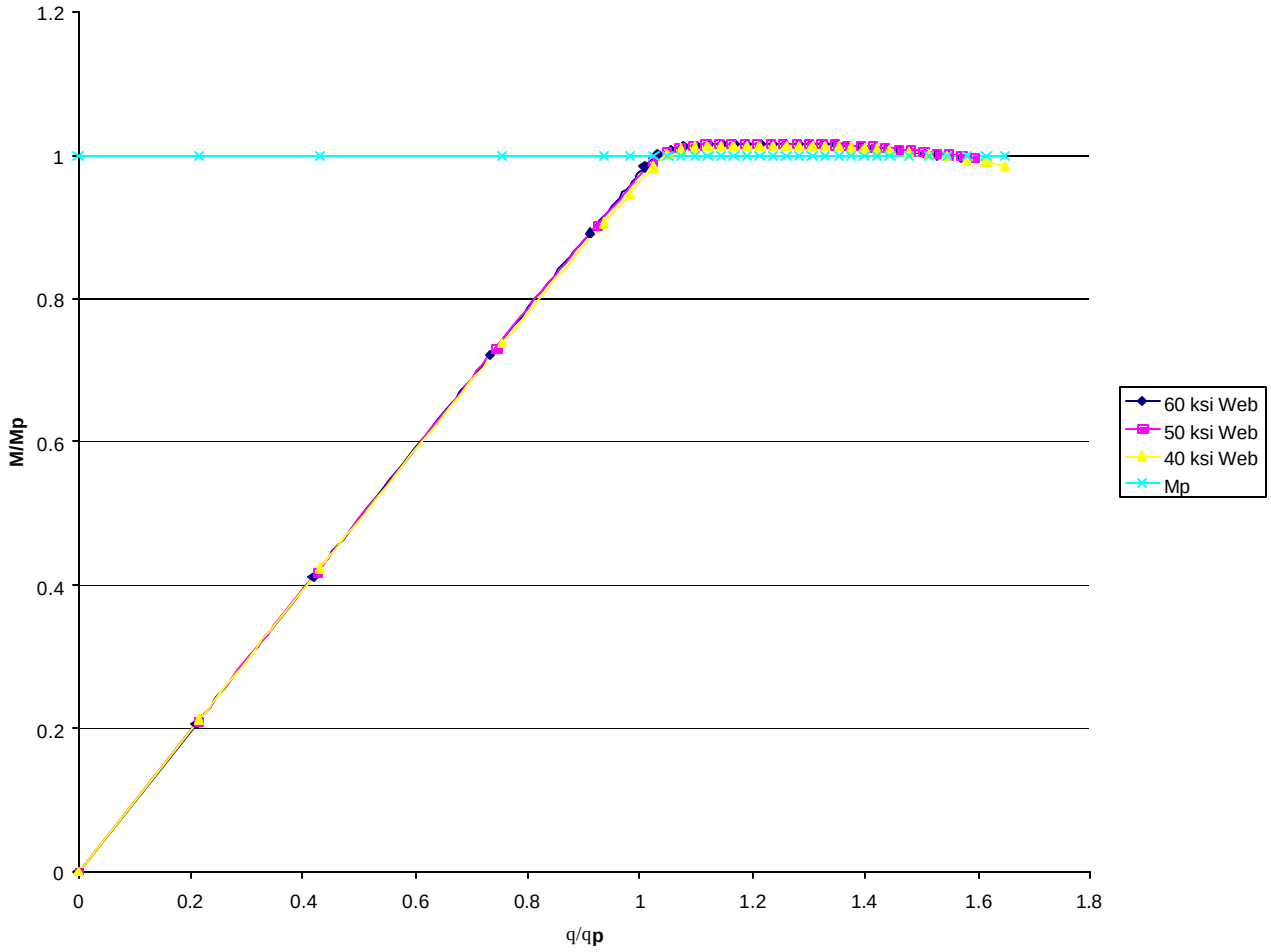

Figure C13 Moment Gradient Response of AASHTO Interaction Equation Case 1

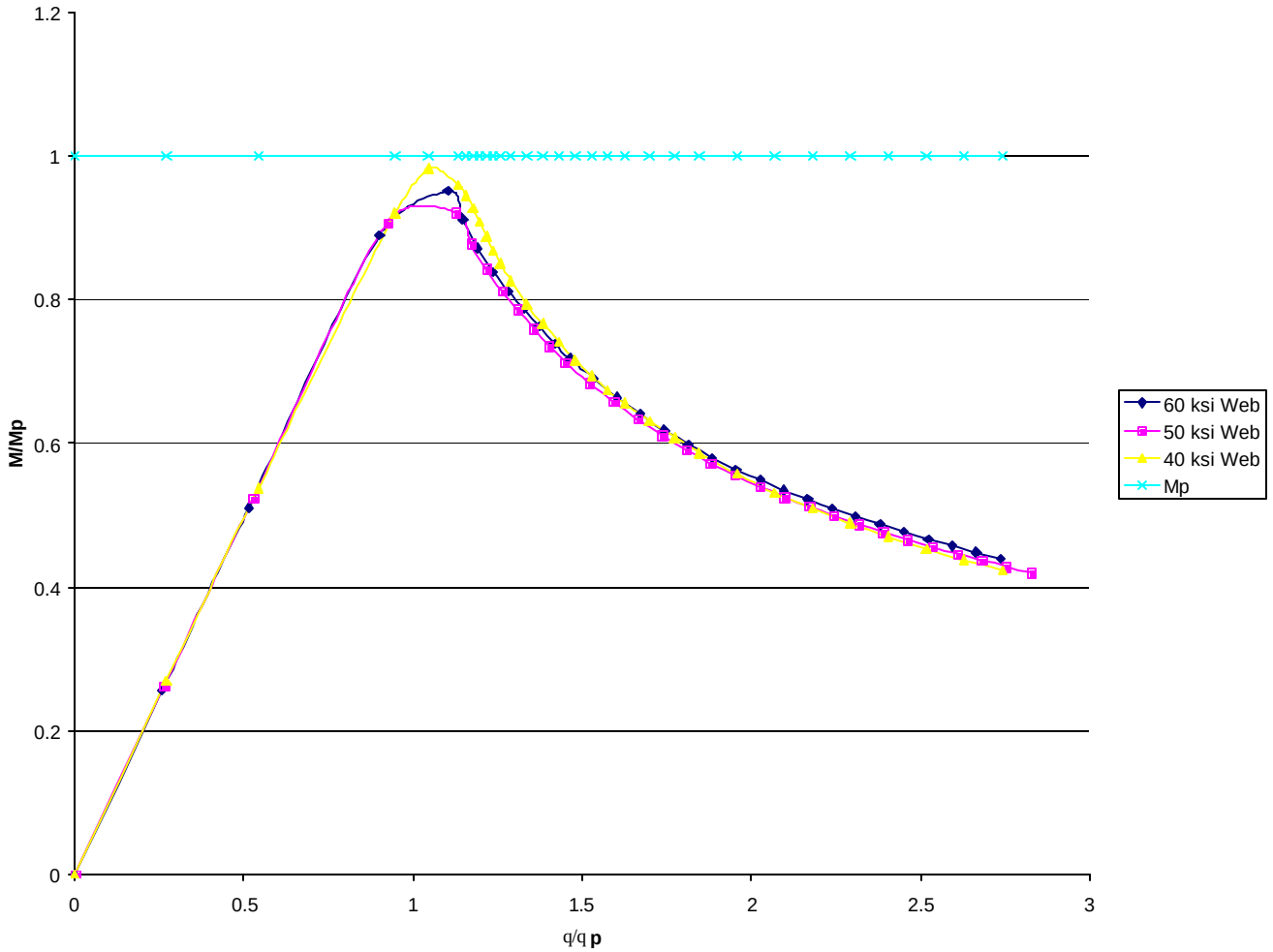

Figure C14 Moment Gradient Response of AASHTO Interaction Equation Case 2

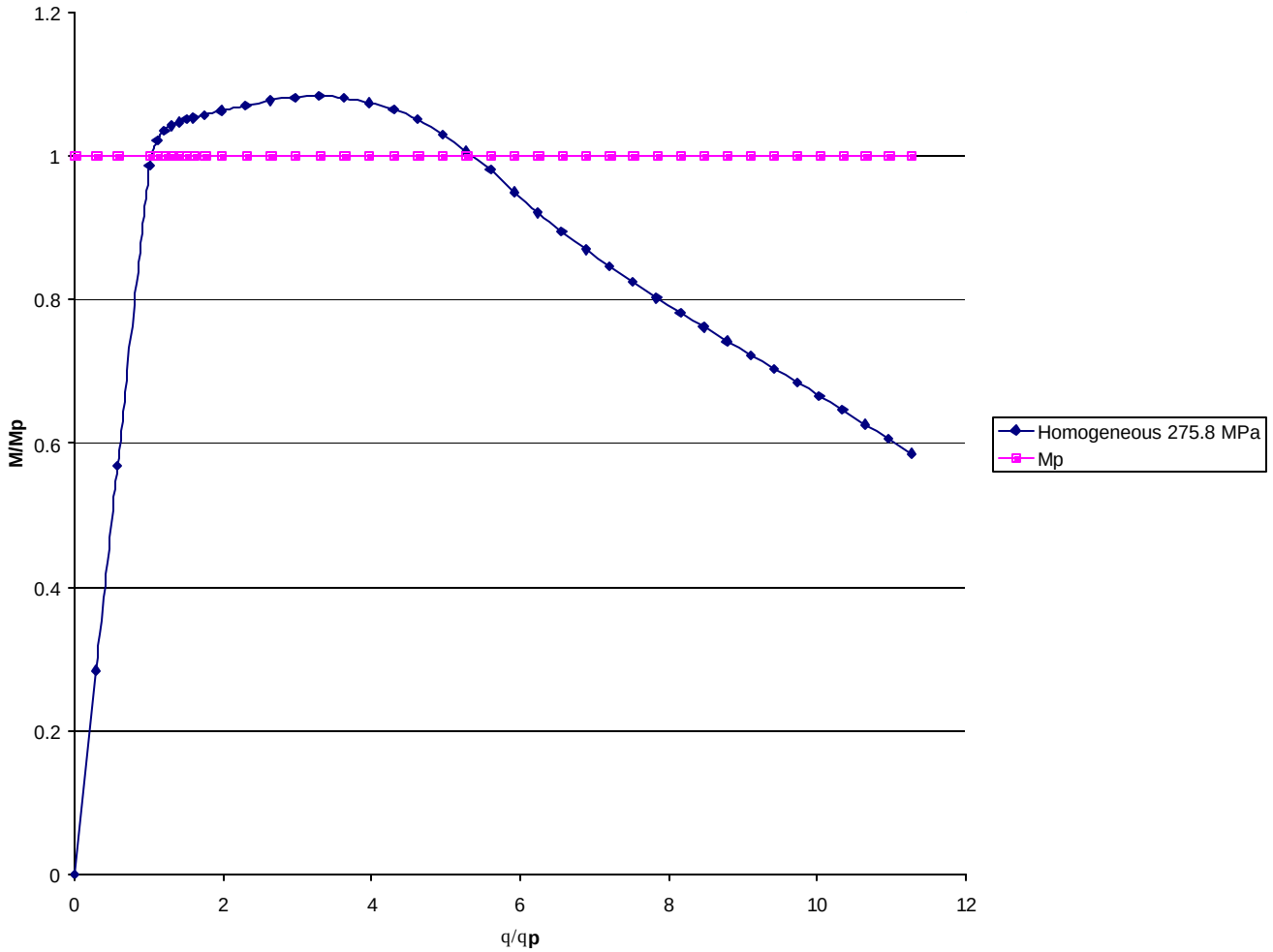

Figure C15 Moment Gradient Response of Homogeneous 275.8 MPa (40 ksi) Girder; AASHTO Bracing, $b_f/2t_f = 4.0$

Table C1 Summary of AASHTO Bracing Rotation Capacity (R) Values

AASHTO BRACING			
	b/2tf	h/tw	R
70F60W	5.0	46.275	0.626339139
	4.5	46.000	0.615777386
	4.0	45.641	0.581460099
	3.5	45.187	0.325193056
	3.0	44.581	0.415329743
	b/2tf	h/tw	R
70F50W	5.0	46.275	0.636464835
	4.5	46.000	0.613493074
	4.0	45.641	0.572788751
	3.5	45.187	0.478075137
	3.0	44.581	0.369794499
	b/2tf	h/tw	R
70F40W	5.0	46.275	0.614677359
	4.5	46.000	0.577393937
	4.0	45.641	0.518952329
	3.5	45.187	0.43435563
	3.0	44.581	0.294015838
	b/2tf	h/tw	R
50F50W	5.0	46.275	2.630835245
	4.5	46.000	2.68608435
	4.0	45.641	2.696848999
	3.5	45.187	2.62758581
	3.0	44.581	2.336094877

Table C2 Summary of *d/2* Bracing Rotation Capacity (R) Values

D/2 BRACING			
	b/2tf	h/tw	R
70F60W	5.0	46.275	2.905386034
	4.5	46.000	3.0354541
	4.0	45.641	3.046818729
	3.5	45.187	3.040141846
	3.0	44.581	2.478437684
	b/2tf	h/tw	R
70F50W	5.0	46.275	2.923789797
	4.5	46.000	3.162422301
	4.0	45.641	3.11231189
	3.5	45.187	3.016181016
	3.0	44.581	2.150757132
	b/2tf	h/tw	R
70F40W	5.0	46.275	3.079304259
	4.5	46.000	3.189747034
	4.0	45.641	3.102477256
	3.5	45.187	2.952373022
	3.0	44.581	1.235415432
	b/2tf	h/tw	R
50F50W	5.0	46.275	5.942105495
	4.5	46.000	6.316686391
	4.0	45.641	6.57529165
	3.5	45.187	6.410050352
	3.0	44.581	5.742310563

Table C3 Summary of *d* Bracing Rotation Capacity (R) Values

D BRACING			
	b/2tf	h/tw	R
70F60W	5.5	46.506	2.335223337
	5.0	46.275	3.530885353
	4.5	46.000	4.212141536
	4.0	45.641	4.622400973
	3.5	45.187	9.798234817
	3.0	44.581	N/A
	b/2tf	h/tw	R
70F50W	5.5	46.506	2.868741724
	5.0	46.275	3.71033871
	4.5	46.000	4.371766695
	4.0	45.641	4.599134939
	3.5	45.187	7.028240925
	3.0	44.581	1.861845339
	b/2tf	h/tw	R
70F40W	5.5	46.506	3.24375485
	5.0	46.275	3.89314204
	4.5	46.000	4.4753828
	4.0	45.641	3.699860691
	3.5	45.187	4.6190594
	3.0	44.581	0.780196997
	b/2tf	h/tw	R
50F50W	5.5	46.506	7.18252381
	5.0	46.275	7.894731806
	4.5	46.000	8.20294768
	4.0	45.641	8.368687487
	3.5	45.187	22.28172724
	3.0	44.581	11.11203481

Table C4 Summary of AASHTO Bracing Rotation Capacity (R) Values

CASE 1	
	R
60 ksi Web	0.510632595
50 ksi Web	0.535615973
40 ksi Web	0.522859398

CASE 2	
	R
60 ksi Web	0
50 ksi Web	0
40 ksi Web	0

AASHTO BRACING			
	bf/2tf	h/tw	R
40F40W	4	45.64	4.294334495

APPENDIX D

Appendix D

D.1 Model Cross-Sectional Properties Calculation Sheets

Excel sheets are generated for each model in order to calculate their respective cross-sectional properties, plastic moment (M_p), and plastic rotation ($?_p$). Figures D1-D34 are the Excel sheets used to calculate these values for each model. The set of figures can be divided into the following categories:

1. HPS flange with 60 ksi web; Figures D2 – D7
2. HPS flange with 50 ksi web; Figures D8 – D13
3. HPS flange with 40 ksi web; Figures D14 – D20
4. Homogeneous 50 ksi girder; Figures D21 – D26
5. Homogeneous 40 ksi girder; Figures D27
6. AASHTO Interaction Case 1; Figures D28 – D30
7. AASHTO Interaction Case 2; Figures D31 – D34

The model's cross section is divided into 4 regions as shown in Figure D1. Each model's dimensions and yield strengths (for each section) are entered into the Excel sheet. The area and resultant forces for each section are calculated from these two sets of values. Once the resultant forces for each section are calculated, M_p is calculated by taking the moment about the model's neutral axis. q_p is calculated using the plastic moment. Table D1 provides a summary of M_p and q_p for each model analyzed.

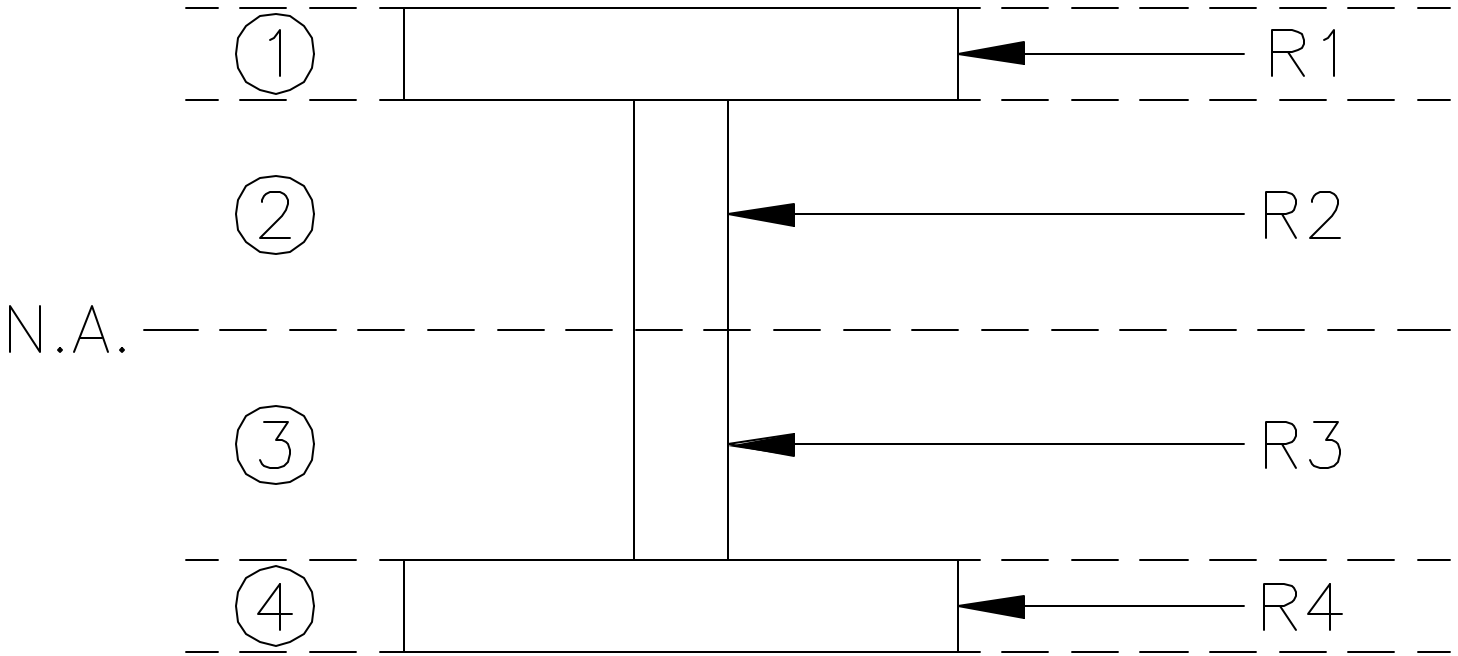

Figure D1 Illustration of Model Divided Into 4 Sections

Enter in the Dimensions of the Beam		
Height =	0.781	m *
Width =	0.406	m
Flange Thickness =	0.03691	m
Web Thickness =	0.016	m
L btw Supports =	15.25	m
A1 =	0.014985	m^2
A2 =	0.005953	m^2
A3 =	0.005953	m^2
A4 =	0.014985	m^2

Calculations of the Resultant Forces		
R1 =	8101552	N
R2 =	2462640	N
R3 =	2462640	N
R4 =	8101552	N

Enter Stresses in the 4 beam Sections (ksi)				
σy1 =	78.411	=	540627500	Pa **
σy2 =	60	=	413700000	Pa
σy3 =	60	=	413700000	Pa
σy4 =	78.411	=	540627500	Pa **

Cross Sectional Properties		
E =	2.00E+11	Pa
Ixx =	0.005122983	m^4
Iyy =	0.000411945	m^4
ry =	0.099182467	m
Sx =	0.012527008	m^3
P =	1899940.966	N
Mp =	7243524.934	Nm
Θp =	0.026952989	

* Height is defined from the centroid of the top flange to the centroid of the bottom flange

** Yield stress value is taken from results of material tests performed on HPS steel used in experimental tests by Azizinamini et al. (1999)

Figure D2 Calculation Sheet for HPS Hybrid Girder with 60 ksi Web, $b_f/2t_f = 5.5$

Enter in the Dimensions of the Beam		
Height =	0.781	m *
Width =	0.406	m
Flange Thickness =	0.0406	m
Web Thickness =	0.016	m
L btw Supports =	15.25	m
A1 =	0.016484	m^2
A2 =	0.005923	m^2
A3 =	0.005923	m^2
A4 =	0.016484	m^2

Calculations of the Resultant Forces		
R1 =	8911487	N
R2 =	2450428	N
R3 =	2450428	N
R4 =	8911487	N

Enter Stresses in the 4 beam Sections (ksi)				
σy1 =	78.411	=	540627500	Pa **
σy2 =	60	=	413700000	Pa
σy3 =	60	=	413700000	Pa
σy4 =	78.411	=	540627500	Pa **

Cross Sectional Properties		
E =	2.00E+11	Pa
Ixx =	0.00557288	m^4
Iyy =	0.000453101	m^4
ry =	0.100552454	m
Sx =	0.013565921	m^3
P =	2063480.68	N
Mp =	7867020.092	Nm
Θp =	0.026909795	

* Height is defined from the centroid of the top flange to the centroid of the bottom flange

** Yield stress value is taken from results of material tests performed on HPS steel used in experimental tests by Azizinamini et al. (1999)

Figure D3 Calculation Sheet for HPS Hybrid Girder with 60 ksi Web, $b_f/2t_f = 5.0$

Enter in the Dimensions of the Beam		
Height =	0.781	m *
Width =	0.406	m
Flange Thickness =	0.045	m
Web Thickness =	0.016	m
L btw Supports =	15.25	m
A1 =	0.01827	m^2
A2 =	0.005888	m^2
A3 =	0.005888	m^2
A4 =	0.01827	m^2

Calculations of the Resultant Forces		
R1 =	9877264	N
R2 =	2435866	N
R3 =	2435866	N
R4 =	9877264	N

Enter Stresses in the 4 beam Sections (ksi)				
σy1 =	78.411	=	540627500	Pa **
σy2 =	60	=	413700000	Pa
σy3 =	60	=	413700000	Pa
σy4 =	78.411	=	540627500	Pa **

Cross Sectional Properties		
E =	2.00E+11	Pa
Ixx =	0.006109744	m^4
Iyy =	0.000502177	m^4
ry =	0.101948973	m
Sx =	0.014793569	m^3
P =	2258502.835	N
Mp =	8610542.057	Nm
Θp =	0.026865029	

* Height is defined from the centroid of the top flange to the centroid of the bottom flange

** Yield stress value is taken from results of material tests performed on HPS steel used in experimental tests by Azizinamini et al. (1999)

Figure D4 Calculation Sheet for HPS Hybrid Girder with 60 ksi Web, $b_f/2t_f = 4.5$

Enter in the Dimensions of the Beam		
Height =	0.781	m *
Width =	0.406	m
Flange Thickness =	0.05075	m
Web Thickness =	0.016	m
L btw Supports =	15.25	m
A1 =	0.020605	m^2
A2 =	0.005842	m^2
A3 =	0.005842	m^2
A4 =	0.020605	m^2

Calculations of the Resultant Forces		
R1 =	11139359	N
R2 =	2416835	N
R3 =	2416835	N
R4 =	11139359	N

Enter Stresses in the 4 beam Sections (ksi)				
σy1 =	78.411	=	540627500	Pa **
σy2 =	60	=	413700000	Pa
σy3 =	60	=	413700000	Pa
σy4 =	78.411	=	540627500	Pa **

Cross Sectional Properties		
E =	2.00E+11	Pa
Ixx =	0.006812038	m^4
Iyy =	0.00056631	m^4
ry =	0.103473216	m
Sx =	0.016380013	m^3
P =	2513386.664	N
Mp =	9582286.657	Nm
Θp =	0.02681464	

* Height is defined from the centroid of the top flange to the centroid of the bottom flange

** Yield stress value is taken from results of material tests performed on HPS steel used in experimental tests by Azizinamini et al. (1999)

Figure D5 Calculation Sheet for HPS Hybrid Girder with 60 ksi Web, $b_f/2t_f = 4.0$

Enter in the Dimensions of the Beam		
Height =	0.781	m *
Width =	0.406	m
Flange Thickness =	0.058	m
Web Thickness =	0.016	m
L btw Supports =	15.25	m
A1 =	0.023548	m^2
A2 =	0.005784	m^2
A3 =	0.005784	m^2
A4 =	0.023548	m^2

Calculations of the Resultant Forces		
R1 =	12730696	N
R2 =	2392841	N
R3 =	2392841	N
R4 =	12730696	N

Enter Stresses in the 4 beam Sections (ksi)				
σy1 =	78.411	=	540627500	Pa **
σy2 =	60	=	413700000	Pa
σy3 =	60	=	413700000	Pa
σy4 =	78.411	=	540627500	Pa **

Cross Sectional Properties		
E =	2.00E+11	Pa
Ixx =	0.007698794	m^4
Iyy =	0.000647173	m^4
ry =	0.10503267	m
Sx =	0.01835231	m^3
P =	2834802.837	N
Mp =	10807685.81	Nm
Θp =	0.026760231	

* Height is defined from the centroid of the top flange to the centroid of the bottom flange

** Yield stress value is taken from results of material tests performed on HPS steel used in experimental tests by Azizinamini et al. (1999)

Figure D6 Calculation Sheet for HPS Hybrid Girder with 60 ksi Web, $b_f/2t_f = 3.5$

Enter in the Dimensions of the Beam		
Height =	0.781	m *
Width =	0.406	m
Flange Thickness =	0.0677	m
Web Thickness =	0.016	m
L btw Supports =	15.25	m
A1 =	0.027486	m^2
A2 =	0.005706	m^2
A3 =	0.005706	m^2
A4 =	0.027486	m^2

Calculations of the Resultant Forces		
R1 =	14859796	N
R2 =	2360738	N
R3 =	2360738	N
R4 =	14859796	N

Enter Stresses in the 4 beam Sections (ksi)				
σy1 =	78.411	=	540627500	Pa **
σy2 =	60	=	413700000	Pa
σy3 =	60	=	413700000	Pa
σy4 =	78.411	=	540627500	Pa **

Cross Sectional Properties		
E =	2.00E+11	Pa
Ixx =	0.008887651	m^4
Iyy =	0.000755363	m^4
ry =	0.106669959	m
Sx =	0.020944152	m^3
P =	3264906.872	N
Mp =	12447457.45	Nm
Θp =	0.02669768	

* Height is defined from the centroid of the top flange to the centroid of the bottom flange

** Yield stress value is taken from results of material tests performed on HPS steel used in experimental tests by Azizinamini et al. (1999)

Figure D7 Calculation Sheet for HPS Hybrid Girder with 60 ksi Web, $b_f/2t_f = 3.0$

Enter in the Dimensions of the Beam		
Height =	0.781	m *
Width =	0.406	m
Flange Thickness =	0.03691	m
Web Thickness =	0.016	m
L btw Supports =	15.25	m
A1 =	0.014985	m^2
A2 =	0.005953	m^2
A3 =	0.005953	m^2
A4 =	0.014985	m^2

Calculations of the Resultant Forces		
R1 =	8101552	N
R2 =	2052200	N
R3 =	2052200	N
R4 =	8101552	N

Enter Stresses in the 4 beam Sections (ksi)				
σy1 =	78.411	=	540627500	Pa **
σy2 =	50	=	344750000	Pa
σy3 =	50	=	344750000	Pa
σy4 =	78.411	=	540627500	Pa **

Cross Sectional Properties		
E =	2.00E+11	Pa
Ixx =	0.005122983	m^4
Iyy =	0.000411945	m^4
ry =	0.099182467	m
Sx =	0.012527008	m^3
P =	1859887.939	N
Mp =	7090822.768	Nm
Θp =	0.026384788	

* Height is defined from the centroid of the top flange to the centroid of the bottom flange

** Yield stress value is taken from results of material tests performed on HPS steel used in experimental tests by Azizinamini et al. (1999)

Figure D8 Calculation Sheet for HPS Hybrid Girder with 50 ksi Web, $b_f/2t_f = 5.5$

Enter in the Dimensions of the Beam		
Height =	0.781	m *
Width =	0.406	m
Flange Thickness =	0.0406	m
Web Thickness =	0.016	m
L btw Supports =	15.25	m
A1 =	0.016484	m^2
A2 =	0.005923	m^2
A3 =	0.005923	m^2
A4 =	0.016484	m^2

Calculations of the Resultant Forces		
R1 =	8911487	N
R2 =	2042023	N
R3 =	2042023	N
R4 =	8911487	N

Enter Stresses in the 4 beam Sections (ksi)				
σy1 =	78.411	=	540627500	Pa **
σy2 =	50	=	344750000	Pa
σy3 =	50	=	344750000	Pa
σy4 =	78.411	=	540627500	Pa **

Cross Sectional Properties		
E =	2.00E+11	Pa
Ixx =	0.00557288	m^4
Iyy =	0.000453101	m^4
ry =	0.100552454	m
Sx =	0.013565921	m^3
P =	2023823.92	N
Mp =	7715828.694	Nm
Θp =	0.026392633	

* Height is defined from the centroid of the top flange to the centroid of the bottom flange

** Yield stress value is taken from results of material tests performed on HPS steel used in experimental tests by Azizinamini et al. (1999)

Figure D9 Calculation Sheet for HPS Hybrid Girder with 50 ksi Web, $b_f/2t_f = 5.0$

Enter in the Dimensions of the Beam		
Height =	0.781	m *
Width =	0.406	m
Flange Thickness =	0.045	m
Web Thickness =	0.016	m
L btw Supports =	15.25	m
A1 =	0.01827	m^2
A2 =	0.005888	m^2
A3 =	0.005888	m^2
A4 =	0.01827	m^2

Calculations of the Resultant Forces		
R1 =	9877264	N
R2 =	2029888	N
R3 =	2029888	N
R4 =	9877264	N

Enter Stresses in the 4 beam Sections (ksi)				
σy1 =	78.411	=	540627500	Pa **
σy2 =	50	=	344750000	Pa
σy3 =	50	=	344750000	Pa
σy4 =	78.411	=	540627500	Pa **

Cross Sectional Properties		
E =	2.00E+11	Pa
Ixx =	0.006109744	m^4
Iyy =	0.000502177	m^4
ry =	0.101948973	m
Sx =	0.014793569	m^3
P =	2219316.013	N
Mp =	8461142.3	Nm
Θp =	0.0263989	

* Height is defined from the centroid of the top flange to the centroid of the bottom flange

** Yield stress value is taken from results of material tests performed on HPS steel used in experimental tests by Azizinamini et al. (1999)

Figure D10 Calculation Sheet for HPS Hybrid Girder with 50 ksi Web, $b_f/2t_f = 4.5$

Enter in the Dimensions of the Beam		
Height =	0.781	m *
Width =	0.406	m
Flange Thickness =	0.05075	m
Web Thickness =	0.016	m
L btw Supports =	15.25	m
A1 =	0.020605	m^2
A2 =	0.005842	m^2
A3 =	0.005842	m^2
A4 =	0.020605	m^2

Calculations of the Resultant Forces		
R1 =	11139359	N
R2 =	2014030	N
R3 =	2014030	N
R4 =	11139359	N

Enter Stresses in the 4 beam Sections (ksi)				
σy1 =	78.411	=	540627500	Pa **
σy2 =	50	=	344750000	Pa
σy3 =	50	=	344750000	Pa
σy4 =	78.411	=	540627500	Pa **

Cross Sectional Properties		
E =	2.00E+11	Pa
Ixx =	0.006812038	m^4
Iyy =	0.00056631	m^4
ry =	0.103473216	m
Sx =	0.016380013	m^3
P =	2474809.745	N
Mp =	9435212.153	Nm
Θp =	0.026403073	

* Height is defined from the centroid of the top flange to the centroid of the bottom flange

** Yield stress value is taken from results of material tests performed on HPS steel used in experimental tests by Azizinamini et al. (1999)

Figure D11 Calculation Sheet for HPS Hybrid Girder with 50 ksi Web, $b_f/2t_f = 4.0$

Enter in the Dimensions of the Beam		
Height =	0.781	m *
Width =	0.406	m
Flange Thickness =	0.058	m
Web Thickness =	0.016	m
L btw Supports =	15.25	m
A1 =	0.023548	m^2
A2 =	0.005784	m^2
A3 =	0.005784	m^2
A4 =	0.023548	m^2

Calculations of the Resultant Forces		
R1 =	12730696	N
R2 =	1994034	N
R3 =	1994034	N
R4 =	12730696	N

Enter Stresses in the 4 beam Sections (ksi)				
σy1 =	78.411	=	540627500	Pa **
σy2 =	50	=	344750000	Pa
σy3 =	50	=	344750000	Pa
σy4 =	78.411	=	540627500	Pa **

Cross Sectional Properties		
E =	2.00E+11	Pa
Ixx =	0.007698794	m^4
Iyy =	0.000647173	m^4
ry =	0.10503267	m
Sx =	0.01835231	m^3
P =	2796988.106	N
Mp =	10663517.16	Nm
Θp =	0.026403264	

* Height is defined from the centroid of the top flange to the centroid of the bottom flange

** Yield stress value is taken from results of material tests performed on HPS steel used in experimental tests by Azizinamini et al. (1999)

Figure D12 Calculation Sheet for HPS Hybrid Girder with 50 ksi Web, $b_f/2t_f = 3.5$

Enter in the Dimensions of the Beam		
Height =	0.781	m *
Width =	0.406	m
Flange Thickness =	0.0677	m
Web Thickness =	0.016	m
L btw Supports =	15.25	m
A1 =	0.027486	m^2
A2 =	0.005706	m^2
A3 =	0.005706	m^2
A4 =	0.027486	m^2

Calculations of the Resultant Forces		
R1 =	14859796	N
R2 =	1967281	N
R3 =	1967281	N
R4 =	14859796	N

Enter Stresses in the 4 beam Sections (ksi)				
σy1 =	78.411	=	540627500	Pa **
σy2 =	50	=	344750000	Pa
σy3 =	50	=	344750000	Pa
σy4 =	78.411	=	540627500	Pa **

Cross Sectional Properties		
E =	2.00E+11	Pa
Ixx =	0.008887651	m^4
Iyy =	0.000755363	m^4
ry =	0.106669959	m
Sx =	0.020944152	m^3
P =	3228100.005	N
Mp =	12307131.27	Nm
Θp =	0.026396704	

* Height is defined from the centroid of the top flange to the centroid of the bottom flange

** Yield stress value is taken from results of material tests performed on HPS steel used in experimental tests by Azizinamini et al. (1999)

Figure D13 Calculation Sheet for HPS Hybrid Girder with 50 ksi Web, $b_f/2t_f = 3.0$

Enter in the Dimensions of the Beam		
Height =	0.781	m *
Width =	0.406	m
Flange Thickness =	0.03691	m
Web Thickness =	0.016	m
L btw Supports =	15.25	m
A1 =	0.014985	m^2
A2 =	0.005953	m^2
A3 =	0.005953	m^2
A4 =	0.014985	m^2

Calculations of the Resultant Forces		
R1 =	8101552	N
R2 =	1641760	N
R3 =	1641760	N
R4 =	8101552	N

Enter Stresses in the 4 beam Sections (ksi)				
σy1 =	78.411	=	540627500	Pa **
σy2 =	40	=	275800000	Pa
σy3 =	40	=	275800000	Pa
σy4 =	78.411	=	540627500	Pa **

Cross Sectional Properties		
E =	2.00E+11	Pa
Ixx =	0.005122983	m^4
Iyy =	0.000411945	m^4
ry =	0.099182467	m
Sx =	0.012527008	m^3
P =	1819834.912	N
Mp =	6938120.602	Nm
Θp =	0.025816586	

* Height is defined from the centroid of the top flange to the centroid of the bottom flange

** Yield stress value is taken from results of material tests performed on HPS steel used in experimental tests by Azizinamini et al. (1999)

Figure D14 Calculation Sheet for HPS Hybrid Girder with 40 ksi Web, $b_f/2t_f = 5.5$

Enter in the Dimensions of the Beam		
Height =	0.781	m *
Width =	0.406	m
Flange Thickness =	0.0406	m
Web Thickness =	0.016	m
L btw Supports =	15.25	m
A1 =	0.016484	m^2
A2 =	0.005923	m^2
A3 =	0.005923	m^2
A4 =	0.016484	m^2

Calculations of the Resultant Forces		
R1 =	8911487	N
R2 =	1633619	N
R3 =	1633619	N
R4 =	8911487	N

Enter Stresses in the 4 beam Sections (ksi)				
σy1 =	78.411	=	540627500	Pa **
σy2 =	40	=	275800000	Pa
σy3 =	40	=	275800000	Pa
σy4 =	78.411	=	540627500	Pa **

Cross Sectional Properties		
E =	2.00E+11	Pa
Ixx =	0.00557288	m^4
Iyy =	0.000453101	m^4
ry =	0.100552454	m
Sx =	0.013565921	m^3
P =	1984167.16	N
Mp =	7564637.296	Nm
Θp =	0.02587547	

* Height is defined from the centroid of the top flange to the centroid of the bottom flange

** Yield stress value is taken from results of material tests performed on HPS steel used in experimental tests by Azizinamini et al. (1999)

Figure D15 Calculation Sheet for HPS Hybrid Girder with 40 ksi Web, $b_f/2t_f = 5.0$

Enter in the Dimensions of the Beam		
Height =	0.781	m *
Width =	0.406	m
Flange Thickness =	0.045	m
Web Thickness =	0.016	m
L btw Supports =	15.25	m
A1 =	0.01827	m^2
A2 =	0.005888	m^2
A3 =	0.005888	m^2
A4 =	0.01827	m^2

Calculations of the Resultant Forces		
R1 =	9877264	N
R2 =	1623910	N
R3 =	1623910	N
R4 =	9877264	N

Enter Stresses in the 4 beam Sections (ksi)				
σy1 =	78.411	=	540627500	Pa **
σy2 =	40	=	275800000	Pa
σy3 =	40	=	275800000	Pa
σy4 =	78.411	=	540627500	Pa **

Cross Sectional Properties		
E =	2.00E+11	Pa
Ixx =	0.006109744	m^4
Iyy =	0.000502177	m^4
ry =	0.101948973	m
Sx =	0.014793569	m^3
P =	2180129.192	N
Mp =	8311742.543	Nm
Θp =	0.02593277	

* Height is defined from the centroid of the top flange to the centroid of the bottom flange

** Yield stress value is taken from results of material tests performed on HPS steel used in experimental tests by Azizinamini et al. (1999)

Figure D16 Calculation Sheet for HPS Hybrid Girder with 40 ksi Web, $b_f/2t_f = 4.5$

Enter in the Dimensions of the Beam		
Height =	0.781	m *
Width =	0.406	m
Flange Thickness =	0.05075	m
Web Thickness =	0.016	m
L btw Supports =	15.25	m
A1 =	0.020605	m^2
A2 =	0.005842	m^2
A3 =	0.005842	m^2
A4 =	0.020605	m^2

Calculations of the Resultant Forces		
R1 =	11139359	N
R2 =	1611224	N
R3 =	1611224	N
R4 =	11139359	N

Enter Stresses in the 4 beam Sections (ksi)				
σy1 =	78.411	=	540627500	Pa **
σy2 =	40	=	275800000	Pa
σy3 =	40	=	275800000	Pa
σy4 =	78.411	=	540627500	Pa **

Cross Sectional Properties		
E =	2.00E+11	Pa
Ixx =	0.006812038	m^4
Iyy =	0.00056631	m^4
ry =	0.103473216	m
Sx =	0.016380013	m^3
P =	2436232.826	N
Mp =	9288137.649	Nm
Θp =	0.025991506	

* Height is defined from the centroid of the top flange to the centroid of the bottom flange

** Yield stress value is taken from results of material tests performed on HPS steel used in experimental tests by Azizinamini et al. (1999)

Figure D17 Calculation Sheet for HPS Hybrid Girder with 40 ksi Web, $b_f/2t_f = 4.0$

Enter in the Dimensions of the Beam		
Height =	0.781	m *
Width =	0.406	m
Flange Thickness =	0.058	m
Web Thickness =	0.016	m
L btw Supports =	15.25	m
A1 =	0.023548	m^2
A2 =	0.005784	m^2
A3 =	0.005784	m^2
A4 =	0.023548	m^2

Calculations of the Resultant Forces		
R1 =	12730696	N
R2 =	1595227	N
R3 =	1595227	N
R4 =	12730696	N

Enter Stresses in the 4 beam Sections (ksi)				
σy1 =	78.411	=	540627500	Pa **
σy2 =	40	=	275800000	Pa
σy3 =	40	=	275800000	Pa
σy4 =	78.411	=	540627500	Pa **

Cross Sectional Properties		
E =	2.00E+11	Pa
Ixx =	0.007698794	m^4
Iyy =	0.000647173	m^4
ry =	0.10503267	m
Sx =	0.01835231	m^3
P =	2759173.376	N
Mp =	10519348.5	Nm
Θp =	0.026046297	

* Height is defined from the centroid of the top flange to the centroid of the bottom flange

** Yield stress value is taken from results of material tests performed on HPS steel used in experimental tests by Azizinamini et al. (1999)

Figure D18 Calculation Sheet for HPS Hybrid Girder with 40 ksi Web, $b_f/2t_f = 3.5$

Enter in the Dimensions of the Beam		
Height =	0.781	m *
Width =	0.406	m
Flange Thickness =	0.0677	m
Web Thickness =	0.016	m
L btw Supports =	15.25	m
A1 =	0.027486	m^2
A2 =	0.005706	m^2
A3 =	0.005706	m^2
A4 =	0.027486	m^2

Calculations of the Resultant Forces		
R1 =	14859796	N
R2 =	1573825	N
R3 =	1573825	N
R4 =	14859796	N

Enter Stresses in the 4 beam Sections (ksi)				
σy1 =	78.411	=	540627500	Pa **
σy2 =	40	=	275800000	Pa
σy3 =	40	=	275800000	Pa
σy4 =	78.411	=	540627500	Pa **

Cross Sectional Properties		
E =	2.00E+11	Pa
Ixx =	0.008887651	m^4
Iyy =	0.000755363	m^4
ry =	0.106669959	m
Sx =	0.020944152	m^3
P =	3191293.137	N
Mp =	12166805.09	Nm
Θp =	0.026095728	

* Height is defined from the centroid of the top flange to the centroid of the bottom flange

** Yield stress value is taken from results of material tests performed on HPS steel used in experimental tests by Azizinamini et al. (1999)

Figure D19 Calculation Sheet for HPS Hybrid Girder with 40 ksi Web, $b_f/2t_f = 3.0$

Enter in the Dimensions of the Beam		
Height =	0.781	m *
Width =	0.406	m
Flange Thickness =	0.03691	m
Web Thickness =	0.016	m
L btw Supports =	15.25	m
A1 =	0.014985	m^2
A2 =	0.005953	m^2
A3 =	0.005953	m^2
A4 =	0.014985	m^2

Calculations of the Resultant Forces		
R1 =	5166237	N
R2 =	2052200	N
R3 =	2052200	N
R4 =	5166237	N

Enter Stresses in the 4 beam Sections (ksi)				
σy1 =	50	=	344750000	Pa
σy2 =	50	=	344750000	Pa
σy3 =	50	=	344750000	Pa
σy4 =	50	=	344750000	Pa

Cross Sectional Properties		
E =	2.00E+11	Pa
Ixx =	0.005122983	m^4
Iyy =	0.000411945	m^4
ry =	0.099182467	m
Sx =	0.012527008	m^3
P =	1258581.558	N
Mp =	4798342.189	Nm
Θp =	0.01785452	

* Height is defined from the centroid of the top flange to the centroid of the bottom flange

Figure D20 Calculation Sheet for Homogeneous 50 ksi Girder, $b_f/2t_f = 5.5$

Enter in the Dimensions of the Beam		
Height =	0.781	m *
Width =	0.406	m
Flange Thickness =	0.0406	m
Web Thickness =	0.016	m
L btw Supports =	15.25	m
A1 =	0.016484	m^2
A2 =	0.005923	m^2
A3 =	0.005923	m^2
A4 =	0.016484	m^2

Calculations of the Resultant Forces		
R1 =	5682721	N
R2 =	2042023	N
R3 =	2042023	N
R4 =	5682721	N

Enter Stresses in the 4 beam Sections (ksi)				
σy1 =	50	=	344750000	Pa
σy2 =	50	=	344750000	Pa
σy3 =	50	=	344750000	Pa
σy4 =	50	=	344750000	Pa

Cross Sectional Properties		
E =	2.00E+11	Pa
Ixx =	0.00557288	m^4
Iyy =	0.000453101	m^4
ry =	0.100552454	m
Sx =	0.013565921	m^3
P =	1362403.192	N
Mp =	5194162.168	Nm
Θp =	0.017767063	

* Height is defined from the centroid of the top flange to the centroid of the bottom flange

Figure D21 Calculation Sheet for Homogeneous 50 ksi Girder, $b_f/2t_f = 5.0$

Enter in the Dimensions of the Beam		
Height =	0.781	m *
Width =	0.406	m
Flange Thickness =	0.045	m
Web Thickness =	0.016	m
L btw Supports =	15.25	m
A1 =	0.01827	m^2
A2 =	0.005888	m^2
A3 =	0.005888	m^2
A4 =	0.01827	m^2

Calculations of the Resultant Forces		
R1 =	6298583	N
R2 =	2029888	N
R3 =	2029888	N
R4 =	6298583	N

Enter Stresses in the 4 beam Sections (ksi)				
σy1 =	50	=	344750000	Pa
σy2 =	50	=	344750000	Pa
σy3 =	50	=	344750000	Pa
σy4 =	50	=	344750000	Pa

Cross Sectional Properties		
E =	2.00E+11	Pa
Ixx =	0.006109744	m^4
Iyy =	0.000502177	m^4
ry =	0.101948973	m
Sx =	0.014793569	m^3
P =	1486214.221	N
Mp =	5666191.717	Nm
Θp =	0.017678609	

* Height is defined from the centroid of the top flange to the centroid of the bottom flange

Figure D22 Calculation Sheet for Homogeneous 50 ksi Girder, $b_f/2t_f = 4.5$

Enter in the Dimensions of the Beam		
Height =	0.781	m *
Width =	0.406	m
Flange Thickness =	0.05075	m
Web Thickness =	0.016	m
L btw Supports =	15.25	m
A1 =	0.020605	m^2
A2 =	0.005842	m^2
A3 =	0.005842	m^2
A4 =	0.020605	m^2

Calculations of the Resultant Forces		
R1 =	7103401	N
R2 =	2014030	N
R3 =	2014030	N
R4 =	7103401	N

Enter Stresses in the 4 beam Sections (ksi)				
$\sigma y1$ =	50	=	344750000	Pa
$\sigma y2$ =	50	=	344750000	Pa
$\sigma y3$ =	50	=	344750000	Pa
$\sigma y4$ =	50	=	344750000	Pa

Cross Sectional Properties		
E =	2.00E+11	Pa
Ixx =	0.006812038	m^4
Iyy =	0.00056631	m^4
ry =	0.103473216	m
Sx =	0.016380013	m^3
P =	1648033.835	N
Mp =	6283128.995	Nm
Θp =	0.017582425	

* Height is defined from the centroid of the top flange to the centroid of the bottom flange

Figure D23 Calculation Sheet for Homogeneous 50 ksi Girder, $b_f/2t_f = 4.0$

Enter in the Dimensions of the Beam		
Height =	0.781	m *
Width =	0.406	m
Flange Thickness =	0.0677	m
Web Thickness =	0.016	m
L btw Supports =	15.25	m
A1 =	0.027486	m^2
A2 =	0.005706	m^2
A3 =	0.005706	m^2
A4 =	0.027486	m^2

Calculations of the Resultant Forces		
R1 =	9475867	N
R2 =	1967281	N
R3 =	1967281	N
R4 =	9475867	N

Enter Stresses in the 4 beam Sections (ksi)			
σy1 =	50	=	344750000 Pa
σy2 =	50	=	344750000 Pa
σy3 =	50	=	344750000 Pa
σy4 =	50	=	344750000 Pa

Cross Sectional Properties		
E =	2.00E+11	Pa
Ixx =	0.008887651	m^4
Iyy =	0.000755363	m^4
ry =	0.106669959	m
Sx =	0.020944152	m^3
P =	2125189.086	N
Mp =	8102283.39	Nm
Θp =	0.01737802	

* Height is defined from the centroid of the top flange to the centroid of the bottom flange

Figure D24 Calculation Sheet for Homogeneous 50 ksi Girder, $b_f/2t_f = 3.5$

Enter in the Dimensions of the Beam		
Height =	0.781	m *
Width =	0.406	m
Flange Thickness =	0.0677	m
Web Thickness =	0.016	m
L btw Supports =	15.25	m
A1 =	0.027486	m^2
A2 =	0.005706	m^2
A3 =	0.005706	m^2
A4 =	0.027486	m^2

Calculations of the Resultant Forces		
R1 =	9475867	N
R2 =	1967281	N
R3 =	1967281	N
R4 =	9475867	N

Enter Stresses in the 4 beam Sections (ksi)			
σy1 =	50	=	344750000 Pa
σy2 =	50	=	344750000 Pa
σy3 =	50	=	344750000 Pa
σy4 =	50	=	344750000 Pa

Cross Sectional Properties		
E =	2.00E+11	Pa
Ixx =	0.008887651	m^4
Iyy =	0.000755363	m^4
ry =	0.106669959	m
Sx =	0.020944152	m^3
P =	2125189.086	N
Mp =	8102283.39	Nm
Θp =	0.01737802	

* Height is defined from the centroid of the top flange to the centroid of the bottom flange

Figure D25 Calculation Sheet for Homogeneous 50 ksi Girder, $b_f/2t_f = 3.0$

Enter in the Dimensions of the Beam		
Height =	0.781	m *
Width =	0.406	m
Flange Thickness =	0.05075	m
Web Thickness =	0.016	m
L btw Supports =	15.25	m
A1 =	0.020605	m^2
A2 =	0.005842	m^2
A3 =	0.005842	m^2
A4 =	0.020605	m^2

Calculations of the Resultant Forces		
R1 =	5682721	N
R2 =	1611224	N
R3 =	1611224	N
R4 =	5682721	N

Enter Stresses in the 4 beam Sections (ksi)				
σy1 =	40	=	275800000	Pa
σy2 =	40	=	275800000	Pa
σy3 =	40	=	275800000	Pa
σy4 =	40	=	275800000	Pa

Cross Sectional Properties		
E =	2.00E+11	Pa
Ixx =	0.006812038	m^4
Iyy =	0.00056631	m^4
ry =	0.103473216	m
Sx =	0.016380013	m^3
P =	1318427.068	N
Mp =	5026503.196	Nm
Θp =	0.01406594	

* Height is defined from the centroid of the top flange to the centroid of the bottom flange

Figure D26 Calculation Sheet for Homogeneous 40 ksi Girder, $b_f/2t_f = 4.0$

Enter in the Dimensions of the Beam		
Height =	0.781	m *
Width =	0.406	m
Flange Thickness =	0.03684	m
Web Thickness =	0.010802	m
L btw Supports =	15.25	m
A1 =	0.014957	m^2
A2 =	0.004019	m^2
A3 =	0.004019	m^2
A4 =	0.014957	m^2

Calculations of the Resultant Forces		
R1 =	8086187	N
R2 =	1662777	N
R3 =	1662777	N
R4 =	8086187	N

Enter Stresses in the 4 beam Sections (ksi)				
σy1 =	78.411	=	540627500	Pa **
σy2 =	60	=	413700000	Pa
σy3 =	60	=	413700000	Pa
σy4 =	78.411	=	540627500	Pa **

Cross Sectional Properties		
E =	2.00E+11	Pa
Ixx =	0.004935951	m^4
Iyy =	0.000410988	m^4
ry =	0.104062323	m
Sx =	0.012070701	m^3
P =	1818753.652	N
Mp =	6933998.3	Nm
Θp =	0.0267789	

* Height is defined from the centroid of the top flange to the centroid of the bottom flange

** Yield stress value is taken from results of material tests performed on HPS steel used in experimental tests by Azizinamini et al. (1999)

Figure D27 Calculation Sheet for AASHTO Interaction Case 1, HPS Hybrid Girder with 60 ksi Web

Enter in the Dimensions of the Beam		
Height =	0.781	m *
Width =	0.406	m
Flange Thickness =	0.03684	m
Web Thickness =	0.010802	m
L btw Supports =	15.25	m
A1 =	0.014957	m^2
A2 =	0.004019	m^2
A3 =	0.004019	m^2
A4 =	0.014957	m^2

Calculations of the Resultant Forces		
R1 =	8086187	N
R2 =	1385648	N
R3 =	1385648	N
R4 =	8086187	N

Enter Stresses in the 4 beam Sections (ksi)				
σy1 =	78.411	=	540627500	Pa **
σy2 =	50	=	344750000	Pa
σy3 =	50	=	344750000	Pa
σy4 =	78.411	=	540627500	Pa **

Cross Sectional Properties		
E =	2.00E+11	Pa
Ixx =	0.004935951	m^4
Iyy =	0.000410988	m^4
ry =	0.104062323	m
Sx =	0.012070701	m^3
P =	1791707.264	N
Mp =	6830883.943	Nm
Θp =	0.026380675	

* Height is defined from the centroid of the top flange to the centroid of the bottom flange

** Yield stress value is taken from results of material tests performed on HPS steel used in experimental tests by Azizinamini et al. (1999)

Figure D28 Calculation Sheet for AASHTO Interaction Case 1, HPS Hybrid Girder with 50 ksi Web

Enter in the Dimensions of the Beam		
Height =	0.781	m *
Width =	0.406	m
Flange Thickness =	0.03684	m
Web Thickness =	0.010802	m
L btw Supports =	15.25	m
A1 =	0.014957	m^2
A2 =	0.004019	m^2
A3 =	0.004019	m^2
A4 =	0.014957	m^2

Calculations of the Resultant Forces		
R1 =	8086187	N
R2 =	1108518	N
R3 =	1108518	N
R4 =	8086187	N

Enter Stresses in the 4 beam Sections (ksi)				
σy1 =	78.411	=	540627500	Pa **
σy2 =	40	=	275800000	Pa
σy3 =	40	=	275800000	Pa
σy4 =	78.411	=	540627500	Pa **

Cross Sectional Properties		
E =	2.00E+11	Pa
Ixx =	0.004935951	m^4
Iyy =	0.000410988	m^4
ry =	0.104062323	m
Sx =	0.012070701	m^3
P =	1764660.875	N
Mp =	6727769.586	Nm
Θp =	0.02598245	

* Height is defined from the centroid of the top flange to the centroid of the bottom flange

** Yield stress value is taken from results of material tests performed on HPS steel used in experimental tests by Azizinamini et al. (1999)

Figure D29 Calculation Sheet for AASHTO Interaction Case 1, HPS Hybrid Girder with 40 ksi Web

Enter in the Dimensions of the Beam		
Height =	0.781	m *
Width =	0.406	m
Flange Thickness =	0.02766	m
Web Thickness =	0.01441	m
L btw Supports =	15.25	m
A1 =	0.01123	m^2
A2 =	0.005428	m^2
A3 =	0.005428	m^2
A4 =	0.01123	m^2

Calculations of the Resultant Forces		
R1 =	6071225	N
R2 =	2245487	N
R3 =	2245487	N
R4 =	6071225	N

Enter Stresses in the 4 beam Sections (ksi)				
σy1 =	78.411	=	540627500	Pa **
σy2 =	60	=	413700000	Pa
σy3 =	60	=	413700000	Pa
σy4 =	78.411	=	540627500	Pa **

Cross Sectional Properties		
E =	2.00E+11	Pa
Ixx =	0.003939751	m^4
Iyy =	0.000308705	m^4
ry =	0.096260519	m
Sx =	0.009743899	m^3
P =	1465556.576	N
Mp =	5587434.447	Nm
Θp =	0.027034824	

* Height is defined from the centroid of the top flange to the centroid of the bottom flange

** Yield stress value is taken from results of material tests performed on HPS steel used in experimental tests by Azizinamini et al. (1999)

Figure D30 Calculation Sheet for AASHTO Interaction Case 2, HPS Hybrid Girder with 60 ksi Web

Enter in the Dimensions of the Beam		
Height =	0.781	m *
Width =	0.406	m
Flange Thickness =	0.02766	m
Web Thickness =	0.01441	m
L btw Supports =	15.25	m
A1 =	0.01123	m^2
A2 =	0.005428	m^2
A3 =	0.005428	m^2
A4 =	0.01123	m^2

Calculations of the Resultant Forces		
R1 =	6071225	N
R2 =	1871239	N
R3 =	1871239	N
R4 =	6071225	N

Enter Stresses in the 4 beam Sections (ksi)				
σy1 =	78.411	=	540627500	Pa **
σy2 =	50	=	344750000	Pa
σy3 =	50	=	344750000	Pa
σy4 =	78.411	=	540627500	Pa **

Cross Sectional Properties		
E =	2.00E+11	Pa
Ixx =	0.003939751	m^4
Iyy =	0.000308705	m^4
ry =	0.096260519	m
Sx =	0.009743899	m^3
P =	1428581.382	N
Mp =	5446466.52	Nm
Θp =	0.026352751	

* Height is defined from the centroid of the top flange to the centroid of the bottom flange

** Yield stress value is taken from results of material tests performed on HPS steel used in experimental tests by Azizinamini et al. (1999)

Figure D31 Calculation Sheet for AASHTO Interaction Case 2, HPS Hybrid Girder with 50 ksi Web

Enter in the Dimensions of the Beam		
Height =	0.781	m *
Width =	0.406	m
Flange Thickness =	0.02766	m
Web Thickness =	0.01441	m
L btw Supports =	15.25	m
A1 =	0.01123	m^2
A2 =	0.005428	m^2
A3 =	0.005428	m^2
A4 =	0.01123	m^2

Calculations of the Resultant Forces		
R1 =	6071225	N
R2 =	1496991	N
R3 =	1496991	N
R4 =	6071225	N

Enter Stresses in the 4 beam Sections (ksi)				
σy1 =	78.411	=	540627500	Pa **
σy2 =	40	=	275800000	Pa
σy3 =	40	=	275800000	Pa
σy4 =	78.411	=	540627500	Pa **

Cross Sectional Properties		
E =	2.00E+11	Pa
Ixx =	0.003939751	m^4
Iyy =	0.000308705	m^4
ry =	0.096260519	m
Sx =	0.009743899	m^3
P =	1391606.188	N
Mp =	5305498.592	Nm
Θp =	0.025670677	

* Height is defined from the centroid of the top flange to the centroid of the bottom flange

** Yield stress value is taken from results of material tests performed on HPS steel used in experimental tests by Azizinamini et al. (1999)

Figure D32 Calculation Sheet for AASHTO Interaction Case 2, HPS Hybrid Girder with 40 ksi Web

Table D1 Summary of M_p and q_p for Figures D2 – D32

Parametric Study

HPS Flange w/ 60 ksi Web

bf/2tf	M_p (Nm)	θ_p
5.5	7243525	0.026953
5.0	7867020	0.026910
4.5	8610542	0.026865
4.0	9582287	0.026815
3.5	10807686	0.026760
3.0	12447457	0.026698

HPS Flange w/ 50 ksi Web

bf/2tf	M_p (Nm)	θ_p
5.5	7090823	0.026385
5.0	7715829	0.026393
4.5	8461142	0.026399
4.0	9435212	0.026403
3.5	10663517	0.026403
3.0	12307131	0.026397

HPS Flange w/ 40 ksi Web

bf/2tf	M_p (Nm)	θ_p
5.5	6938121	0.025817
5.0	7564637	0.025875
4.5	8311743	0.025933
4.0	9288138	0.025992
3.5	10519348	0.026046
3.0	12166805	0.026096

Homogeneous 50 ksi

bf/2tf	M_p (Nm)	θ_p
5.5	4798342	0.017855
5.0	5194162	0.017767
4.5	5666192	0.017679
4.0	6283129	0.017582
3.5	7061136	0.017484
3.0	8102283	0.017378

AASHTO Interaction Equation Study

HPS Flange w/ 60 ksi Web

	M_p (Nm)	θ_p
Case 1	6933998	0.026779
Case 2	5587434	0.027035

HPS Flange w/ 50 ksi Web

	M_p (Nm)	θ_p
Case 1	6830884	0.026381
Case 2	5446467	0.026353

HPS Flange w/ 40 ksi Web

	M_p (Nm)	θ_p
Case 1	6727770	0.025982
Case 2	5305499	0.025671

D.2 Rotation Capacity Calculation Sheets

Each model's rotation capacity, *R*, is determined from its respective moment versus rotation plot given in Appendix C. Figure 2, shown here as Figure D33, illustrates the calculation of *R* from the moment versus rotation plot explained in Section 1.0. It is seen from Figure D33 that $?_1$ and $?_2$ must first be calculated in order to calculate *R*.

q_1 is calculated using a linear elastic approximation. The coordinates of two points on the elastic loading portion of the moment versus rotation plot are used to calculate q_1, the theoretical rotation at which the full plastic capacity is achieved based on elastic beam stiffness. The two points on the uploading portion of an actual moment versus rotation plot, obtained from a random ABAQUS run used in the parametric study, are illustrated in Figure D34.

q_2 is calculated using a linear interpolation of two points on the unloading branch of the moment versus rotation plot. The coordinates of two points on opposite sides of the $M/M_p = 1$ line are used to interpolate the value of q_2, the rotation when the moment capacity drops below M_p on the unloading portion of the moment versus rotation plot. The two points used on the unloading portion of an actual moment versus rotation plot, obtained from a random ABAQUS run used in the parametric study, are illustrated in Figure D35.

Excel Calculation Sheets for all model R values are given in Figures D36 – D39. Note that “70F60W” stands for a girder comprised of a HPS flange (F) with 60 ksi web (W).

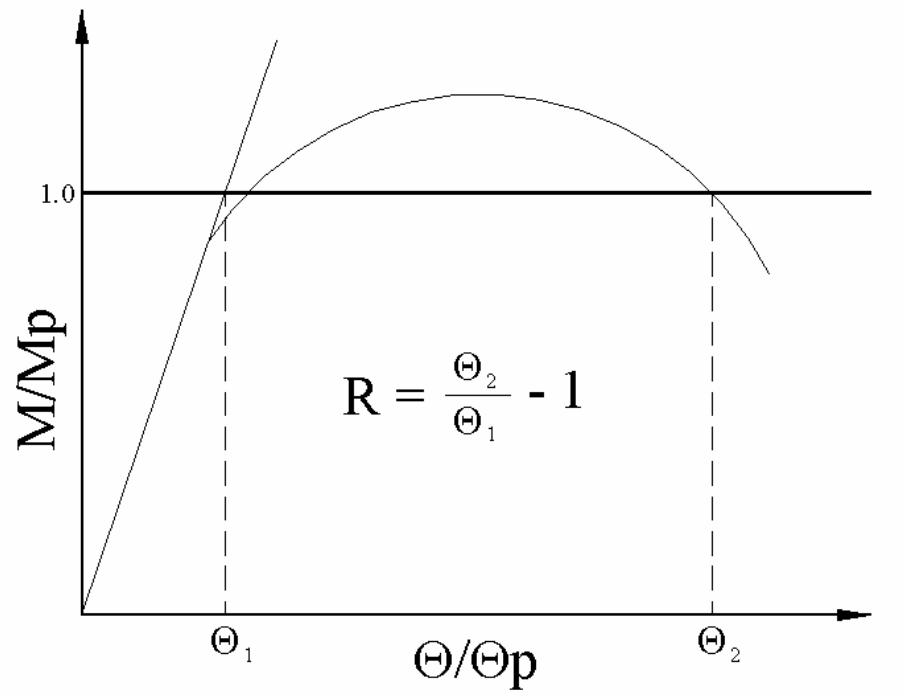

Figure D33 Rotation Capacity Definition

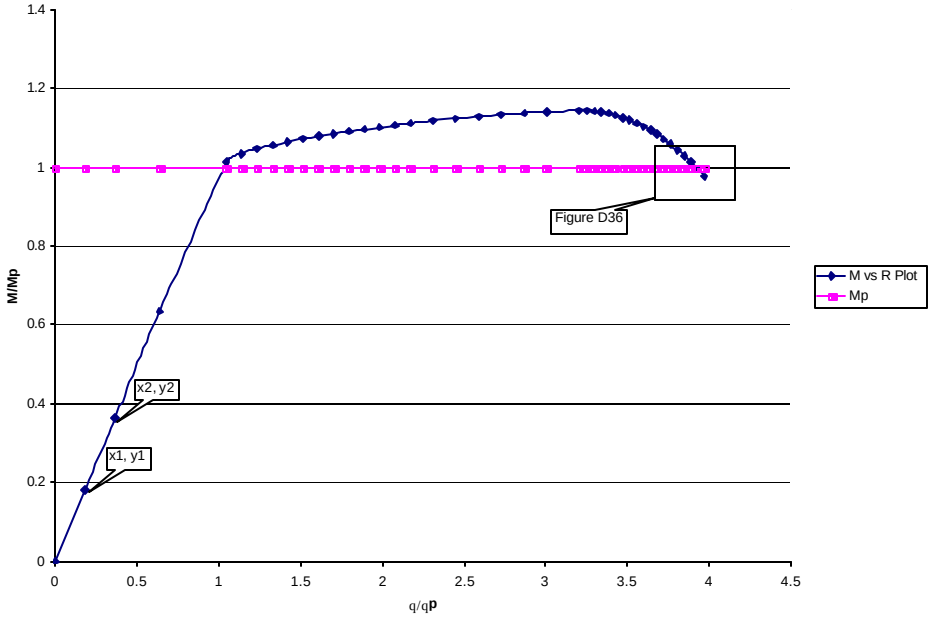

Figure D34 Illustration of Two Points Used to Calculate q_1

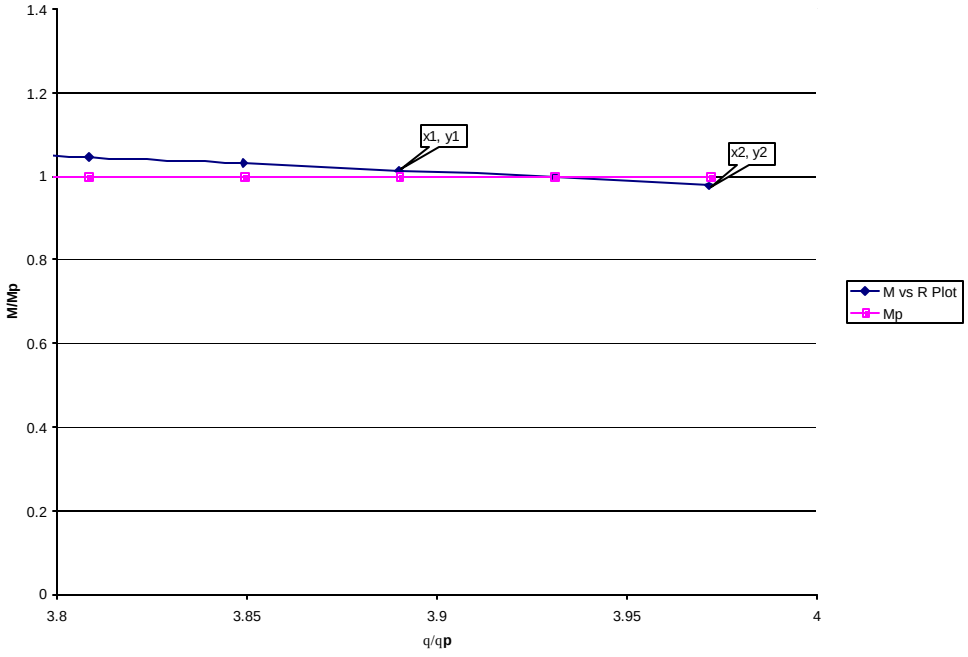

Figure D35 Illustration of Two Points Used to Calculate q_2

AASHTO BRACING

		θ1				θ2						
	b/2tf	X1	Y1	X2	Y2	X1	Y1	X2	Y2	θ1	θ2	R
70F60W	5	0.365	0.363	0.639	0.635	1.61	1.0026	1.7	0.994	1.006684	1.637209	0.626339
	4.5	0.334	0.3318	0.585	0.5802	1.56	1.0062	1.65	0.9983	1.009194	1.630633	0.615777
	4	0.301	0.2982	0.527	0.5215	1.57	1.0027	1.65	0.99533	1.011286	1.599308	0.58146
	3.5	0.268	0.264	0.469	0.462	1.147	1.0074	1.64	0.989	1.015152	1.345272	0.325193
	3	0.234	0.2296	0.409	0.40156	1.42	1.0025	1.51	0.9917	1.01802	1.440833	0.41533

		θ1				θ2						
	b/2tf	X1	Y1	X2	Y2	X1	Y1	X2	Y2	θ1	θ2	R
70F50W	5	0.372	0.37023	0.651	0.647	1.636	1.00109	1.729	0.9924	1.006844	1.647665	0.636465
	4.5	0.34023	0.3376	0.5956	0.5905	1.5897	1.0036	1.6752	0.9956	1.009099	1.628175	0.613493
	4	0.306	0.303	0.535	0.5296	1.52936	1.0059	1.6587	0.99313	1.010382	1.589118	0.572789
	3.5	0.4753	0.4687	0.78105	0.7684	1.484	1.002137	1.57	0.9928	1.017325	1.503683	0.478075
	3	0.2363	0.2322	0.4136	0.40614	1.344	1.0068	1.43224	0.9952	1.018932	1.395727	0.369794

		θ1				θ2						
	b/2tf	X1	Y1	X2	Y2	X1	Y1	X2	Y2	θ1	θ2	R
70F40W	5	0.189	0.1889	0.3798	0.3776	1.5702	1.0054	1.6656	0.9967	1.009127	1.629414	0.614677
	4.5	0.346	0.344	0.6063	0.6008	1.52853	1.0064	1.7021	0.9896	1.010941	1.594652	0.577394
	4	0.3107	0.3076	0.5439	0.5381	1.4603	1.00768	1.6158	0.9919	1.011211	1.535981	0.518952
	3.5	0.482	0.475	0.79126	0.7746	1.44349	1.003	1.52056	0.99382	1.023928	1.468676	0.434356
	3	0.239	0.235	0.418	0.411	1.265	1.007	1.354	0.9948	1.01704	1.316066	0.294016

		θ1				θ2						
	b/2tf	X1	Y1	X2	Y2	X1	Y1	X2	Y2	θ1	θ2	R
50F50W	5	0.277	0.275	0.553	0.54998	3.48	1.0132	3.7	0.9959	1.004689	3.647861	2.630835
	4.5	0.254	0.252	0.5089	0.504	3.6119	1.00922	3.8859	0.98692	1.010608	3.725186	2.686084
	4	0.45934	0.4547	0.8041	0.79514	3.644	1.0078	3.81801	0.9936	1.01156	3.739583	2.696849
	3.5	0.41	0.4047	0.7171	0.708	3.6425	1.00262	3.77336	0.99169	1.012758	3.673868	2.627586
	3	0.179	0.176	0.359	0.3527	3.1832	1.014426	3.489251	0.993818	1.018389	3.397442	2.336095

Figure D36 Rotation Capacity Calculation Sheet Used for AASHTO Bracing Models

D/2 BRACING

		θ1				θ2						
	b/2tf	X1	Y1	X2	Y2	X1	Y1	X2	Y2	θ1	θ2	R
70F60W	5	0.36445	0.363236	0.638026	0.63534	3.8899	1.01546	3.930769	0.9967	1.004659	3.92358	2.905386
	4.5	0.33367	0.33188	0.584123	0.580515	4.04896	1.004621	4.0899	0.99053	1.006674	4.062386	3.035454
	4	0.52627	0.521699	0.864855	0.856059	4.0864	1.001442	4.119956	0.9871	1.010615	4.089775	3.046819
	3.5	0.468127	0.462634	0.769327	0.759482	4.06108	1.01298	4.124597	0.98806	1.013371	4.094164	3.040142
	3	0.408445	0.401651	0.671218	0.659521	3.528576	1.00407	3.55722	0.995148	1.018171	3.541643	2.478438

		θ1				θ2						
	b/2tf	X1	Y1	X2	Y2	X1	Y1	X2	Y2	θ1	θ2	R
70F50W	5	0.37159	0.37035	0.650528	0.64779	3.920666	1.010598	3.95097	0.995538	1.004639	3.941991	2.92379
	4.5	0.339563	0.337741	0.594436	0.590766	4.1659	1.007488	4.207562	0.99462	1.00666	4.190143	3.162422
	4	0.53448	0.52983	0.8781	0.86681	4.16146	1.00343	4.18796	0.99217	1.013914	4.169532	3.112312
	3.5	0.47456	0.46889	0.77969	0.76909	4.06676	1.00231	4.097056	0.99262	1.014392	4.073982	3.016181
	3	0.412103	0.40623	0.678871	0.66702	3.137413	1.0536	3.23545	0.98329	1.019485	3.21215	2.150757

		θ1				θ2						
	b/2tf	X1	Y1	X2	Y2	X1	Y1	X2	Y2	θ1	θ2	R
70F40W	5	0.189465	0.188927	0.379019	0.377755	4.08789	1.002714	4.118805	0.989455	1.003656	4.094218	3.079304
	4.5	0.345666	0.3438	0.605083	0.601188	4.20608	1.0045	4.2215	0.999226	1.007039	4.219237	3.189747
	4	0.31	0.308	0.542	0.538	4.116	1.008	4.139	0.9985	1.008017	4.135368	3.102477
	3.5	0.480958	0.475315	0.789877	0.775276	4.01502	1.00862	4.0572	0.991776	1.021312	4.036606	2.952373
	3	0.417867	0.410916	0.68647	0.67268	2.2807	1.00282	2.305529	0.98779	1.022342	2.285359	1.235415

		θ1				θ2						
	b/2tf	X1	Y1	X2	Y2	X1	Y1	X2	Y2	θ1	θ2	R
50F50W	5	0.276	0.275	0.552	0.5501	6.93	1.0108	7.02	0.98343	1.003372	6.965513	5.942105
	4.5	0.507	0.504	0.887596	0.881737	7.29531	1.016896	7.385797	0.9953	1.006754	7.366104	6.316686
	4	0.45849	0.45485	0.802609	0.795574	7.62522	1.00236	7.68208	0.99522	1.009072	7.644014	6.575292
	3.5	0.20462	0.20243	0.40933	0.404755	7.451	1.0062	7.50247	0.9991	1.011592	7.495946	6.41005
	3	0.35849	0.35275	0.62749	0.6171	6.8289	1.00352	6.89797	0.9951	1.017125	6.857775	5.742311

Figure D37 Rotation Capacity Calculation Sheet Used for *d/2* Bracing Models

D BRACING

		θ1				θ2						
	b/2tf	X1	Y1	X2	Y2	X1	Y1	X2	Y2	θ1	θ2	R
70F60W	5.5	0.197	0.197	0.395	0.394	3.321	1.006	3.372	0.995	1.004076	3.348818	2.335223
	5	0.182	0.1817	0.364	0.363	4.54	1.003	4.5475	0.99957	1.003459	4.54656	3.530885
	4.5	0.33358	0.332	0.584	0.581	5.2287	1.005	5.243	0.9988	1.005389	5.240232	4.212142
	4	0.3006	0.298	0.526	0.522	5.6412	1.011	5.671	0.995	1.006988	5.661688	4.622401
	3.5	0.267	0.265	0.467	0.463	10.978	1.109	10.10.877	0.995	1.009424	10.9	9.798235
	3									N/A	N/A	N/A

		θ1				θ2						
	b/2tf	X1	Y1	X2	Y2	X1	Y1	X2	Y2	θ1	θ2	R
70F50W	5.5	0.4035	0.403	0.706	0.705	3.865	1.003	3.884	0.997	1.001488	3.8745	2.868742
	5	0.186	0.185	0.372	0.37	4.731	1.003	4.739	0.998	1.005405	4.7358	3.710339
	4.5	0.339	0.338	0.594	0.591	5.385	1.012	5.412	0.996	1.006233	5.40525	4.371767
	4	0.3052	0.3029	0.534	0.53	5.612	1.038	5.642	0.999	1.007518	5.641231	4.599135
	3.5	0.271	0.268	0.474	0.469	8.1108	1.00746	8.1108	0.998	1.010284	8.1108	7.028241
	3	0.236	0.232	0.413	0.406	2.899	1.013	2.914	0.997	1.017241	2.911188	1.861845

		θ1				θ2						
	b/2tf	X1	Y1	X2	Y2	X1	Y1	X2	Y2	θ1	θ2	R
70F40W	5.5	0.2062	0.206	0.4124	0.412	4.233	1.007	4.25	0.999	1.000971	4.247875	3.243755
	5	0.379	0.378	0.663	0.6598	4.919	1.0137	4.922	0.999	1.005856	4.921796	3.893142
	4.5	0.346	0.344	0.605	0.601	5.505	1.005	5.544	0.984	1.007105	5.514286	4.475383
	4	0.3101	0.308	0.543	0.538	4.7464	1.0054	4.766	0.981	1.010825	4.750738	3.699861
	3.5	0.274	0.2717	0.48	0.475	5.657	1.016	5.69	0.998	1.011972	5.686333	4.619059
	3	0.119	0.117	0.239	0.235	1.808	1.001	1.82	0.996	1.016966	1.8104	0.780197

		θ1				θ2						
	b/2tf	X1	Y1	X2	Y2	X1	Y1	X2	Y2	θ1	θ2	R
50F50W	5.5	0.298	0.298	0.596	0.596	8.103	1.02	8.1865	0.999	1	8.182524	7.182524
	5	0.276	0.2752	0.552	0.55	8.902	1.009	8.958	0.991	1.003965	8.93	7.894732
	4.5	0.253	0.252	0.507	0.504	9.258	1.003	9.3312	0.978	1.006937	9.266784	8.202948
	4	0.229	0.227	0.458	0.455	9.3367	1.028	9.484	0.978	1.00539	9.419188	8.368687
	3.5	0.408	0.405	0.7156	0.7082	23.445	1.016	23.714	0.976	1.011635	23.5526	22.28173
	3	0.179	0.176	0.358	0.353	12.202	1.009	12.294	0.995	1.012311	12.26114	11.11203

Figure D38 Rotation Capacity Calculation Sheet Used for *d* Bracing Models

AASHTO Interaction Case 1; bf/2tf = 5.51 , h/tw = 72.3											
	θ_1				θ_2						
	X1	Y1	X2	Y2	X1	Y1	X2	Y2	θ_1	θ_2	R
70F60W	0.418	0.412	0.732	0.72	1.526	1.001	1.548	0.999	1.017455	1.537	0.510633
70F50W	0.4246	0.418	0.743	0.7306	1.547	1.002	1.57	0.999	1.017398	1.562333	0.535616
70F40W	0.4311	0.425	0.745	0.738	1.512	1.002	1.546	0.999	1.007753	1.534667	0.522859

Homogeneous Girder; bf/2tf = 4.0 , h/tw = 45											
	θ_1				θ_2						
	X1	Y1	X2	Y2	X1	Y1	X2	Y2	θ_1	θ_2	R
40F40W	0.287	0.284	0.5742	0.5684	5.273	1.006	5.596	0.98	1.010049	5.347538	4.294334

Figure D39 Rotation Capacity Calculation Sheet Used for Additional Models

BIBLIOGRAPHY

BIBLIOGRAPHY

American Association of State Highway and Transportation Officials (AASHTO), (1998), *LRFD Bridge Design Specifications*, Cusotmary U.S. Units, Second Addition, Washington, D.C.

American Association of State Highway and Transportation Officials (AASHTO), (1998), *LRFD Bridge Design Specifications*, S.I. Units, Second Addition, Washington, D.C.

ABAQUS, (2001), ABAQUS Standard User's Manual, Version 5.8, Volumes 1 to 3, Hibbit, Karlsson & Sorensen, Inc., Pawtucket, Rhode Island, USA.

American Institute of Steel Construction (AISC), (1999), *Load and Resistance Factor Design (LRFD) Specification for Structural Steel Buildings*, Chicago, Illinois.

American Society of Civil Engineers (ASCE), (1971), Plastic Design in Steel, A Guide and Commentary, American Society of Civil Engineers, New York, p. 80.

Joint ASCE-AASHO Committee on Flexural Members, (1968), "Design of Hybrid Steel Beams, Report of the Subcommittee 1 on Hybrid Beams and Girders," *Journal of the Structural Division*, ASCE, Vol. 94, No. ST6, June, pp. 1397-1426.

Azizinamini, A., Mans, P., and Yakel, A.J., (1999), *Flexural Capacity of HPS-70W Bridge Girders*, National Bridge Research Organization (NaBRO), Lincoln, Nebraska

Boresi A. P., Schmidt R. J., and Sidebottom O. M., (1993), *Advanced Mechanics of Materials*, Fifth Ed. John Wiley & Sons, Inc.

Climenhaga, J.J., Johnson, R.P., (1972), "Moment-Rotation Curves for Locally Buckled Beams," *Journal of the Structural Division*, ASCE, Vol. 98, No. ST6, pp. 1239-1254.

Earls C.J., (1995), "On the Use of Nonlinear Finite Element Analysis Techniques to Model Structural Steel Angle Response," Ph. D. Dissertation, University of Minnesota, Minneapolis, USA.

Earls, C.J., (1999), "On the Inelastic Failure of High Strength Steel I-Shaped Beams," *Journal of Constructional Steel Research*, Vol. 49, No. 1, January, pp. 1-24.

Earls C. J., (2000a), "On Geometric Factors Influencing the Structural Ductility of Compact I-Shaped Beams," *Journal of Structural Engineering*, ASCE, Vol. 126, No. 7, pp. 780-789.

Earls C. J., (2000b), "The Influence of Material Effects on the Structural Ductility of Compact I-Shaped Beams," *Journal of Structural Engineering*, ASCE, Vol. 126, No. 11, pp. 1268-1278.

Earls, C.J. and Shah, B.J., (2001), "High Performance Steel Bridge Girder Compactness," *Journal of Constructional Steel Research, In Press, Uncorrected Proof*, pp. 1-22.

Frost, R.W. and Schilling, C.G., (1964), "Behavior of Hybrid Beams Subjected to Static Loads," *Journal of the Structural Division*, ASCE, Vol. 90, No. ST3, June, pp. 55-88.

Gioncu, V., Tirca, L., Petcu, D., (1996), "Interaction Between In-Plane and Out-of-Plane Plastic Buckling of Wide-Flange Section Members," Proceeding of the Coupled Instabilities in Metal Structures Symposium, Liege, Belgium, Imperial College Press, London, pp. 273-282.

Green, P.S., Sauce, R., and Ricles, J.M., (2002), "Strength and Ductility of HPS Flexural Members," *Journal of Constructional Steel Research, In Press, Uncorrected Proof*, pp. 2-35.

Haaijer, G., (1961), "Economy of High Strength Steel Structural Members," *Journal of the Structural Division*, ASCE, Vol. 87, No. ST 8, December, pp. 1-23.

Logan, D.L., (1993), *A First Course In the Finite Element Method*, PWS Publishing Company, Boston, MA.

Riks E., (1972) "The Application of Newton's Method to the Problem of Elastic Stability," *Journal of Applied Mechanics*, ASME, Vol. 39, pp. 1060-1066.

Salmon, C. G., Johnson, J. E., (1996), *Steel Structures, Design and Behavior*, Fourth Edition, HarperCollins Publishers Inc., New York, New York.

Simo, J.C., Hughes, (1988), *Computational Inelasticity, Interdisciplinary Applied Mathematics*, Vol. 7, Stanford University, Stanford, CA.

Teal, R. (2002), "Fabrication With High Performance Steel," Retrieved January 11, 2002, from http://www.fhwa.dot.gov/bridge/hps.htm

Thomas, S. J. and Earls, C.J., (2002), "Bracing and Diaphragm Requirements for HPS70W Girders," *Report No. CE/ST 22*, Department of Civil and Environmental Engineering, University of Pittsburgh, Pittsburgh, Pennsylvania.

Toprac, A. A., (1964), "The Ultimate Strength of Hybrid Steel Beams," University of Texas Report, Austin, Texas.

Wasserman, E. and Pate, H., (2002), “Tennessee’s Experience with High Performance Steel: An Owner’s Perspective,” Retrieved January 11, 2002, from http://www.fhwa.dot.gov/bridge/hps.htm

Wright, W., (1997), “High Performance Steel: Research to Practice,” Retrieved January 11, 2002, from http://www.steel.org/infrastructure/bridges/high_performance/index.html

Yura, J.A., Helwig, T.A. (2001) "Bracing for Stability," *Notes from a Short Course Sponsored by the Structural Stability Research Council and the American Institute of Steel Construction.*

Yura, J.A., Galambos, T.V., and Ravindra, M.K., (1978), “The Bending Resistance of Steel Beams,” *Journal of the Structural Division*, ASCE, Vol. 104, No. ST9, September, pp. 1355-1369.

REFERENCES NOT CITED

Barker, R. M. and Puckett, J. A., (1997), *Design of Highway Bridges, Based on AASHTO LRFD, Bridge Design Specifications*, John Wiley and Sons, Inc., New York, New York.

Barth Karl E., White Donald W. and Bobb Betsy M., (2000), "Negative bending resistance of HPS70W girders," *Journal of Constructional Steel Research*, Vol. 53, January, pp. 1-31.

Basler, K., and Thurlimann, M., (1961), "Strength of Plate Girders in Bending," *Journal of the Structural Division*, ASCE, Vol. 87, No. ST6, August, pp. 153-181.

Basler, K., (1961), "Strength of Plate Girders in Shear," *Journal of the Structural Division*, ASCE, Vol. 87, No. ST7, October, pp. 153-181.

Basler, K., (1961), "Strength of Plate Girders in Shear," *Journal of the Structural Division*, ASCE, Vol. 87, No. ST7, October, pp. 153-181.

Basler, K., (1961), "Strength of Plate Girders in Combined Bending and Shear," *Journal of the Structural Division*, ASCE, Vol. 87, No. ST7, October, pp. 181-197.

Beer, F. P. and Johnston, Jr., E.R., (1992), *Mechanics of Material*, Mc-Graw Hill, Inc. New York, New York.

Earls, C.J., (2001), "Constant Moment Behavior of High Performance Steel I-Shaped Beams," *Journal of Constructional Steel Research*, Volume 57, No. 7, July, pp. 711-728.

Galambos, T.V., (1977), "History of Steel Beam Design," Engineering Journal, AISC, Vol. 14, Fourth Quarter, pp. 141-147.

Miki, C., Homma, K., and Tominaga, T., (2002), "High Strength and High Performance Steels and Their Use In Bridge Structures," *Journal of Constructional Steel Research*, Volume 58, No, 1, January, pp. 3-20.

Ricles J. M., Sauce R., Green P. S., (1998), "High Strength Steel: Material and Geometric Characteristics on Inelastic Flexural Behavior," *Engineering Structures*, Vol. 20, April, pp. 323-335.

White D. W., Barth K. E., (1998), "Strength and Ductility of Compact-Flange I-Girders in Negative Bending," *Journal of Constructional Steel Research*, Vol. 45, No. 3, pp. 241-280.